

The H1 Trigger for Neutral Current  
Deep Inelastic Scattering Events  
at Low  $Q^2$

Dissertation

zur Erlangung des Doktorgrades  
des Fachbereichs Physik  
der Universität Hamburg

vorgelegt von  
**Tibor Kurča**  
aus Košice

Hamburg  
1993

**Gutachter der Dissertation:**

Prof. Dr. H.-H. Duhm  
Prof. Dr. W. Bartel

**Gutachter der Disputation:**

Prof. Dr. H.-H. Duhm  
Prof. Dr. E. Lohrmann

**Datum der Disputation:**

17.12.1993

**Sprecher des Fachbereichs Physik  
und Vorsitzender  
des Promotionsausschusses:**

Prof. Dr. E. Lohrmann

## Abstract

The experiments at the  $e^-p$  storage ring HERA have opened entirely new kinematical domains for the measurement of the proton structure functions. Interesting physics results are expected at high momentum transfers  $Q^2 \rightarrow 10^5 \text{ GeV}^2$ , but also in very low  $x, Q^2$  region. The topic of this thesis is the study of the design of a dedicated electron trigger (BSET) for the backward electromagnetic calorimeter (BEMC) at H1. A further task is the elaboration of efficient trigger algorithms for neutral current deep inelastic scattering (NC DIS) at low  $Q^2$  ( $Q^2 < 100 \text{ GeV}^2$ ), using the available triggers of the H1 detector. Physics rates for NC DIS at  $Q^2 < 100 \text{ GeV}^2$  are relatively high ( $\sim 1 \text{ Hz}$ ), but on the other hand the total background rate at a full design luminosity is expected to be much larger ( $\sim 100 \text{ kHz}$ ). The main goal is to reduce the L1 trigger rate down to  $\leq 100 \text{ Hz}$  and simultaneously to keep a high trigger efficiency for NC DIS events in the whole kinematical region of interest. The designed trigger has been realized and has worked successfully from the very beginning of the data taking at HERA. Different methods to check the technical performance of the trigger on-line as well as off-line and to calculate the trigger efficiency for NC events are developed. Analysis of the data triggered by the BSET in 1992 is made, and on the top of the standard selection criteria additional ones, using detailed trigger and data acquisition information, are applied.

## Zusammenfassung

Die Experimente am  $e^-p$  HERA Speicherring haben vollständig neue kinematische Gebiete für die Messung der Strukturfunktionen des Protons eröffnet. Interessante physikalische Ergebnisse werden sowohl bei hohen Impulsüberträgen  $Q^2 \rightarrow 10^5 \text{ GeV}^2$  als auch bei sehr kleinen Werten der kinematischen Variablen  $x, Q^2$  erwartet. In der vorliegenden Arbeit werden Studien zum Design eines Elektron-Triggers (BSET) für das elektromagnetische Rückwärtskalorimeter (BEMC) des H1-Detektors dargestellt. Weitere Untersuchungen betreffen die Erstellung von effizienten Trigger-Algorithmen für die tiefinelastische Streuung bei neutralen Strömen (NC DIS) und kleinen  $Q^2$  ( $Q^2 < 100 \text{ GeV}^2$ ) unter Berücksichtigung aller verfügbarer Subtrigger des H1-Detektors. Die Raten für NC DIS Ereignisse mit  $Q^2 < 100 \text{ GeV}^2$  liegen relativ hoch ( $\sim 1 \text{ Hz}$ ), aber es wird erwartet, daß die totale Rate von Untergrundereignissen bei der Design-Luminosität Werte bis  $\sim 100 \text{ kHz}$  erreichen kann. Die wesentliche Aufgabe ist die L1-Triggerrate auf einen Wert  $\leq 100 \text{ Hz}$  zu bringen und gleichzeitig eine hohe Trigger-Effizienz für den kinematisch interessanten Bereich zu garantieren. Der entworfene Trigger wurde realisiert und erfolgreich seit Beginn der Datennahme bei H1 eingesetzt. Verschiedene Methoden zur Funktionskontrolle des Triggers während und nach der Datennahme (On- und Offline), sowie zur Berechnung der Trigger-Effizienz physikalischer NC Ereignisse wurden entwickelt. Die Datenanalyse der durch den BSET getriggerten NC DIS Ereignisse wurde zuerst mit den Standard-Selektionskriterien durchgeführt und später um zusätzliche Selektionskriterien unter Berücksichtigung detaillierter Trigger- und Dateninformationen erweitert.



*” Dedicated to the memory of  
my father Karol Kurča”*



# Contents

<b>Introduction</b>	<b>2</b>
<b>1 Physics at HERA</b>	<b>5</b>
1.1 Deep Inelastic Scattering . . . . .	5
1.2 Kinematics . . . . .	6
1.3 Topological characteristics of NC DIS events . . . . .	7
1.4 Reconstruction of the kinematical variables . . . . .	9
1.4.1 Introduction . . . . .	9
1.4.2 Electron measurement only . . . . .	10
1.4.3 Hadronic flow measurement only . . . . .	11
1.4.4 Combined methods from electron and hadrons measurements . . . . .	13
1.5 Nucleon Structure Functions . . . . .	13
1.5.1 Introduction . . . . .	13
1.5.2 Structure Functions and Parton Distributions . . . . .	15
1.5.3 Structure Functions at Low $x$ . . . . .	16
1.6 Beyond DIS . . . . .	19
<b>2 H1 Detector</b>	<b>21</b>
2.1 Introduction . . . . .	21
2.2 Calorimetry . . . . .	21
2.2.1 Liquid Argon Calorimeter . . . . .	23
2.2.2 BEMC . . . . .	24
2.2.3 Plug Calorimeter . . . . .	24
2.2.4 Tail catcher calorimeter (TC) . . . . .	26
2.2.5 Luminosity Monitor and Electron Tagger . . . . .	26
2.3 Tracking Detectors . . . . .	26
2.4 Muon Detectors . . . . .	28
2.4.1 Instrumented iron . . . . .	28
2.4.2 Forward Muon Spectrometer . . . . .	28
2.5 Scintillators . . . . .	28
2.5.1 TOF . . . . .	28
2.5.2 Veto Walls . . . . .	29
<b>3 H1 Trigger</b>	<b>30</b>
3.1 Triggering at HERA . . . . .	30
3.2 Frontend pipelines . . . . .	30
3.3 Multi level trigger . . . . .	31
3.4 L1-Trigger elements from specific detectors . . . . .	32
3.4.1 Calorimetry . . . . .	33

3.4.2	Tracking System . . . . .	34
3.4.3	Luminosity system . . . . .	35
3.4.4	Muon system . . . . .	36
3.4.5	Scintillators . . . . .	37
<b>4</b>	<b>Trigger for NC DIS</b>	<b>39</b>
4.1	General requirements . . . . .	39
4.2	NC DIS Triggers . . . . .	39
4.3	Background to the NC DIS Events . . . . .	40
4.3.1	Physics Background . . . . .	40
4.3.2	Machine Background . . . . .	41
<b>5</b>	<b>Trigger Simulations</b>	<b>45</b>
5.1	BSET Trigger Design Simulations . . . . .	46
5.1.1	Electromagnetic Showers in the BEMC . . . . .	47
5.1.2	Hadronic Showers in the BEMC . . . . .	51
5.1.3	NC DIS and Photoproduction Events in the BEMC . . . . .	52
5.1.4	Machine Background Simulations . . . . .	56
5.1.5	Proposed BEMC Electron Trigger Elements: Summary . . . . .	59
5.2	Trigger Algorithms for NC DIS . . . . .	62
5.2.1	Low $Q^2$ Events . . . . .	62
5.2.2	High $Q^2$ Events . . . . .	68
5.2.3	Subtriggers for NC DIS: Summary . . . . .	69
<b>6</b>	<b>BSET Trigger - Hardware Realisation</b>	<b>72</b>
6.1	Trigger Elements and Algorithm . . . . .	72
6.2	BSET Hardware . . . . .	73
6.2.1	GAIN Card and ATD Module . . . . .	73
6.2.2	CHSM and THRM Modules . . . . .	77
6.2.3	CIM Module . . . . .	77
6.2.4	CSM, CEM and ECTM Modules . . . . .	78
6.2.5	TM Module . . . . .	78
6.2.6	Monitor (GPTP) Modules . . . . .	79
6.2.7	BSET Timing Characteristics . . . . .	79
6.3	BSET Operation Modes . . . . .	79
6.4	Calibration and Timing Adjustment . . . . .	81
6.4.1	Electronic Calibration of the Trigger . . . . .	81
6.4.2	Timing Adjustment Procedure . . . . .	82
<b>7</b>	<b>BSET Trigger Performance</b>	<b>83</b>
7.1	Introduction . . . . .	83
7.1.1	Trigger - Reconstructed Energy Correlations . . . . .	83
7.1.2	Thresholds and Efficiency Functions Evaluation . . . . .	84
7.2	Technical Performance . . . . .	86
7.2.1	On-line Monitoring of the BSET Triggers . . . . .	86
7.2.2	Stack Performance Check . . . . .	87

7.2.3	Logic Consistency Check . . . . .	87
7.2.4	Verification of the Summing Part . . . . .	87
7.3	Physics Trigger Efficiency . . . . .	90
7.3.1	Stack Thresholds . . . . .	90
7.3.2	Total Energy Thresholds . . . . .	90
7.3.3	Cluster Energy Thresholds . . . . .	91
7.3.4	Efficiency for the Low $Q^2$ NC DIS . . . . .	91
7.3.5	Monitor Triggers . . . . .	94
7.3.6	Pileup . . . . .	97
7.3.7	One Diode (1-D) Events . . . . .	97
<b>8</b>	<b>Measurement of NC DIS at Low <math>Q^2</math></b>	<b>100</b>
8.1	Standard Event Selection . . . . .	100
8.1.1	Background Subtraction . . . . .	102
8.2	Discussion . . . . .	103
	<b>Summary</b>	<b>107</b>
<b>A</b>	<b>The H1 Simulation Programs</b>	<b>109</b>
A.1	The H1SIM Package . . . . .	109
A.1.1	BSET Trigger Code in H1SIM . . . . .	110
A.2	The H1FAST . . . . .	111
A.3	The H1PSI (Parametrised Simulation) . . . . .	112
A.3.1	BEMC Geometry in H1PSI . . . . .	112
A.3.2	BSET Trigger Code in H1PSI . . . . .	112
<b>B</b>	<b>The BEMC parameters</b>	<b>114</b>
B.1	Material Constants . . . . .	114
B.2	The BEMC Geometry (Granularity) . . . . .	115
B.2.1	Transversal Size of EM Showers . . . . .	115
B.2.2	Energy Containment (Energy Leakage) . . . . .	115
	<b>Bibliography</b>	<b>117</b>

## Introduction

*" ... even with the best evidence available at any one time, no one can predict how any one class of experiment or any theory may turn out, and which will be the best way ahead..."* D.H. Perkins, Workshop Experimentation at HERA, Amsterdam 1983

First serious considerations on building an electron-proton collider in Europe date back to the beginning of the seventies [1]. In the following years intensive studies on the possibility to build such a machine at CERN and DESY were done under the auspices of ECFA <sup>1</sup>. Two important decisions of the European High Energy Physics community opened the way for DESY as a site for the future electron-proton collider: the decision to build a  $p\bar{p}$  collider and as a long-term program an  $e^-e^+$  collider LEP, both at CERN. When taking into account other facilities, existing or under construction (Tevatron, Isabelle), the need to complement this program of high energy physics research raised the interest in an  $e^-p$  machine. In October 1979 the DESY Scientific Policy Committee decided to present to the German authorities the proposal for HERA (Hadron-Elektron-Ring-Anlage) and in February 1981 the unique scientific value of this project was recognized by the German Federal Government Committee and principal recommendation to construct the  $e^-p$  collider was given.

The pointlike nature of leptons makes them particularly well-suited probes of the more complicated nucleon structure. Not surprisingly, especially processes with a large  $Q^2$  momentum transfer, which due to the uncertainty principle probe very short distances, were in the center of interest [2],[3].

Concentration on the high  $Q^2 > 100 \text{ GeV}^2$  physics has found its reflection also in the H1 detector and trigger design [2],[3],[4]. For the backward region, i.e. for the scattered electron angle  $\theta_e > 145^\circ$  (see Fig. 2.3), only very raw hadronic energy measurement was foreseen and even for the electron measurement the angular coverage down to only  $170^\circ$  was considered sufficient and the task of the trigger was defined this way [2]:

*"The aim of the trigger is to collect all interesting physics events with minimal background. In reality this means all events with  $Q^2 \geq 100 \text{ GeV}^2$  together with a sample of lower  $Q^2$  events..."*

This attitude has its roots of course in the general status of the knowledge at that time. E.g. the limit on the top quark mass was at  $\geq 40 \text{ GeV}$  and this was still within the HERA reach. On the other hand the precision of the QCD calculations was e.g. insufficient to estimate the higher twist contribution. Thus it was hard in the region of low  $Q^2$  to distinguish if the scaling violations in the structure functions measurements vary logarithmically or according to a power law as predicted by other strong interaction theory candidates. Scattering experiments with large momentum transfers  $Q^2 > 100 \text{ GeV}^2$  are

---

<sup>1</sup>European Committee for Future Accelerators

free from potential nonperturbative, mass and higher twist effects. Additionally one can hope that at some sufficiently large  $Q^2$  the quark substructure could be revealed.

Later, with the progress in the theory as well as in the experiment, the importance and interest for low  $Q^2 < 100 \text{ GeV}^2$  physics has grown. The HERA workshop 1987 already realized the importance and potential of the very low  $x$ , low  $Q^2$  region. Theoretical considerations suggested that at very low  $x$  the structure functions may in fact behave drastically differently from any of the available extrapolations [5]. But still the detailed studies were devoted mostly to structure functions measurement at  $Q^2 > 100 \text{ GeV}^2$ .

In the late 1989 the urgent need for an inclusive electron trigger in the backward H1 region was realized. The detailed background studies showed that with the originally proposed trigger on the total energy of the Backward ElectroMagnetic Calorimeter (BEMC), the access to the low  $(x, Q^2)$  physics at high  $y$  would be very limited. Consequently it was decided to build a dedicated single electron trigger based on the design of the BEMC, which was already being constructed.

The task of this thesis is the detailed design simulation of the Single Electron Trigger (BSET) for the BEMC and preparation of the trigger algorithms for the NC DIS at  $Q^2 < 100 \text{ GeV}^2$ . After successful realization of the BSET trigger, its performance during the data taking period in 1992 was checked and the trigger efficiencies for the physics analysis were determined.

The thesis is structured into the following Chapters:

In the **Chapter 1** the basics of the DIS physics, kinematics and experimental measurement of the variables of interest are presented.

In the **Chapters 2 and 3** the main components of the H1 detector and the trigger are described. Emphasis is put on the trigger elements used later for the simulation of the trigger algorithms for NC DIS events. Specifications of triggering at HERA 96  $ns$  bunch crossing intervals are described and the importance of pipelining and multilevel trigger scheme is discussed.

**Chapter 4** is devoted to the general aspects of triggering on NC DIS events. The basic requirements on the triggers and main background sources are given.

In the **Chapter 5** the BSET trigger design simulations results are presented. From the studies of the behaviour of electromagnetic and hadronic showers in the BEMC basic trigger elements are defined. The BSET trigger detects well localized energy deposits, corresponding to the electromagnetic clusters. Subtriggers, i.e. combinations with trigger elements available from other subdetectors, and trigger algorithms for triggering on the low  $(x, Q^2)$  NC DIS processes are proposed. These algorithms are optimized in order to suppress the unwanted background events to the acceptable rate ( $\leq 100 \text{ Hz}$ ).

Hardware realization of the BSET trigger is described in the **Chapter 6**.

In the **Chapter 7** the BSET trigger performance in the real data taking is analysed. Correlations between trigger energies and off-line reconstructed quantities are shown. Tools to check the technical performance by on-line monitoring, using the monitor triggers and logic consistency checks are developed. The trigger thresholds calibration is provided and the physics trigger efficiency for the low  $(x, Q^2)$  NC DIS is calculated. Pileup studies and studies of an unexpected source of background events are done.

In the **Chapter 8** the physics analysis of the measured data in the new kinematical domain with two additional selection criteria is performed.

At the end, in the **Summary**, the main results of all chapters are briefly summarized.

Finally in the **Appendices A** and **B** a short description of the H1 software environment resp. basic BEMC material constants and parameters important for the showers development is given.

## Chapter 1

# Physics at HERA

## 1.1 Deep Inelastic Scattering

Deep inelastic lepton-nucleon scattering (DIS) has played a dominant role in the study of the basic structure of the matter and contributed significantly to the understanding of the electromagnetic, weak and strong interactions at the quark-parton level.

To penetrate deeper into the matter, to probe the nucleon structure with much better resolution <sup>1</sup>, the large electron-proton collider HERA (Hadron-Elektron-Ring- Anlage) has been completed at DESY Hamburg in the year 1991. All previous DIS measurements were performed at fixed target experiments but at HERA for the first time two DIS experiments with assymmetric colliding beams were built. In the late spring 1992 the first physics collisions in both detectors H1 and ZEUS were observed.

Electrons and protons colliding at nominal energies  $E_e = 30 \text{ GeV}$  resp.  $E_p = 820 \text{ GeV}$  will provide a centre of mass energy of 314 GeV. This is equivalent to a 50 TeV electron beam hitting a hydrogen fixed target. This opens up an entirely new kinematical region for DIS physics.

In the first years HERA was operated at a slightly smaller electron beam energy of  $E_e = 26.7 \text{ GeV}$ , providing an energy of 296 GeV in the centre of mass system.

With the design luminosity of  $1.5 \cdot 10^{31} \text{ cm}^{-2} \text{ s}^{-1}$  the proton structure will be explored in a domain which is two orders of magnitude smaller in  $x$ -Björken and two orders of magnitude larger in the square of 4-momentum transfer  $Q^2$ , than what has been reached in fixed target experiments (Fig. 1.3). Measurements at values down to  $x \sim 10^{-4}$  at small  $Q^2$  and at  $Q^2 \geq 10^4$  at higher  $x$  values will be possible.

New, precise measurements of the nucleon structure functions at low and very low  $x$  are an important input for theoretical predictions of cross sections at future colliders such as the LHC and the SSC.

Due to the fact that  $Q^2$  values  $\geq M_Z^2$  are achievable, electroweak parameter measurements at HERA can be done. At these  $Q^2$  values the weak process contributions to the cross sections are of the similar size as those due to the electromagnetic processes. Simultaneous measurement of the neutral and charged current interactions (NC resp. CC) gives the HERA machine the potential of the former lepton and neutrino DIS experiments.

The gap between the kinematical regions accessed by the fixed target and HERA experiments at the design energy (Fig. 1.3) will be covered by HERA operation at lower beam energies. The minimal  $e^-$  beam energy is determined by the injection energy into the HERA machine (12 GeV) and minimal proton beam energy is limited by the requirement of keeping reasonable luminosity (300 GeV).

---

<sup>1</sup> $Q^2 \sim 10^5 \text{ GeV}^2$  corresponds to spatial resolution of about  $10^{-18} \text{ m}$ .

The fact that HERA is foreseen to provide also longitudinally polarised electron or positron beams extends the physics potential of this machine. Experiments with polarised internal gas targets will enable to get more information about the spin distributions in the protons and the neutrons.

## 1.2 Kinematics

Inclusive DIS of leptons on nucleons  $e^-p \rightarrow lX$  (Fig. 1.1) provides the most direct way to measure the nucleon structure functions  $F_1$  and  $F_2$ . These structure functions are directly related to the differential cross section of this scattering process (1.24). Thus inevitable prerequisite to study the nucleon structure is a sufficiently precise measurement of the differential cross-sections for the charged -  $e^-p \rightarrow \nu_e X$ , and/or neutral current -  $e^-p \rightarrow e^- X$  scattering processes. NC cross-section involves  $\gamma$  and  $Z^0$  exchange as well as the interference between the two. In the case of CC interaction in our experiment the exchanged particles are  $W^-$  bosons. The rates of NC and CC interactions are comparable only at  $Q^2 > 5000 \text{ GeV}^2$ , below  $Q < 100 \text{ GeV}^2$  the rate of NC events is by two orders of magnitude higher than those of CC [8]. In our studies we will concentrate only on the NC DIS processes.

The cross-section of the  $e^-p \rightarrow e^- X$  process depends on two independent variables, besides the energy  $s$ . In the experiment the polar angle  $\theta_l$  ( $\theta_j$ ) and the corresponding energy  $E_l$  ( $E_j$ ) of the scattered lepton (current jet) are measured. From these two quantities all other global variables can be calculated. From the scattered quark originates the current jet. Non-interacting proton constituents (spectators) emerge in the final state as a proton or target jet (remnant jet). At HERA we take the convention that the direction along the incoming proton is the forward direction with  $+z$  coordinate and  $\theta = 0^\circ$ . The backward hemisphere is defined by the the incoming electron direction and  $\theta \rightarrow 180^\circ$ .

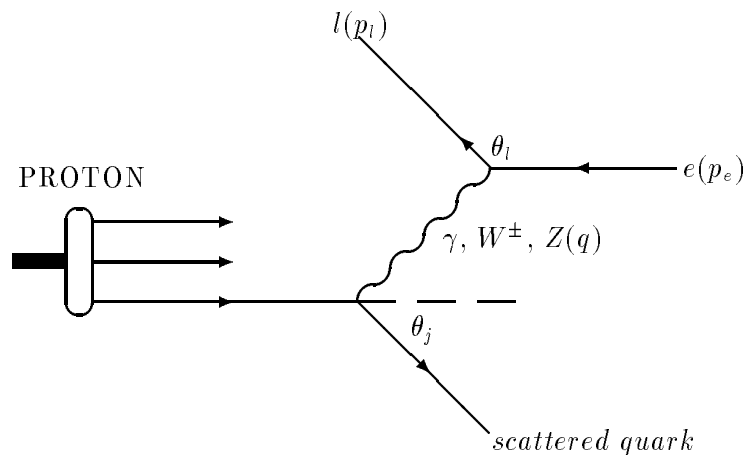


Figure 1.1: Basic diagram for deep inelastic scattering in the quark-parton model.

However, the DIS cross sections and structure functions are usually expressed in terms of  $Q^2$  and  $x$  because of the simple interpretation of these variables in the quark-parton

model.

Denote  $p_e, p_l, P$  the 4-momenta of the incoming and scattered lepton and the incoming proton, respectively, and  $E_l, \theta_l$  the energy and angle of the scattered lepton. When neglecting the masses of the electron, proton and the scattered lepton we obtain the following relations between the kinematic variables characterizing DIS:

$$s = (p_e + P)^2 \approx 4E_e E_p \quad (1.1)$$

$$Q^2 = -q^2 = -(p_e - p_l)^2 \quad (1.2)$$

$$x = \frac{Q^2}{2P \cdot q} \quad (1.3)$$

$$y = \frac{P \cdot q}{P \cdot p_e} = \frac{2P \cdot q}{s} \quad (1.4)$$

$$W^2 = (q + P)^2 \approx \frac{1-x}{x} Q^2 \quad (1.5)$$

Since there are only two degrees of freedom, any two of the above mentioned variables can be used as independent variables for cross section formulae, but  $(x, y)$  and  $(x, Q^2)$  are most commonly used. For more details on the kinematical variables see [6].

The physical interpretation of these variables is the following:

- $s$  - square of the energy in the centre of mass system
- $Q^2$  - square of the 4-momentum transfer, defines the resolution by which the electron probes the short distance structure of the nucleon
- $x$  - Björken scaling variable (in naive QPM momentum fraction of the nucleon carried by the struck quark)
- $y$  - scaling variable, describing energy transfer from the incoming to the outgoing lepton in the rest frame of the proton
- $W$  - total mass of the hadronic final state

### 1.3 Topological characteristics of NC DIS events

Due to the large difference between the electron and proton beam energies the shape of the phase space for the scattered lepton and quark is very elongated and very asymmetric events in the laboratory system will be produced. Most of the final state hadrons will be distributed in the forward direction, i.e. along the incoming proton.

Mainly the losses in the very forward direction (beam pipe effect) are responsible for the missing overlap between the HERA  $(x, Q^2)$  measurable domain and that of fixed targets experiments' domain [7].

The Jacquet-Blondel method [9] (J-B method) extends the measurable domain at HERA at high  $Q^2 \geq 100$  and at  $x \geq 0.01$ , but there still remains a gap which could be overlapped only by HERA running at smaller beam energies than the design ones.

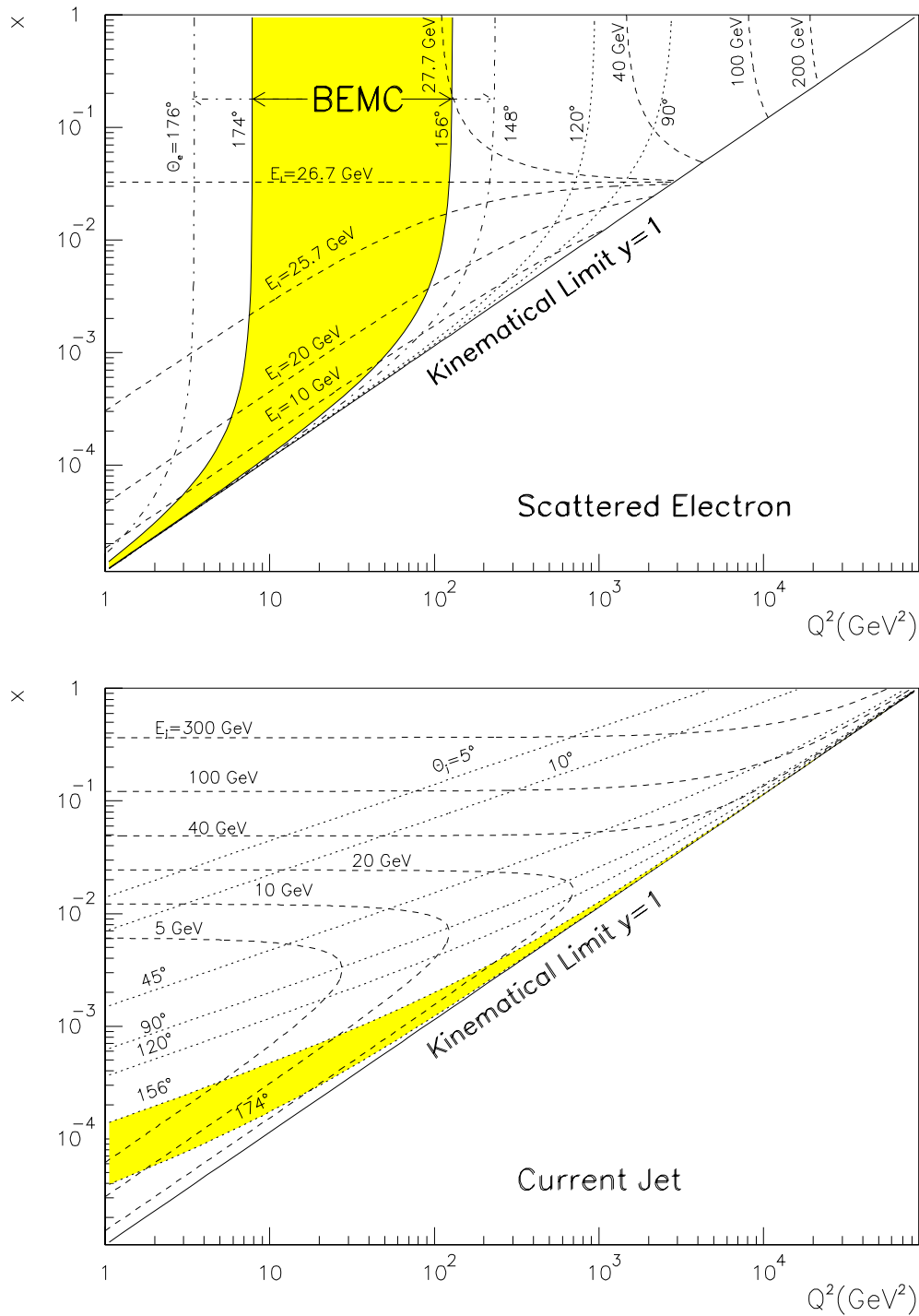


Figure 1.2: Scattering angle and secondary energy of electron and current jet. The angular acceptance of the BEMC is shown for both.

Kinematical equations can be illustrated in the  $(x, Q^2)$  plane by the isolines of constant electron  $\theta_e$  and hadronic current jet  $\theta_j$  scattering angles or by lines of constant electron and current jet energies  $E_e$ , resp.  $E_j$  (Fig. 1.2).

At high  $Q^2$  values electrons are scattered mainly into the central detector part and current jets are found in the central or forward detector part. In this kinematical region, from the trigger point of view, we rely on the liquid argon (LAr) electron trigger and eventually on a trigger based on the topological energy sums such as barrel or transversal energy.

For this kind of events also the tracker triggers will be very useful and this redundancy will be used for cross checking of the performance of the triggers.

Below  $Q^2 \approx 100 \text{ GeV}^2$  the electron will be scattered into the backward hemisphere, into the angular acceptance of the backward electromagnetic calorimeter (BEMC). The BEMC is integrated into the LAr trigger scheme, but it has also its own electron trigger (BSET) [53]. This trigger was designed with the aim to make a better use of the BEMC granularity, allowing efficient suppression of the high background rate. Electrons at very low  $Q^2$  ( $Q^2 \leq 5 - 10 \text{ GeV}^2$ ) are escaping in the beam pipe due to the BEMC angular acceptance limit  $\approx 175^\circ$ . A fraction of these events can be detected due to the smearing of the interaction vertex in  $z$  coordinate, i.e. along beams direction (see page 21). The region of low  $Q^2$  and very low  $x$ , i.e. where struck quarks are almost at rest since they carry only a tiny part of the proton momentum, can be considered as the fixed target HERA domain [7].

The characteristics of events at low  $x$  - high  $y$  values is that the hadron jet and scattered electron go both backwards under big scattering angles and with small electron energy. The smaller the electron energy, the bigger the energy of the hadronic jet accompanying the electron. This kinematic domain is the most difficult one for efficient NC DIS trigger due to the high rates of the beam-wall and photoproduction background events. Another very interesting feature of the HERA kinematics is the existence of the so called kinematic peak (see Fig. 8.2). From the relation between electron energies before and after scattering (1.2) and  $y$  as the measure of electron energy losses (1.3) one can find in the region of small  $y$  a wide range of practically constant electron energy  $E_e \simeq E_l$  (Fig. 1.2). This property enables precise energy calibration of the BEMC from the measured data.

## 1.4 Reconstruction of the kinematical variables

### 1.4.1 Introduction

Previous DIS experiments relied on the measurement of the scattered lepton to measure the internal structure of the nucleon.

HERA interactions resemble more a collision in the center of mass rather than a classical  $e^-p$  scattering, and more extensive use of hadronic flow measurement can be used than in the fixed target measurements. Three domains in the  $(x, Q^2)$  plane (Fig. 1.3) can be identified where the measurement is possible [10]:

- only electron measurement
- only hadrons measurement

- combined electron and hadrons measurement

The precision with which the kinematical variables can be reconstructed directly influences the measured differential cross sections. In different regions of the  $(x, Q^2)$  plane various systematic uncertainties affect the measurement. Main sources of the systematic errors are:

- absolute calibration of the energy measurement
- energy resolution
- detector alignment - scattering angle measurement

Measurement errors on the  $(x, Q^2)$  initiate so-called migration effects. The measured event rate in a given  $(x, Q^2)$  bin is not the true one. In fact it is a mixture of events migrating from the adjacent bins into this bin and the fraction of events remaining in this proper bin. The product of both migrations  $A(x, Q^2)$  is called *smeared acceptance*. The observed and true cross sections are then simply related by:

$$\sigma_{true}(x, Q^2) = \frac{\sigma_{obs}}{A(x, Q^2)} \quad (1.6)$$

The smeared acceptance depends on the detector resolution and also on the relative events rates in the bins.

### 1.4.2 Electron measurement only

This method of  $x$  and  $Q^2$  reconstruction from the energy and angle of the final state electron is the conventional one used in previous fixed target experiments. The most stringent limit to a precise measurement of structure functions is coming from the absolute energy calibration. The absolute energy scale must be known at the 1 – 2% level. A systematic calibration error of 1% generates a systematic shift of the differential cross section which rises inversely proportional to  $y$ , reaching already 10% at  $y \sim 0.1$  value [10]. The basic kinematical variables can be expressed in terms of the scattered electron energy  $E_l$  and angle  $\theta_l$  in the laboratory frame:

$$Q^2 = 4E_e E_l \cos^2 \frac{\theta_l}{2} \quad (1.7)$$

$$x = \frac{E_e E_l \cos^2(\theta_l/2)}{E_p(E_e - E_l \sin^2(\theta_l/2))} \quad (1.8)$$

$$y = \frac{E_e - E_l \sin^2(\theta_l/2)}{E_e} \quad (1.9)$$

From kinematical equations (1.7-1.9) we obtain the following relations for measured uncertainties:

$$\frac{\delta Q^2}{Q^2} = \frac{\delta E_l}{E_l} - \tan \frac{\theta_l}{2} \delta \theta \quad (1.10)$$

$$\frac{\delta x}{x} = \frac{1}{y} \frac{\delta E_l}{E_l} + \tan \frac{\theta_l}{2} \left( x \frac{E_p}{E_e} - 1 \right) \delta \theta \quad (1.11)$$

$$\frac{\delta y}{y} = \frac{y-1}{y} \frac{\delta E_l}{E_l} + \frac{1-y}{y} \cot \frac{\theta_l}{2} \delta \theta \quad (1.12)$$

The kinematical reconstruction from the electron variables is independent of any assumptions about the hadronic final state and for the  $x, Q^2$  measurement following consequences can be drawn [10]:

- The resolution in  $x$  at low  $y$  due to the factor  $1/y$  is very bad. Measurement of  $x$  at  $y$  below 0.1 is hardly achievable with sampling calorimeters
- It is important that this strong  $y$  dependence is independent from the incoming energies. It is therefore possible to extend, at given  $x$  and  $y$ , the region of precise measurement of  $x$  down to lower  $Q^2$  by running HERA at lower beam energies.
- The error on  $x$  due to the precision of the angle measurement is significant only at large  $x$  and low  $Q^2$
- At large  $y$  the electroweak radiative corrections to be applied are large (up to 100% of the Born cross section) and are the major limitation on the measurable highest  $Q^2$  at a given  $x$ .
- The  $Q^2$  measurement is very good with the possible exception at large angles ( $\theta \geq 170^\circ$ ), and only if the angular resolution is worse than a few *mr*ad [11].

### 1.4.3 Hadronic flow measurement only

Some limitations of the electron measurement can be overcome by kinematics reconstruction from the hadronic final state. A method to determine  $x$  and  $Q^2$ , proposed by A. Blondel and P. Jacquet [9], is based on two assumptions:

- $x$  and  $Q^2$  measurement from only outgoing hadronic flow is possible without using any jet identification algorithm or proton structure hypothesis
- for HERA kinematics, it is more suitable to express  $y$  and  $Q^2$  in terms of laboratory variables using the energy-momentum balance between lepton and hadronic system and then to deduce  $x$

Replacing the momentum transfer  $q$  in equation (1.4) by  $(p_h - P)$ , where  $p_h$  is the 4-momentum of the total outgoing hadronic system, gives:

$$y = \frac{P \cdot (p_h - P)}{P \cdot p_e} \quad (1.13)$$

with

$$p_h = \sum_h (E_h, p_{xh}, p_{yh}, p_{zh})$$

we obtain

$$y_{jb} = \sum_h \frac{E_h - p_{zh}}{2E_e} \quad (1.14)$$

Combining equations (1.7) and (1.9) we get on the lepton side:

$$Q^2 = \frac{(E_l \sin \theta_l)^2}{1 - y} \quad (1.15)$$

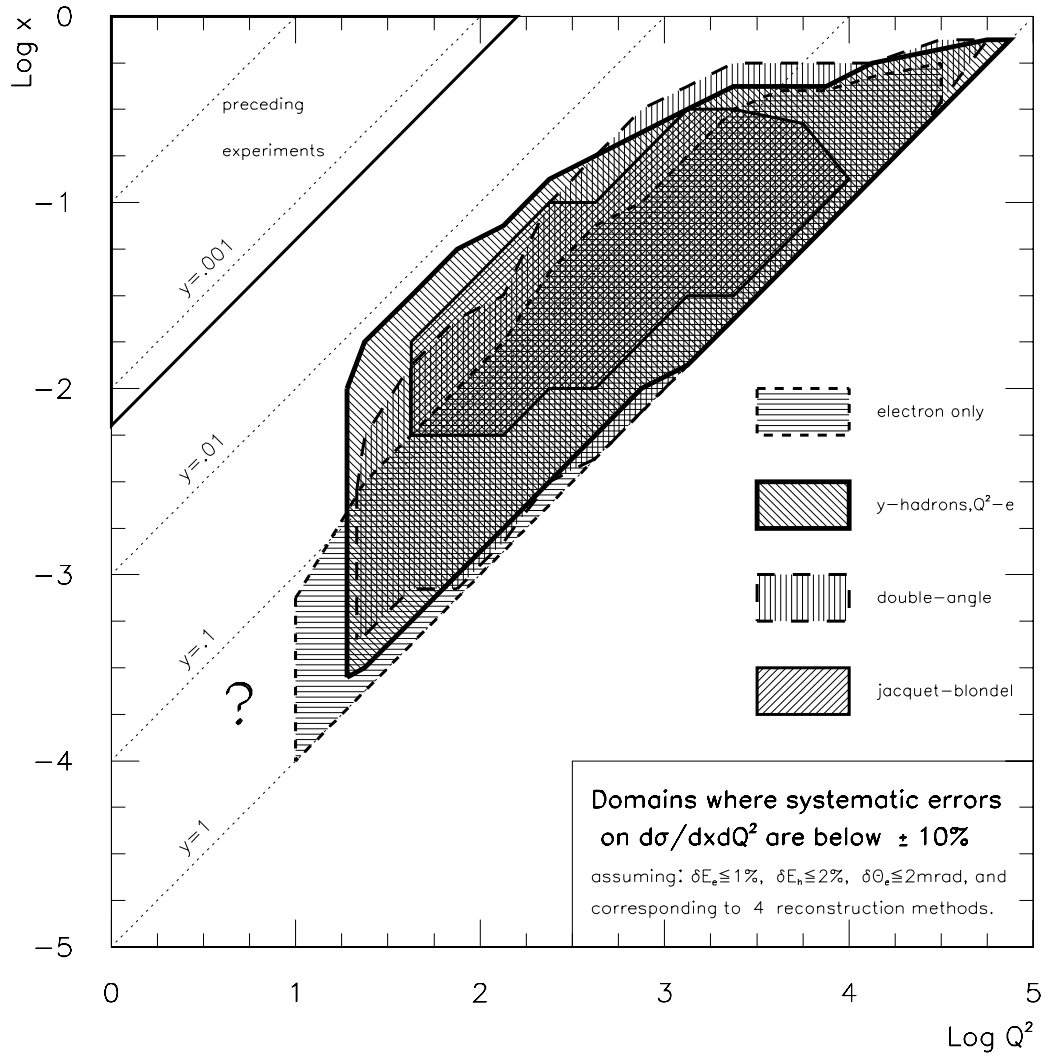


Figure 1.3: Kinematical regions (for electron beam  $E_e = 30 \text{ GeV}$ ) where different reconstruction methods can be used [11]. In the left upper corner the region studied by previous fixed target experiments is shown.

which on the hadronic side leads to:

$$Q_{jb}^2 = \frac{p_t^2}{1-y} = \frac{(\sum p_{th}^2)}{1-y} \quad (1.16)$$

where  $p_t$  is the total transverse momentum of the hadron flow and  $p_{th}^2$  is the transverse momentum of the hadron  $h$ .

It can be seen from equations (1.14) and (1.16), that the variables  $y$  and  $Q^2$  defined by J-B method are very well tailored for the HERA detectors, because the hadrons emitted into the very forward region (with the unavoidable beam pipe cut) contribute only very little to the measured  $y, Q^2$ .

#### 1.4.4 Combined methods from electron and hadrons measurements

From the measured energies and angles of the final state electron ( $E_l, \theta_l$ ) and current jet from the struck quark ( $E_j, \gamma_j$ ) one can combine another methods of the  $x, Q^2, y$  reconstruction. All methods are influenced differently by the detector effects. It turns out that only the so-called double angle method (measurement of  $\theta_l, \gamma_j$ ) and measurement of  $Q^2$  from  $E_l$  resp.  $y_{jb}$  by J-B method can provide the required precision [12].

When using the double angle method the reconstructed kinematical quantities are calculated from the following relations:

$$y_{\theta, \gamma} = \frac{\sin\theta(1 - \cos\gamma)}{\sin\gamma + \sin\theta - \sin(\gamma + \theta)} \quad (1.17)$$

$$Q_{\theta, \gamma}^2 = 4E_e^2 \frac{\sin\gamma(1 + \cos\theta)}{\sin\gamma + \sin\theta - \sin(\theta + \gamma)} \quad (1.18)$$

$$x_{\theta, \gamma} = \frac{E_e \sin\gamma + \sin\theta + \sin(\theta + \gamma)}{E_p \sin\gamma + \sin\theta - \sin(\theta + \gamma)} \quad (1.19)$$

The above mentioned method of *mixed* variables, i.e.  $Q^2$  is taken from electron measurement and  $y$  from the J-B method, leads to the using of the relations:

$$y_{mix} = y_{jb} \quad (1.20)$$

$$Q_{mix}^2 = Q_{el}^2 \quad (1.21)$$

$$x_{mix} = \frac{Q_{el}^2}{s y_{jb}} \quad (1.22)$$

The *mixed* method gives acceptable  $x, Q^2$  measurement in the region  $y \geq 0.01$  Fig. 1.3 [11].

## 1.5 Nucleon Structure Functions

### 1.5.1 Introduction

The first measurements of the the structure functions  $F_1$  and  $F_2$  made at the end of the 60's at SLAC marked the beginning of a modern era of nucleon structure investigations. Mainly two results of the experiments with high energy electron beams ( $E_e \rightarrow 20 GeV$ ) scattered off the nuclear targets indicated that a new structural level has been achieved:

- the measured cross section for scattering at large angles exceeded the expected one by more than one order of magnitude
- both structure functions  $F_1$  and  $F_2$  appeared to depend mainly on  $x$ ; moreover they tended to a finite value even when both  $Q^2$  and  $\nu$  were large, as long as the ratio  $Q^2/\nu$  was kept constant ( $x = \frac{Q^2}{2m_p\nu}$ )

The second result known as scaling of the nucleon structure functions, predicted by J.D. Björken [13], strongly contrasted with the properties of elastic form factors, which rapidly vanish with increasing  $Q^2$  [14]. The new phenomena were explained as an evidence for the pointlike structure of the nucleons (see [15]). The virtual photon, as a probe, can be scattered by the collection of quasifree pointlike, electrically charged objects - Feynman partons, later identified with the quarks (quark parton model - QPM).

In this picture the DIS cross-section is regarded as the incoherent sum of individual photon-parton cross-sections. In the high proton momentum limit ( $P \rightarrow \infty$ ) the Björken  $x$  variable is just the fraction of the proton's momentum carried by the elastically scattered parton. The size of this cross-section is then proportional to the probability  $q_f(x)$  of finding a quark of flavour  $f$  and the momentum  $xP$  in the proton.

Further experiments revealed some apparent inconsistencies in the simple QPM picture of the DIS. In 1972 it became clear that quarks carried only  $\sim 0.5$  of the proton's momentum [16] and in 1975 significant scaling violations were observed at SLAC and FERMILAB [17]. The explanation was provided by a non-abelian gauge theory of strong interactions: quantum chromodynamics (QCD). According to the QCD the nucleon contains not only charged partons (quarks) but also electrically neutral, massless, spin 1 objects, called gluons. Quarks in the nucleon interact with each other by exchanging the gluons which are the carriers of the strong force. For the structure functions it means that they are no longer dependent on  $x$  only but on both  $x$  and  $Q^2$ . The missing momentum fraction of the nucleon was also cured, it was attributed to the gluons.

In analogy with QED, quarks may radiate gluons ( $q \rightarrow qg$ ) and gluons may convert into  $q\bar{q}$  pairs ( $g \rightarrow q\bar{q}$ ). Unlike the electrically neutral QED photons, gluons, carrying colour charge, may couple directly to each other. Therefore in the QCD there exist additional diagrams of the  $g \rightarrow gg$  and  $gg \rightarrow gg$  type corresponding to the gluon selfcoupling. The interactions between quarks and gluons are governed by the QCD coupling constant which in the first loop approximation has the following form:

$$\alpha_s(Q^2) = \frac{12\pi}{(33 - 2N_f) \ln(Q^2/\Lambda^2)} \quad (1.23)$$

where  $N_f$  is the number of quark flavours and  $\Lambda$  is a mass scale parameter, the only free parameter in the theory to be determined from an experiment. As it is seen from (1.23) the QCD possesses the so-called asymptotic freedom property, i.e. when  $Q^2 \rightarrow \infty$  then  $\alpha_s \rightarrow 0$ , enabling perturbative calculations at sufficiently large  $Q^2$ . This way the QPM treatment of essentially free quarks is contained also in the QCD theory. The QPM became very successful in describing all processes with large momentum transfers (hard processes) from leptons to hadrons, or even from hadrons to hadrons and is considered as the Born approximation of the perturbative QCD theory. Non-perturbative approaches are these days still in their infancy. They face big technical, computational problems and yet do not have a strong predictive power.

The series of further DIS experiments at CERN (EMC, BCDMS) and FERMILAB, using beams of high energy muons and neutrinos, extended the SLAC measurements of the structure functions to the significantly higher values of  $Q^2$  ( $\rightarrow 200 \text{ GeV}^2$ ) and lower  $x$  values ( $> 0.01$ ). The HERA experiments are now pushing these limits of  $Q^2$  beyond  $10^4 \text{ GeV}^2$  and of  $x$  down to  $10^{-4}$ . This is a big leap towards the frontiers where the signs of a new physics are expected.

### 1.5.2 Structure Functions and Parton Distributions

The differential cross section for unpolarized  $e^-p \rightarrow e^-X$  scattering in lowest order of the electroweak coupling constant  $\alpha$  can be written in terms of three structure functions  $F_1(x, Q^2)$ ,  $F_2(x, Q^2)$  and  $F_3(x, Q^2)$ :

$$\frac{d^2\sigma}{dx dQ^2} = \frac{4\pi\alpha^2}{xQ^4} [xy^2 F_1(x, Q^2) + (1-y)F_2(x, Q^2) + (y - \frac{y^2}{2})x F_3(x, Q^2)] \quad (1.24)$$

For  $Q^2 < 500 \text{ GeV}^2$  the contribution to the cross section from the exchange of the  $Z^0$  boson is negligible and the  $x F_3$  structure function can be neglected [7]. The DIS cross section in the kinematical region considered is determined by the two structure functions  $F_1$  and  $F_2$ , which are related via  $2xF_1 = F_2/(1+R)$ :

$$\frac{d^2\sigma}{dx dQ^2} = \frac{2\pi\alpha^2}{xQ^4} [2(1-y) + \frac{y^2}{1+R}] F_2(x, Q^2) \quad (1.25)$$

Unlike real photons, the exchanged virtual photon can have a longitudinal as well as the transverse polarization. By  $R$  we denote the ratio of the corresponding cross sections  $\sigma_L$  and  $\sigma_T$  for the absorption of longitudinally and transversely polarized virtual photons.

$F_1$  and  $F_2$  can be unambiguously separated only from the measurements at different beam energies. If only a measurement at one energy is available, an assumption about the value of  $R$  has to be made.

The measured structure function  $F_2$  is in the QPM interpreted as a linear combination of the quark  $q_f(x, Q^2)$  and antiquark  $\bar{q}_f(x, Q^2)$  momentum distribution functions:

$$F_2(x, Q^2) = \sum_f A_f(Q^2) [x q_f(x, Q^2) + x \bar{q}_f(x, Q^2)] \quad (1.26)$$

The flavour-dependent coefficient  $A_f$  involves at low  $Q^2$  only the quark electric charge  $e_f^2$  and  $F_2$  reduces to the electromagnetic structure function  $F_2^{em}$ .

Specific quark distribution functions can be isolated from the so-called global fits [18], i.e. by combining the information from DIS experiments with different beams ( $e^-$ ,  $\mu$ ,  $\nu$ ,  $\bar{\nu}$ ). The procedure starts with parametrization of  $q_f$  at a sufficiently large  $Q_0^2 \sim 4 - 5 \text{ GeV}^2$ . Then the  $q_f(x, Q^2)$  can be calculated at higher  $Q^2$  from next-to-leading order (NLO) perturbative QCD. For example the MRS parametrization [18] of the parton distributions (valence, sea quark and gluon) at  $Q^2 = Q_0^2$  is of the form:

$$x u_v = N_1 x^{\eta_1} (1-x)^{\eta_2} (1 + \eta_3 x) \quad (1.27)$$

$$x d_v = N_2 x^{\eta_4} (1-x)^{\eta_5} (1 + \eta_6 x) \quad (1.28)$$

$$2x(\bar{u} + \bar{d} + \bar{s}) = A_s x^{-\lambda} (1-x)^{\eta_s} \quad (1.29)$$

$$xg = A_g x^{-\lambda} (1-x)^{\eta_g} \quad (1.30)$$

where  $u_v = u - \bar{u}$  etc. There are thus more than 10 parameters ( $\eta_i, A_s, (A_g), \lambda_{QCD}$ ) to be determined by the data for  $Q^2 > Q_0^2$ . The coefficients  $N_1$  and  $N_2$  are fixed by the flavour sum rules, and  $A_g$  (or  $A_s$ ) by the momentum sum rule. Usually it is assumed that the sea quarks distributions satisfy the  $\bar{u} = \bar{d} = 2\bar{s}$  condition. Recent NMC data [19], violating the Gottfried sum rule, initiated big discussions on the precise  $u$  and  $d$  content of the sea. The contribution of heavy sea quarks ( $c$  and  $b$ ) is usually included via gluon annihilation process  $g \rightarrow Q\bar{Q}$ .

Gluon distribution is a dominating component in the low  $x$  DIS. It has been difficult to measure its properties due to the absence of direct coupling between the gluon and the electroweak bosons. At low  $x$  we enter the region where non-perturbative effects starts to play a non negligible role and therefore measurements at HERA are supposed to be a challenge for theoretical physicists to solve the QCD in the non-perturbative regime. Naive QPM and Regge theory (with  $\alpha_P = 1$ ) imply that  $\lambda = 0$ . However there are good theoretical reasons why  $\lambda$  may be as large as 0.5, as will be discussed in the next section.

### 1.5.3 Structure Functions at Low $x$

The  $x$  and  $Q^2$  dependence of parton distributions at very small  $x$ , where the dynamics of DIS becomes dominated by the gluons, is one of the most promising domains in QCD [10]. A large amount of different sets of structure function parametrisations exist today (see e.g. [20]) describing rather well the available experimental data. But extrapolation to low  $x$  gives rise to huge discrepancies among the different parametrisations. The theoretical interpretation is not unambiguous today and first data already brought constraints, which allow to exclude some of the most diverging predictions [36].

In the domain of standard DIS ( $Q^2 \rightarrow \infty$  at fixed  $x$ ) we have a rather good (complete) understanding of QCD dynamics. Standard QCD evolution equations of Gribov, Lipatov, Altarelli and Parisi (GLAP) [21] are based upon solid tools of field theory. Splitting functions, considered as the central elements of this approach, describe a cascade of quarks and gluons decays. In this process partons loose longitudinal momentum but gain transversal one (virtuality). In the region of small  $x$  and  $Q^2$  the evolution gets dominated by gluons alone and the gluon splitting functions should be replaced by the so-called Fadin-Kuraev-Lipatov kernel (FKL) [22] which describes more precisely the main contribution  $\alpha_s \ln 1/x \cdot \phi(q^2)$  with the exact function  $\phi(q^2)$  (not only the approximate term  $\phi(q^2) \sim \ln q^2$  which leads to the  $\ln q^2$  dependence as in the GLAP case). Numerical studies [23] indicate that for the gluon distribution the differences between GLAP and FKL are small at HERA energies. Characteristic behaviour of parton distributions at low  $x$  in the perturbative QCD results from the summation of soft gluon emissions via the GLAP or FKL equations. It gives at small  $x \ll 1$ ,  $\lambda = 12\alpha_s \ln 2/\pi$  at fixed coupling  $\alpha_s$ . So the expected gluon and sea quark distributions behave as

$$xg(xq_{sea}) \sim x^{-\lambda} \quad (1.31)$$

where  $\lambda \simeq 0.5$ .

As  $x$  decreases the standard QCD predicts a very strong rise of the density of slow gluons. At very low  $x$  a serious conflict appears: the total cross section for the scattering of a virtual photon off the proton rises faster than the unitarity limit. In other words it means that gluon density seen by the photon probe gets unphysically large. If the density of gluons within the proton becomes too large they can no longer be treated as free partons. This is an indication that the standard QCD description is not valid at  $x \rightarrow 0$ ! Here one expects that transition from the region of perturbative QCD to the Regge limit of DIS cross sections takes place [24]. In this new regime the evolution equations must go beyond  $LL(Q^2)$  perturbation approximations and reach the new regime ( $\frac{s}{Q^2} \approx \frac{1}{x} \rightarrow \infty$ ) at fixed  $Q^2$ . Nevertheless if  $Q^2 > Q_0^2$  this new regime may be studied in the framework of the perturbative QCD.

According to the proposed scenario annihilation and recombination of parton pairs are responsible for the damping of the singular growth predicted by the standard QCD. Gribov, Levin and Ryskin have tried to add a negative nonlinear term to the GLAP equation [24], leading to the GLR equation, in order to treat this effect of "screening" or "shadowing" also theoretically. At this point one should stress however that the nonlinear GLR equation is derived from the study of a set of Feynman diagrams and that there is no firm theoretical basis to use it in the nonperturbative region. The GLR equation can be used for the first estimate of the boundary line between the LLA and this new perturbative QCD regions (Fig. 1.4). According to this estimation we should already at HERA reach this new region. One hopes that signs of the new physics could be unveiled [26].

For low  $Q^2 \approx O(1) \text{ GeV}^2$  in the nonperturbative region, the Regge theory is used to describe the known phenomena. The input gluon distributions <sup>2</sup> in the structure function analysis traditionally derived from the naive Regge parton model have the following form

$$xg \sim x^{1-\alpha_P(0)} \sim \text{constant} \quad (1.32)$$

with the Pomeron intercept  $\alpha_P(0) \simeq 1$ .

Form (1.32) is unstable with the evolution in  $Q^2$  (with increasing  $Q^2$  it develops spikes at small  $x$ ) and if one puts (1.23) for rather large  $Q^2 \simeq 4 - 10 \text{ GeV}^2$  then with decreasing  $Q^2$  the structure function soon becomes negative at small  $x$ . If verified experimentally, behaviour (1.31) would be a manifestation of the so-called "Lipatov" [24] or "hard" QCD pomeron with  $\alpha_p - 1 = \lambda$ . Unlike (1.32), behaviour (1.31) is stable with evolution in  $Q^2$ .

A short summary of the situation is shown on the Fig. 1.4. From the theoretical point of view the  $(Q^2, x)$ -plane can be divided into four regions, where different "physics" should dominate ([24],[27]):

- region A - standard DIS, perturbative QCD in  $LL(Q^2)$  approximation is valid
- region B - transition region, leading log perturbative QCD still could be applied but with some restrictions or in a more sophisticated form (nonlinear term in the evolution equation)
- region C - no QCD-based theory yet, but perturbative QCD still should work
- region D - nonperturbative QCD region

---

<sup>2</sup>If one can talk about the gluon distribution in this nonperturbative region, but this language is widely used in the literature (see [25]).

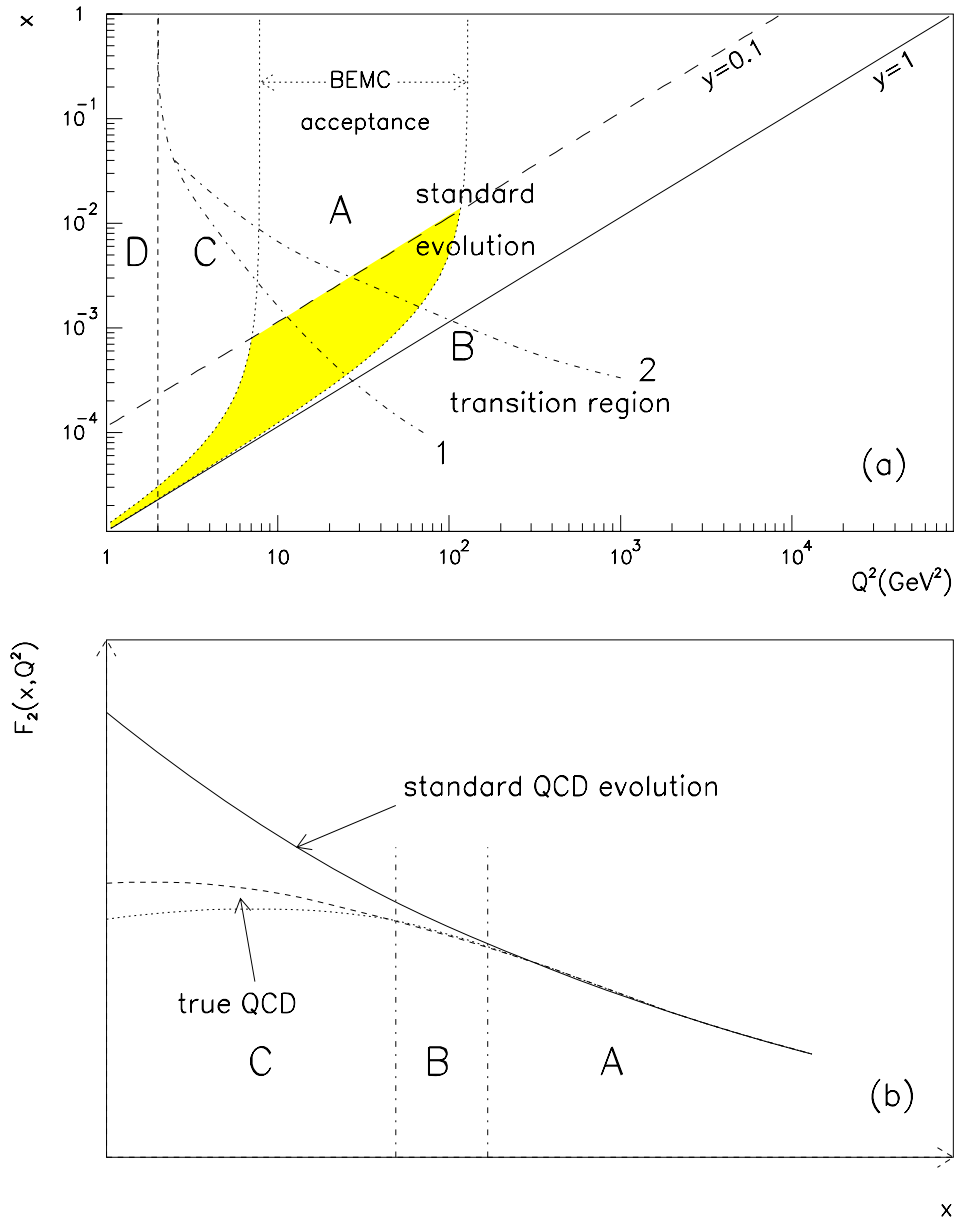


Figure 1.4: (a) Estimation of the  $(Q^2, x)$ -plane division into LLA and nonperturbative regions according to the GLR equation. The shaded area shows the region, where  $F_2$  is measurable with the BEMC. (b) Sketch of  $F_2(x, Q^2)$  evolution at fixed  $Q^2$  according to the standard perturbative QCD. In both regions B and C the structure function should lie below the extrapolation, but the precise behaviour cannot be predicted at present.

**Experimental identification of a new regime** There is no doubt that the measurements at HERA will eliminate a lot of at present available  $F_2$  parametrizations. However an unambiguous physical interpretation of these results will be probably impossible from the  $F_2$  measurement alone [27]. A major problem in unambiguous identification of a new regime from the  $F_2(x, Q^2)$  measurements at small  $x$  alone lies in the fact that our knowledge of the nonperturbative regime is very poor and therefore:

- predictions are simply phenomenological extrapolations
- they depend on:
  - a set of "starting" distributions,  $f_a(x, Q^2)$ , as a function of  $x$  at some  $Q^2 = Q_0^2$ .
  - the presence and size of the screening corrections

As a result, we cannot be certain whether an observed steep behaviour at  $x \sim 10^{-3}$  is a manifestation of the Lipatov perturbative effects or if it is due to the  $Q^2$  evolution of the nonperturbative input  $x$  distribution. On the other hand it will be difficult to decide if the saturation of the structure function is due to the strong screening effect or to the initial flat gluon behaviour at  $Q^2 = Q_0^2$ .

Several alternative, dedicated measurements have been proposed to search for the unambiguous identification of the regime dominating the studied process as e.g. hot spots measurements [26], heavy photon dissociation [29], rapidity correlations between hadrons produced in DIS [30] or diffractive  $ep$  scattering [31].

## 1.6 Beyond DIS

HERA physics is of course not limited to the DIS. Although the aim of this thesis is to study the NC DIS, we want at least to mention some of the exciting topics accessible already with a rather limited statistics, as e.g.:

**Photoproduction** The largest event rate at HERA is expected from the collisions of almost real photons ( $Q^2 \rightarrow 0 \text{ GeV}^2$ ) with protons. The study of hard scattering reactions in photoproduction is of great theoretical and experimental interest. These  $\gamma p$  processes could reveal the anticipated internal structure of the photons. Total photoproduction cross section measurement is at HERA accessible in a range from about 100 to 250 GeV  $\gamma p$  c.m.s. energy, i.e. extending the measured domain by more than one order of magnitude [32].

Current extrapolations of the total cross sections towards HERA energies differ substantially, therefore these values are awaited with great interest [32]. First measurements [34] are in good agreement with the Regge motivated parametrizations and seem to disfavour extreme 'minijet' models.

**Hadronic final states** DIS at HERA is a more complicated process than  $e^+e^-$  annihilation, but not so "messy" as at hadron colliders. Hadronic final states in leptonproduction have been studied experimentally up to invariant mass  $W \simeq 25 \text{ GeV}$  only. Processes with very high  $Q^2 \rightarrow 10^4 \text{ GeV}^2$  accessible at HERA provide a large phase space for gluon radiation. This means appearance of multijet final states and the strong coupling constant

from relative rates of these multijets events will be measurable. However this advantage is partially reduced by the big boost of the center of mass into the proton direction. This has consequences for the precise measurement of the hadronic jets in the very forward region. Among phenomena related to the QCD accessible at HERA one can mention e.g.: initial QCD radiation, hard parton emission, non-perturbative hadronization and confinement etc.

**Beyond the Standard Model** The large  $\sqrt{s}$  energies and large momentum transfer reachable at HERA give the possibilities of observing new particles and interactions, and smaller scale structures which would provide signals for physics beyond the Standard Model.

In particular s-channel resonances in the electron-quark system, such as leptoquarks, predicted in a number of different theoretical scenarios (composite models, GUT theories), are candidates particularly suited for HERA. Since the present experimental limits are accessible at HERA, HERA has the potential for leptoquark or leptogluon discovery or at least for a significant improvement of the present experimental bounds [33]. First results from H1 point to an experimental limit of  $145 - 192 \text{ GeV}$  for leptoquarks from the fusion of an electron and quark, resp. to the mass limit of  $98 - 121 \text{ GeV}$  for leptoquarks formed with an antiquark. Up to now no evidence for leptogluons was found [38]. Among other processes it is also worthwhile to mention e.g. [39]:

- single production of new fermions (excited leptons)
- pair production of new particles (slepton, squark)
- the study of effects from new *virtual* particle exchanges (new gauge bosons)

## Chapter 2

# H1 Detector

## 2.1 Introduction

The event topology of HERA collisions requires an asymmetric detector design since the center of mass of the collision is strongly boosted along the proton direction and consequently high particle densities and high energies are expected in the forward region.

Head on collisions of electron and proton bunches occur in the interaction region extending to  $\pm 50$  cm along the beam axis, with respect to the nominal interaction point ( $z = 0$  cm). This *z-vertex spread* of the position of the interaction point position is due to the fact that the proton bunches are long (50 – 200 cm).<sup>1</sup>

The innermost part of the H1 detector Fig. 2.1 is equipped with a central (2) and forward tracking (3) system. A liquid argon calorimeter consisting of an electromagnetic (4) and a hadronic (5) section surrounds the tracking system and ensures good hermeticity in the central and forward region. The backward region (see Fig. 2.3) is closed by the backward proportional chamber (BPC), the backward electromagnetic calorimeter (BEMC) (12) and the two scintillator walls (time of flight detectors - TOF). The very forward direction around the beam pipe is closed by the plug calorimeter (13).

A superconducting coil (6) with a diameter of 6 m provides a magnetic field of 1.2 Tesla. This field is compensated by another superconducting coil (7) in order not to influence the HERA machine.

The magnetic flux is returned by the iron yoke (10). This yoke is interleaved with limited streamer tubes to measure the hadronic energy leakage. Muons are identified and measured by muon chambers (9) inside and outside the iron. Measurement of muon tracks in the forward region is done in the toroid (11) equipped with drift chambers.

The H1 detector is completed with the small angle electron and photon detectors placed at 33.4 and 102.9 m respectively from the nominal interaction point in the HERA tunnel, downstream of the electron beam.

In the next section we discuss the major components in more details.

## 2.2 Calorimetry

The H1-calorimetry is based on a large liquid argon (LAr) calorimeter, backed up by an iron tail catcher and closed by a warm backward electromagnetic calorimeter (BEMC) and a forward plug calorimeter. Electron and photon crystal detectors in the HERA tunnel are completing the H1 calorimeter system.

Basic parameters of the H1 calorimeters are summarized in the tables 2.1 and 2.2 [41].

---

<sup>1</sup>Length of the electron bunches is  $\sim 1$  cm.

## HERA Experiment H1

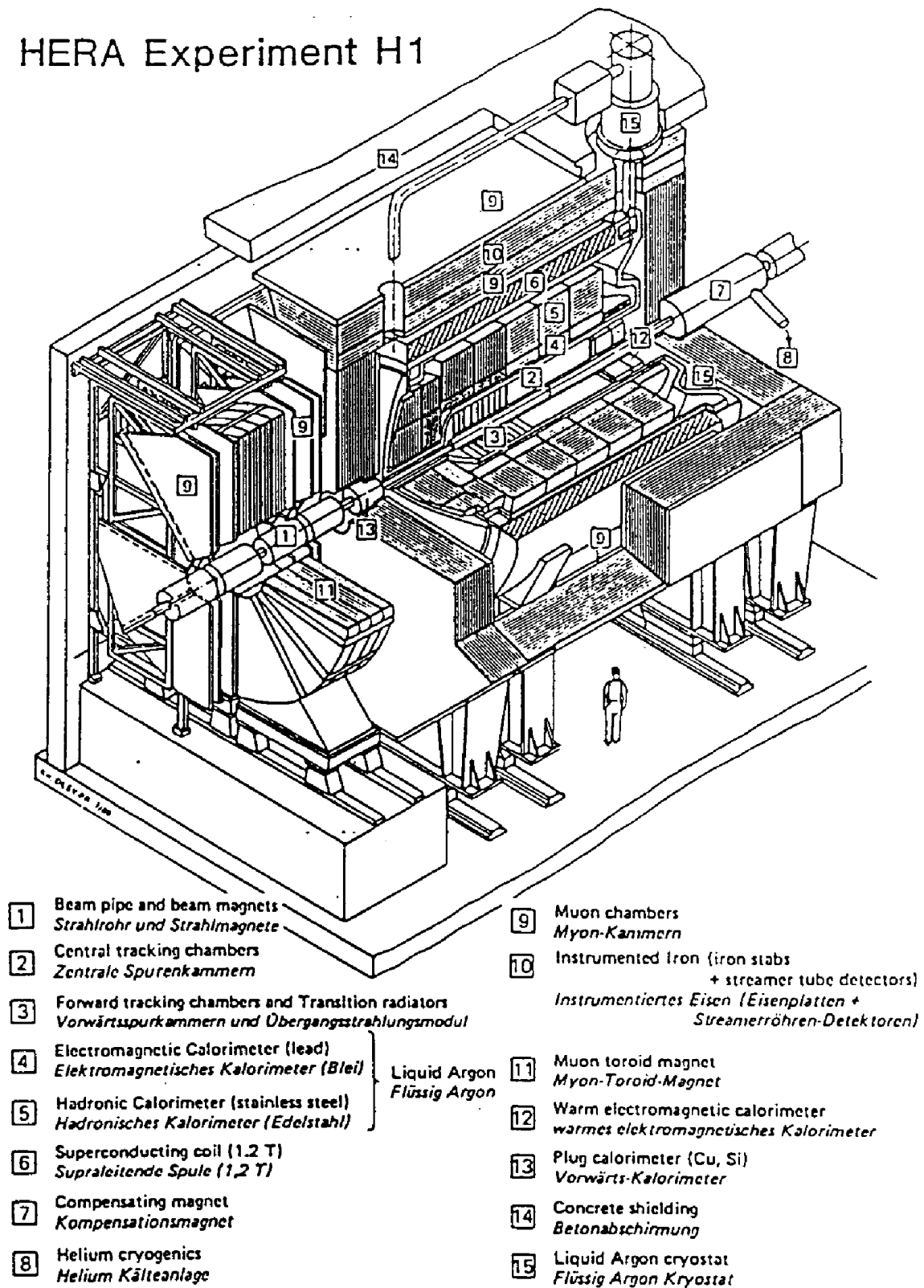


Figure 2.1: H1 - detector at HERA

Detector	Depth $X_0$	Depth $\lambda$	Transversal granularity $[cm]^2$	# of channels
LAr em	30-20	1	10-100	30784
LAr had	-	6-4	50-2000	13568
BEMC	22	1	250	88
Plug	-	4.3 (6.7)	25	336
Tail catcher	-	4.5	2500	4000
e-Tagger	21	-	5	49
$\gamma$ -detector	21	-	4	25

Table 2.1: Basic parameters of H1 calorimeters

Detector	Calibration $\Delta E/E[\%]$	A $[\%GeV^{1/2}]$	B $[GeV]$	C $[\%]$
LAr em	$\pm 1$	$11.2 \pm .05$	$.152 \pm .004$	$.64 \pm .07$
LAr had	$\pm 2$	$46.1 \pm .7$	$.73 \pm .03$	$2.6 \pm .2$
BEMC	$< \pm 3$	10.0	-	-
Plug	-	$\approx 110$	-	-
Tail catcher	-	100	-	-
e-Tagger	$< \pm 1$	10	-	1.0

Table 2.2: Energy calibration and resolution:  $\sigma/E = \sqrt{A^2/E + B^2/E^2 + C}$ 

### 2.2.1 Liquid Argon Calorimeter

The choice of the LAr for the main calorimeter was motivated by the requirements of [3]:

- longterm stability of response ( $\leq 1\%$  and  $\leq 2\%$  for electromagnetic resp. hadronic part) and easy calibration
- homogeneity of response
- $e/\pi$  rejection  $\leq 10^{-3}$  (requiring fine longitudinal segmentation)
- good angular resolution for jet directions measurements mainly in the forward region (requiring fine transversal granularity)
- energy resolution of electromagnetic part  $\sigma/E \approx 10\%/\sqrt{E}$
- energy resolution of hadronic part  $\sigma/E \approx 50\%/\sqrt{E}$

The design optimizes calorimeter homogeneity in order to reduce the effects from cracks and support structures (dead material). This is achieved by minimalized cracks between electromagnetic parts, and the cracks between hadronic sections have non-projective geometry. The LAr calorimeter consists of 8 independent modules (wheels) assembled along

the beamline [3]. Each of these wheels has 8 electromagnetic and 8 hadronic stacks. The only exception is the backward barrel electromagnetic (BBE) part, which has no hadronic part. The sampling structure in the electromagnetic part is built from 2.4 mm thick Pb absorber plates and 2.35 mm LAr gaps as active medium. The signal is readout by one plane of pad boards per gap.

The basic structure of the hadronic part consist of a 16 mm thick stainless steel absorber and a double gap of  $2 \times 2.4 \text{ mm}$  LAr from both sides of the absorber containing a double sided pad read out board [40].

Total depths of  $20 - 30 X_0$  and  $4.5 - 8 \lambda_0$  are designed to ensure full absorption of the electromagnetic and hadronic showers with minimal leakage into the tail catcher calorimeter.

The hadronic calorimeter is not compensating, i.e. the  $e/h$  ratio response is not one, therefore a software weighting procedure is used [44]. The weighting can be used because of the fine granularity in both longitudinal and lateral directions.

### 2.2.2 BEMC

The BEMC is a warm sampling calorimeter in the backward region of the H1 detector ( $156^\circ < \theta < 174^\circ$ ) (Fig. 2.3) which is not covered by the main liquid argon calorimeter (for more details see [47]). The BEMC is exposed to the magnetic field of 1.2 T of the H1 detector and its primary task is to measure energies of electrons scattered under small angles (in H1 convention  $\theta > 156^\circ$ ) from the deep inelastic processes (see Fig. 1.2).

The sampling structure is built from 2.5 mm Pb and 4 mm SCSN38 scintillator plates. While the total depth of the calorimeter in units of radiation length is  $22.5 X_0$ , the corresponding nuclear interaction length is only  $\approx 1 \lambda_0$ . This means that the BEMC is an electromagnetic calorimeter without containment for hadrons. The sampling structures are assembled in 88 stainless steel boxes (stacks) (Fig. 2.2). Most of them (56) have a regular rectangular shape  $15.9 \times 15.9 \text{ cm}^2$ . The stacks at the edge are completing the cylindrical shape of the BEMC and therefore are of a smaller size and of a irregular shapes (big and small trapezoids and triangles).

The light signal from the scintillator layers is collected and guided to the Hamamatsu S2575 silicon photodiodes by Y7 wavelength shifters (WLS).

There are 2 basic types for the geometrical arrangement of WLS - WLS covering the whole length and WLS which cover only the last third of the stack length. The first ones are called "electromagnetic" (EM) and the second ones "hadronic" (HAD) or backward channels. All stacks have 4 EM channels with the exception of small triangles with only 3 EM channels. Each quadratic stack and each big trapezoid one has in addition 2 HAD channels. In total there are 64 stacks with "hadronic" readout.

### 2.2.3 Plug Calorimeter

The plug calorimeter was built with the aim to minimize the missing part of the total transverse momentum due to the hadrons from the proton fragmentation, emitted close to the beam axis. This calorimeter is however placed behind larger amounts of dead material of beam pipe, LAr cryostat and of the FTD. Therefore only a moderate energy resolution for hadronic showers is required ( $\sigma/E = 100\%/\sqrt{E_h}$ ).

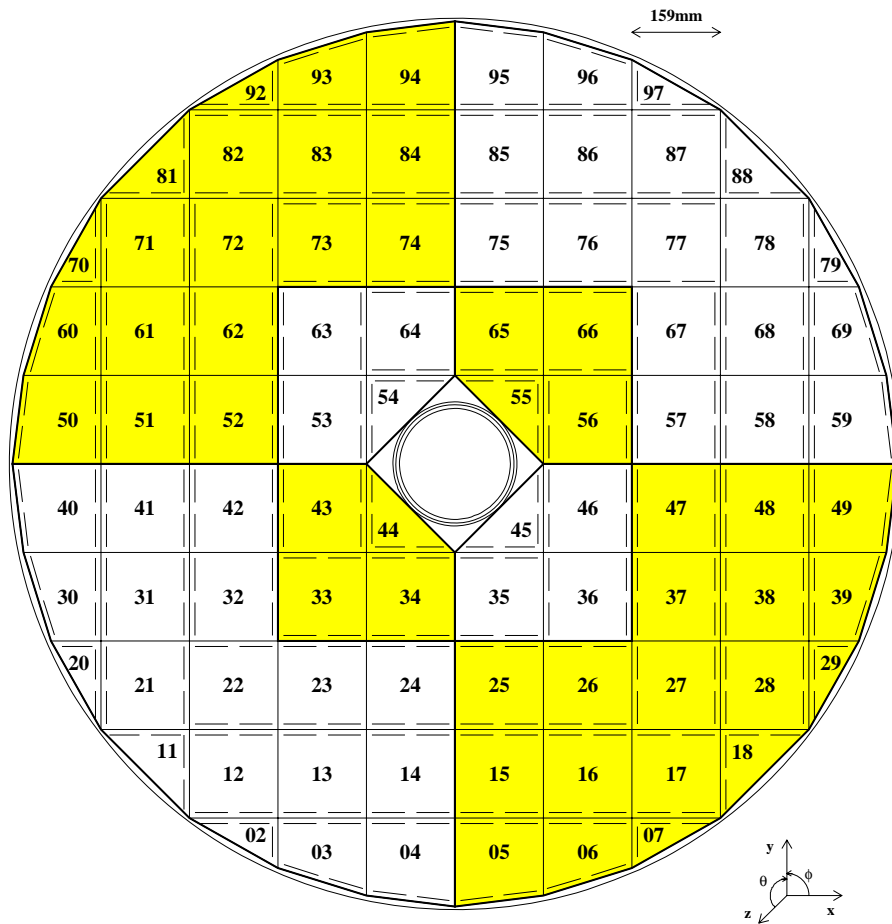


Figure 2.2: BEMC - a frontface view from the H1 interaction point. Stack structure with the position of long wavelength shifters and numbering scheme are shown. Shaded and white areas indicate 8 trigger big towers (BT) readout by the LAr trigger.

Due to the space limitations a very compact calorimeter design, consisting of a silicon-instrumented sandwich, was used. The plug calorimeter is built of 8 layers, each layer consisting of a 7.5 cm Cu plates and 300  $\mu\text{m}$  Si-pad detector. The total length of the instrumented part is 65 cm which corresponds to  $4.3\lambda$ . The lateral size of the basic detector cell is  $5 \times 5 \text{ cm}^2$  and the radial acceptance of the plug is  $6 \text{ cm} \leq r \leq 25 \text{ cm}$  or in angular units  $12.5 \text{ mrad} \leq \theta \leq 60 \text{ mrad}$ .

### 2.2.4 Tail catcher calorimeter (TC)

The hadronic energy leaking out of the main calorimeters is measured by a limited streamer tube (LST) detector [45]. The basic elements of the LST chambers are 8-fold profiles with a cell size of  $9 \times 9 \text{ mm}^2$ . Signals are readout from wires and strips simultaneously. A nonflammable gas mixture of  $\text{CO}_2$ , Isobutane and Argon is used (88.5%, 9.5%, 2.5%) instead of standard Argon-Isobutane mixture. For the detector installation the slits in the iron yoke of the main solenoid magnet are used (instrumented iron). The LAr calorimeter is thus backed by another  $4.5\lambda$  of the tail catcher. The requirements for the hadronic energy resolution measurement are very moderate ( $\sigma/\sqrt{E_h} \approx 100\%$ ). The tail catcher should detect only a small fraction of the jet energies. In more than 95% of the events the energy leakage into the tail catcher is less than 20% [3].

For the calorimetric part of the LST system (11 layers) the analogue signals from the pads are summed into towers and are read out through the LAr DAQ chain.

### 2.2.5 Luminosity Monitor and Electron Tagger

The small angle electron and photon shower counter hodoscopes located at respectively 33.4 and 102.9  $m$  downstream of the interaction point have three separate tasks:

- luminosity measurement of the  $e^-p$  collisions
- identification and measurement of photoproduction processes
- tagging of radiative events

Both detectors, also called *luminosity detectors*, are built from matrices of KRS-15 crystals (78%  $\text{TlCl}$ , 22%  $\text{TlBr}$ ). The electron tagger (ET), with angular acceptance  $0 - 5.0 \text{ mrad}$ , is built from a matrix of  $7 \times 7$  and the photon detector (PD) consists of a matrix of only  $5 \times 5$  crystals (for details see table 2.1). Fine granularity and good energy resolution are vital for the electron tagging to study the photoproduction processes with almost real photons.

The luminosity system is completed with the  $2 X_0 \text{ Pb}$  filter (protection against synchrotron radiation) followed by the  $1 X_0$  water Cerenkov counter in front of PD.

## 2.3 Tracking Detectors

Due to the specific HERA kinematics the tracking detectors are divided into two main parts, central and forward.

The extended interaction region is surrounded by the Central Tracking Detectors (CTD) and the forward direction is covered by the Forward Tracking Detectors (FTD).

The tracking possibilities are completed with the backward proportional chamber (BPC) in front of the BEMC. The BPC is a module containing 4 wire planes rotated by  $45^\circ$  with respect to each other.

In the FTD two types of forward chamber modules (radial - and planar - drift chambers) are chosen to find tracks in the region where pattern recognition is expected to be difficult. The forward trackers are grouped into 3 identical supermodules, each one built from a planar drift chamber (FWP), a MWPC, a transition radiation volume and a radial drift chamber (FWR).

The radial chambers give a precise determination of the  $\phi$  coordinate and space points are defined by the planars with different wire orientations.

The CTD is a system of proportional and drift chambers designed to fit the innermost cylindrical volume of the H1 detector (Fig. 2.3). Starting from the interaction point a particle is detected by the multiwire proportional chambers (MWPC), called CIP (central inner proportional chamber), followed by the central inner z-chamber (CIZ), the inner jet chamber (CJC1), the outer z-chamber (COZ), the outer MWPC (COP) and the outer jet chamber (CJC2).

Chamber	r [cm]	$z_{min}$ [cm]	$z_{max}$ [cm]	$\sigma_{r\phi}$ [mm]	$\sigma_z$ [mm]	$\sigma_r$ [mm]	$\sigma_{x,y}$ [mm]
CIP	15.3-17.2	-112.5	106.5	-	-	-	-
CIZ	17.4-20.0	-108	72	25	0.25	-	-
CJC1,CJC2	21.5-76.9	-112.5	107.5	0.21	23.5	-	-
COZ	46-49	-110.5	105.5	58	0.34	-	-
COP	50-53	-110.7	106.5	-	-	-	-
FWR	15-75	-	-	0.17	-	29.0	-
FWP	15-75	-	-	-	-	-	0.21
BPC	13.5-65	-144	-138	-	-	-	2.0

Table 2.3: Tracking detectors sensitive regions ( $r,z$ ) and resolutions ( $\sigma_{r,\phi,z,x,y}$ ) as obtained from the first luminosity runs at HERA [41].

The CIP and COP chambers have a good time resolution ( $60 ns$ ) and provide an independent determination of the bunch crossing time ( $t_0$ ) for the trigger.

The task of the central drift chamber (two rings of tilted jet chambers) is a precise measurement of  $r,\phi$  coordinates of charged tracks ( $\sigma_{r\phi} = 100 \mu m$ ) and a moderate  $z$  measurement from the charge division ( $\sigma_z = 24 mm$ ). Additionally, ionization energy measurement for charged particle identification with the design resolution  $dE/dx \approx 6\%$  should be available [3].

Precise  $z$ -measurement is provided by CIZ and COZ - two sets of separated proportional  $z$ -chambers. The CIZ and COZ wires are stretched in a polygon installed around the CIP resp. COP. The drift direction is parallel to the beam axis and the expected  $z$ -resolution is  $\sigma_z \leq 350 \mu m$ .

The design momentum resolution of the CJC chambers is  $\sigma_{p\perp}/p_{\perp}^2 \simeq 3 \cdot 10^{-3} GeV^{-1}$  with the gas mixture 50%Ar, 50% $C_2H_6$ . For safety reasons in the first periods of data taking the gas mixture of 89.5% Ar, 9.5%  $CO_2$  and 1%  $CH_4$  was used. The achieved

momentum resolution was  $\simeq 10^{-2} \text{ GeV}^{-1}$ , and the  $dE/dx$  resolution amounts to about 10%.

The basic parameters of the tracking detectors are summarized in the table 2.3.

## 2.4 Muon Detectors

### 2.4.1 Instrumented iron

Muons in the central region are measured by the instrumented iron detector. *Muon chambers* are LST layers with digital read-out of the anode wires.

### 2.4.2 Forward Muon Spectrometer

In order to measure muon momenta in the very forward direction ( $3^\circ \leq \theta \leq 17^\circ$ ) with sufficient precision a separate forward muon spectrometer (FMS) was built. The heart of the FMS is a toroid magnet with length of 1.2 m and field of 1.5 Tesla. Before and after this magnet 2 arrays, each consisting of 6 drift chambers, are installed. The drift chambers drift cells' lengths vary between 0.4 m and 2.4 m. The maximum drift distance is 6 cm and the coordinate along the sense wire is obtained from charge division measurement. Two of the double planes on either side of the toroid measure the polar angle  $\theta$  and the remaining ones the azimuthal angle  $\phi$ . The chambers are arranged in pairs with a relative shift of the sense wires by half of the drift length (3 cm). This geometrical arrangement resolves left-right ambiguities and provides a checksum (the sum of the drift times from the two offset planes) to facilitate recognition of good tracks and reject large angle punch-through. Correlated position and angle measurements for tracks at the exit of the solenoid return yoke reduce the ambiguities in linking with tracks in the central chambers. First measurements with halo muons from the proton beam showed a spatial resolution of  $\sigma \leq 0.35 \text{ mm}$ . The momentum resolution is expected to be  $\sigma_p/p \approx 23 - 32\%$  for muons in the energy range of 25-150 GeV [41]. The resolution on the lower edge is limited by the multiple Coulomb scattering.

## 2.5 Scintillators

### 2.5.1 TOF

The time of flight (TOF) counter system placed behind the BEMC detector (Fig. 2.3) is vital for vetoing beam-gas and beam-wall background events initiated by the proton beam. The TOF itself consists of four planes of NE104 scintillator elements. Two pairs of planes create the inner and outer part of the TOF wall. The wall closer to BEMC (TOF1) is at  $z = -193.7, -198.7 \text{ cm}$  and consists of 16 scintillator elements, each of  $31.7 \times 31.7 \times 2 \text{ cm}^3$  size. The second wall further from BEMC (TOF0) located at  $z = -224.3, -229.3 \text{ cm}$ , is of bigger granularity with only 8 scintillator elements, each of  $25 \times 50 \times 2 \text{ cm}^3$  size. Short maximal light paths  $\approx 22.4 \text{ cm}$ , resp.  $28 \text{ cm}$  are an inevitable prerequisite for very good time resolution. A measured resolution of individual scintillator plates  $\sigma \approx 1 \text{ ns}$  [63] ensures the TOF capability to distinguish between events originating in the interaction region and the background events originating outside, upstream of the proton beam.

### 2.5.2 Veto Walls

The big and small veto walls, at  $z = -6.5\text{ m}$  resp. at  $z = -8.0\text{ m}$ , are built with the aim to veto particles off the proton beam axis. The big veto wall is consisting of 26 large scintillator sheets arranged in two layers covering a radius of approximately 2.5m around the beam pipe. A square hole  $60 \times 60\text{ cm}^2$  left in the centre is covered down to a 26cm circle by a small veto wall placed a further 1.5 m upstream [48].

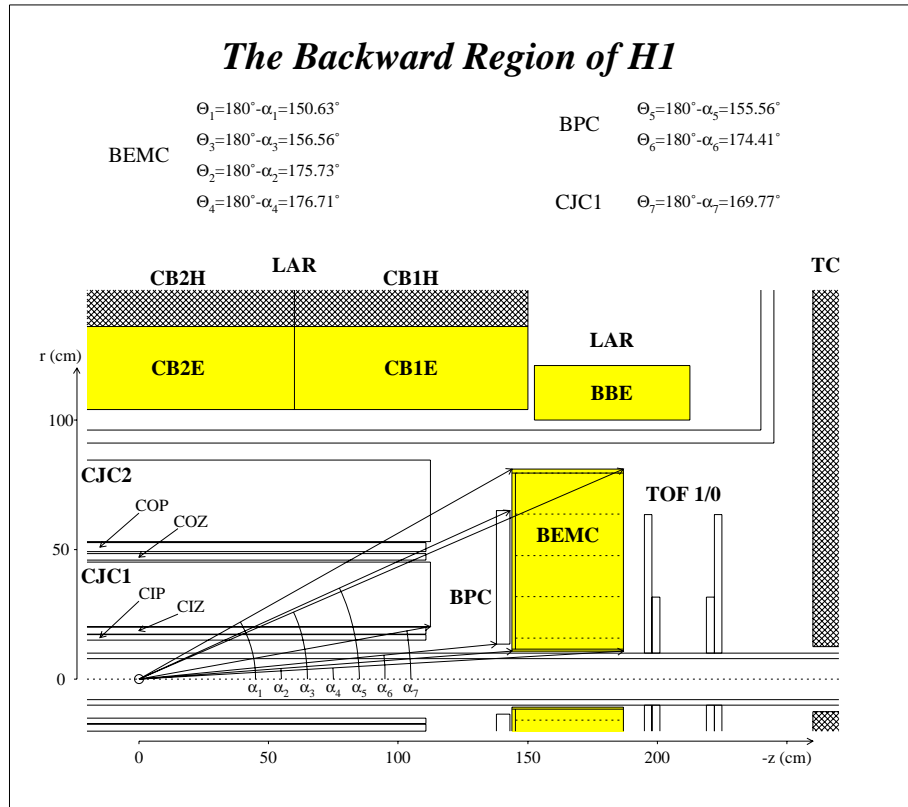


Figure 2.3: The details of the H1 backward region with all detectors in the proper scale.

## Chapter 3

# H1 Trigger

### 3.1 Triggering at HERA

Electrons and protons at HERA are circulating in up to 220 bunches with a beam crossing rate of 10.4 MHz, giving a clock period of 96 ns. Thus every 96 ns interactions can occur. At the design luminosity of  $1.5 \cdot 10^{31} \text{ cm}^{-2} \text{ s}^{-1}$  the dominant physics process will be photoproduction at a rate of  $O(100)$  Hz. Other physics processes will contribute by a small fraction of this highest rate only. From this point of view the triggering at HERA appears as a rather trivial problem. But, as the physics cross sections are small, maximum beam currents are required. The off-momentum protons, which number is correlated with the beam current, initiate huge background rate of the order of  $100 \text{ kHz}$  in the interaction region (for more details on the background rate estimation see page 41).

In fact two, at first sight contradictory tasks are required from the trigger and the data acquisition system:

- **high decision speed of the trigger** in order to minimize the dead time and to reduce the event rate down to a manageable level.
- **long signal integration time of the data acquisition system** in order to achieve the required energy and time measurement precision.

Next we discuss the solution developed within the H1-collaboration.

### 3.2 Frontend pipelines

The whole detector complexity, the geometrical size and differences in the basic physics detection principles of the different subdetectors are the reasons why the trigger decision cannot be made during the interval between two bunch crossings. The simple solution to buffer the frontend information and ignore the following bunch crossings until the decision to keep the event is made is not possible. This would mean introduction of the dead time on the first trigger level (L1) and would lead to unacceptable losses of the luminosity provided by the HERA machine. The goal is to build deadtime free L1 trigger.

Therefore, the detector response for each beam crossing has to be kept in a memory until the decision is available.

To achieve this goal, the so-called frontend pipelines for the detector and trigger data flow are used. The use of a pipeline allows to postpone the trigger decision and more time is available for the detector signals processing. By analogy, one can compare a pipeline to a cable delay. Thus for each channel the time structure of the detector response can be obtained. Analog delay lines are used e.g. to store the pulseheight of the BEMC. Digital

data for each beam crossing are stored sequentially and these data can be accessed at any time up to the pipeline depth (length).

The ideal pipeline length should be bigger than the longest trigger decision time, but small enough on the other hand so that it empties fast after restart. At H1 it has a length of  $2.2 \mu s$ .

### 3.3 Multi level trigger

The trigger converts the analog information into the **trigger elements (TE)**, i.e. yes/no decisions of the individual H1 trigger components encoded in bits. Examples are encoded energy thresholds for calorimeters ( $E > \text{threshold}$ ) or encoded hit patterns for multiwire proportional chambers. Each subdetector provides many trigger elements. These trigger elements are by logical functions combined into the so-called **subtriggers** and a logical *OR* from all subtriggers gives the final Level 1 **trigger decision**.

A decisive trigger parameter is speed rather than precision. It is impossible to get the final trigger decision in  $2.2 \mu s$  with a rate acceptable for the data logging on the storage media (5 Hz). Therefore together with pipelining a multi-level trigger and buffering scheme is used. For H1 the final trigger decision is supposed to be done in 4 different steps, called levels. The higher the level, the more complex and the more time-consuming is the process. The task of each level is to reduce significantly the rate of event candidates and to allow more time for a more sophisticated decision at the subsequent level.

In the first data taking period, in the year 1992, only two trigger levels were used: level 1 (L1) and level 4 (L4). Operation with only two levels was possible due to the fact that HERA machine was operated at  $\sim 1\%$  of the design luminosity.

In 1992 the measured proton induced background rate was only few hundred  $Hz$ . An L1 output rate of  $\sim 25 Hz$  safely matched the L4 input limit rate of  $50 Hz$ .

The final trigger decision at H1 will be done on the following trigger levels:

- **Level 1 (L1)** - An acceptable output trigger rate is 1 kHz for an expected total interaction rate of  $\sim 50 - 100 kHz$ , i.e. the required reduction factor is  $\sim 50 - 100$ . These numbers are valid for the full HERA and H1 trigger performance.

The dead time free first level trigger, due to  $2.2 \mu s$  decision time, must be based on the hardwired algorithms and combines only subsets of the full information available from all subdetectors. An important property is the big flexibility in combining different trigger elements from the same subdetector into complex coincidences.

The major parameters influencing the L1 trigger efficiencies are changeable by downloading them into the electronics. The trigger performance checking and identification of defective modules or inconsistencies in the trigger logic is done by on-line monitoring.

The L1 trigger is a rather complicated, distributed system with many additional signal delays. Precise synchronisation of all its elements is a vital task for the correct performance of L1.

One has to ensure that all individual trigger elements are providing their decisions in a well defined time, i.e. they have to be synchronized with the HERA clock. Of course

different trigger components have different decision speed. All fast trigger elements have to be delayed to wait for the slower ones. Correct timing adjustment is needed to synchronize all trigger elements. The beam crossing information provided by the subdetectors with very good time resolution, so called  $t_0$ , is treated as an independent trigger element and is needed for the proper calorimetric energy measurement, drift time measurement and for all other pipelined systems.

When analysing the L1 decision process three phases can be distinguished [43]:

1. Trigger elements from different subdetectors are produced, synchronised to the HERA clock and transferred to the central trigger logic (CTL) in groups of eight signals with accompanying clock to compensate automatically for individual cable delays and to maintain the synchronisation.
  2. The CTL synchronizes all 16 groups of trigger elements and forms up to 128 different subtriggers. The *OR* of all these subtriggers eventually leads to the L1 trigger decision.
  3. If the level 1 loaded trigger conditions are fulfilled  $2.2\ \mu\text{s}$  after the interaction time, an *L1-Keep* signal is produced which initiates a well defined sequence of fast hardware signals fanned out from the central trigger controller (CTC) to all subdetectors. The frontend pipeline stops and dead time starts accumulating. A L1-reject condition implies no signal and all pipelines remain active.
- **Level 2 (L2)** - hardware trigger with dead-time, starting with *L1-Keep*. The task of L2 is to reduce the input rate of 1 kHz to about 200 Hz. L2 decision is taken at fixed time  $\approx 20\ \mu\text{s}$ . The trigger elements for level 2 will be based on the same information as is used on the L1, but now more time is available to combine trigger bits from different detector parts. So called topological L2 trigger will require special hardware units utilizing characteristic topology of different physics event classes.
  - **Level 3 (L3)** - software trigger, starting in parallel with L2 further reduces the rate of triggered events to maximum 50 Hz. A dedicated  $\mu$ -processor will compute the L3 decision in  $800\ \mu\text{s}$  on the basis of the more complex matching of the information from different detector components.
  - **Level 4 (L4)** - software filter. The aim of this level is further reduction of the data volume before it is sent to the final storage media at the DESY computer center. The calculations are performed by the processor farm on the full event data, asynchronously with the rest of the trigger. Therefore this level is also called L4 filter farm. The filtering analysis is based on charged track, vertex and energy cluster information. The most important filtering criterion, effective against beam gas and beam wall backgrounds, is based on the  $(x, y, z)$  vertex reconstruction. Very important is also the recognition and rejection of the so-called 1-diode events triggered by BSET (see page 97). The aim is reduction of the final data logging rate to  $\sim 5\text{Hz}$ .

### 3.4 L1-Trigger elements from specific detectors

As already mentioned, the L1 subtriggers must be based on hardwired algorithms and only relatively crude information from the subdetectors can be utilised. Nevertheless L1

comprises many trigger elements from different parts of the H1 detector, such as energy sums from the calorimeter or veto-wall and TOF bits suppressing events initiated by the off-momentum beam particles. Particularly interesting L1-trigger elements are produced by the tracking chambers. XILINX logic cells are used for fast z-vertex position reconstruction from the proportional chambers and for the fast charged tracks finding in the  $r - \phi$ -projection of the central drift chamber.

Generally one can say that the main DIS physics triggers are based on the calorimeter trigger information and that the tracker trigger elements are used mainly as an effective tool to recognize the background events and reject them on the L4 level.

Subdetectors providing trigger bits for L1 are shown in Fig. 3.1.

### 3.4.1 Calorimetry

#### Liquid Argon Calorimeter

The primary task of the LAr calorimeter trigger is to select the high  $Q^2$  events, the study of these being one of the reasons for which HERA was built. The LAr trigger itself is divided into an analog and a digital part [52] and its overall decision time is  $2.1 \mu s$  [40].

The analog sum of 16 channels in the electromagnetic (EM) or of 4 in the hadronic (HAD) part forms the basic trigger unit - called *Trigger Cell* (TC). In total almost 40000 channels are read out.

Up to 4 electromagnetic and 6 hadronic TCs are summed up and shaped to form a *Trigger Tower* (TT). The TTs are approximately pointing to the interaction point and are segmented in 23  $\theta$ -bins and up to 32  $\phi$ -bins. In order to allow for a bunch crossing time  $t_0$  determination the capacities of the channels summed into the same TT must fit to  $\pm 5\%$  [40].

Depending on the  $\theta$ -region, either 1,2, or 4 TTs are summed up to form a *Big Tower* (BT). BTs are organized also according to the principles of projective geometry, they are pointing to the vertex. There are in total 252 BTs, 240 in the LAr calorimeter itself and additional 8 BTs in BEMC, resp. 4 BTs in plug calorimeter.

In the digital part the energies of the corresponding EM and HAD sections are digitized by 8-bit 10 MHz FADCs and summed up into BT-energies after relative weighting by lookup tables. Further summing of BTs, again according to the corresponding lookup tables, results in the different energy sums. Digital part provides following trigger elements sent to the central trigger logic:

- *electron trigger*
- *transverse energy*
- *total energy*
- *missing transverse energy*
- *topological energy sums*  
 Plug, Inner Forward (IF), Forward (IF+Plug),  
 Central Barrel (CB), Forward Barrel (FB), Barrel (FB+CB),  
 BEMC, Backward (CB+BEMC)

- *BTs*  $t_0$
- *Big Rays*  $t_0$  (BTs  $t_0$  matched to the MWPC big ray)

The division into 8 topological regions is hardwired and each of these regions is subdivided into 4  $\phi$ -quadrants. This gives altogether 40 topological trigger sums (with 8 total energies). The total and transverse energies are added separately. Each energy is discriminated by a 2-bit table, allowing definition of 3 thresholds.

The energies of the EM and HAD parts of the individual BTs are used to build an electron trigger. Energy in the EM part has to be above a given threshold, whereas energy in the HAD must be below some threshold.

### BEMC and Plug

The BEMC and plug trigger are an integral part of the L1 overall calorimeter trigger. BEMC is divided into 24 TTs and 8 BTs (Fig. 2.2) and plug is subdivided into 16 TTs and 4 BTs.

### BSET

A special BEMC single electron trigger (BSET) with smaller granularity was designed and realised in order to cope with the expected high rates in the backward part of H1 (for details see page 72).

## 3.4.2 Tracking System

### MWPC Triggers

Trigger signals from the MWPC are derived from the two double layers of CIP and COP in the central region at average radii of 16 *cm* and 52 *cm*, and three double layers of MWPC (modules) in the forward region centered at  $z = 146, 188, 231$  *cm* [60]. The combinations of the hits in various chambers define trajectories (rays) with a precision given by the cathode pad size and the spacing between the chambers.

These rays are then used to provide two types of trigger information :

- *z-vertex trigger* - A hardwired logic finds so-called *rays* from  $z$ -coordinates of all possible hit combinations in the CIP and COP pair or in the CIP and the first forward MWPC pair. The  $z$ -coordinate of the origin of each ray enters the 16 bin histogram (5 *cm*/bin). Inevitably also combinations not originating from true particle tracks are entered, however these 'wrong' rays generally produce a flat  $z$ -distribution. If there is at least one entry into the histogram the  $ZVTX - t_0$  trigger element is produced. So the  $ZVTX - t_0$  is a rather weak condition indicating some activity in the H1 interaction region. A significant peak in the  $z$ -vertex histogram is considered as a strong signal for an event originating in the interaction region. Two different significance thresholds are used and the corresponding trigger elements are called  $ZVTX - sig1$  and  $ZVTX - sig2$ . The final histogram building and the peak analysis is done by the programmable logic cell arrays (XILINX).

- *forward ray trigger* - The forward ray trigger identifies trajectories (roads) of charged particles coming from the interaction region ( $\pm 25\text{ cm}$ ). A road is a set of impacts on 3 or 4 MWPC modules in one  $2\pi/16\ \phi$  sector. Among the 6 or 8 chambers (2 chambers per module) only one is allowed to miss the track, which was detected by the others. An estimation of tracks multiplicity for each sector is also made. Topological pattern code gives some information on the event topology in  $2\pi/8\ \phi$  granularity. The 256 different patterns are grouped into 30 different classes. Patterns in each class can be derived from each other from symmetry principles. Patterns are fully programmable and e.g. two back to back roads with low multiplicity per  $\phi$  sector can be required.
- *big rays* - a big ray corresponds to at least one ray found by the ZVTX or forward ray trigger and pointing to a calorimeter big tower.
- *BPC trigger* - if at least three out of four planes of the backward MWPC (BPC) have seen a hit, the BPC trigger element is produced.
- *CIP trigger* - if more than three sectors in the backward quarter of the CIP are active, the CIP-backward trigger element is produced. This element is used mainly as a veto for some subtriggers which are using tracking information only.

### Drift chamber trigger

The information from the central jet chambers is used to find and count charged tracks [61]. The track finding logic works fully parallel in the  $r - \phi$  projection of the whole chamber on the subset of 870 out of the total 2160 sense wires of the CJC1 and CJC2. The signals above the threshold from selected wires are fed into shift registers. The outputs of shift registers are compared with a large number of predefined patterns corresponding to different  $\phi$  angles and different  $p_{\perp}$  cuts and charge. In the trigger only 10 out of 56 layers of sensitive wires are used. These ten layers of wires are divided into two groups. Only hits in four out of five layers within one group are required to form a valid pattern, so called trigger road.

Restricting the  $R - \phi$  origin of the tracks to be very close to the beam axis (distance of closest approach - DCA) is an effective tool to reduce the background and noise events rates [61].

The  $DC - r\phi$  trigger logic provides the number of track candidates for positive and negative curvatures above two programmable transverse momentum thresholds and topological correlations between tracks can be programmed as well. E.g. trigger elements  $DC - r\phi - thr0$  and  $DC - r\phi - thr1$  are used for finding at least 1 resp. more than 1 track candidates in the interaction region.

### 3.4.3 Luminosity system

Three basic trigger elements are used in the central trigger logic:

- ET (electron tagger) total energy
- PD (photon detector) total energy
- VC (veto counter) signal

For luminosity measurements a stand alone system, independent from the central trigger and DAQ is needed. For this purpose the bremsstrahlung process  $e^-p \rightarrow e^- \gamma p$  is used. Simultaneous measurement of  $\gamma$  and scattered electron requires coincidence between energies deposited in ET and PD. Cerenkov counter in front of PD can be used as a veto (VC) for events in which bremsstrahlung photons interacted in the Pb filter.

The total photoproduction cross section measurement is the second very important task of the luminosity system. A typical and clean signature for the photoproduction process ( $\gamma p$ ), i.e. the interaction of quasi-real photons  $Q^2 \rightarrow 0 \text{ GeV}^2$  with protons, is the following: no activity in the PD and an energy deposit in the ET above some threshold. But the huge background from the above mentioned bremsstrahlung process (24.3 mb of accepted cross section compared to  $\sim 1.4 \mu\text{b}$  for  $\gamma p$  [62]) and from the beam-gas background interactions makes this method only marginal and does not provide a reliable measurement of  $\sigma_{\gamma p}^{\text{tot}}$  [62].

In order to measure the  $\sigma_{\gamma p}^{\text{tot}}$  one has to rely on an alternative method: tagging of the scattered electron in coincidence with the trigger elements of the main H1 detector. For triggering on secondaries created at the  $\gamma p$  vertex the tracker triggers are most effective. The electron tagger as a subtrigger requires a coincidence of the total energy of ET with a veto from the PD ( $ET * \overline{PD} * \overline{VC}$ ).

### 3.4.4 Muon system

Inclusion of efficient muon triggers covering a large solid angle, substantially increases the physics potential of H1 [48]. Muon triggering and measurement is for many processes complementary to electron triggering and allows a comparison between channels involving intrinsically the same physics, but with different systematic effects. Only to name a few of the physics processes, which need a good muon trigger one can mention:

- heavy-flavour physics; accessible through the  $\sim 10\%$  semi-leptonic decay fractions of charm and beauty states
- $J/\psi$  photoproduction; accessible through the decay into  $\mu^+ \mu^-$
- exotic phenomena; search for excited leptons or supersymmetric particles

A second important asset is the possibility of cross-calibration of the other parts of the H1 detector. This can be done by cosmic or beam-halo muons, and muons from the physics channels.

**Central muon trigger** The first level muon trigger is based on the digital readout of the tail catcher calorimeter layers (*muon chambers*) [46]. Each wire from the LST system is digitized and the number of output signals is reduced by factor 16 via applying a logical *OR* on groups of 16 wires. These fast trigger outputs of five, from the total 12, LST chamber layers (3,4,5,8,12) are sent to the central trigger logic.

The configuration of the trigger electronics is programmable and provides a very flexible solution to meet many different requirements. The whole LST detector is divided into 4 *sectors* (forward and backward endcap, forward and backward barrel), within each of these sectors chambers are grouped into 16 different modules. Signals from the five trigger planes are treated separately for each module in a so called *layer coincidence*. Trigger

signals within the planes are OR'd and outputs from 5 planes are in the corresponding RAM combined according to the required logic. Each RAM provides 8 bits for further usage and in total  $64 \times 8$  signals can be combined.

### Forward muon trigger

Muon track candidates are selected only if they have hits in both modules in front of or in both modules behind the toroid (pre- resp. post-toroid muons). For triggering purposes only the  $\theta$ -chambers are used, the usefulness of  $\phi$ -chambers being limited by multiple scattering. The requirement on the pointing of the track to the z-vertex efficiently reduces rate of background events [48].

### 3.4.5 Scintillators

Scintillator triggers are designed mainly to veto background events. Their very good time resolution of  $\sim 1$  ns enables them to provide very important time information for the H1 trigger system and allows precise synchronisation of the triggers with respect to the beam interactions.

### Veto Walls

Experience of UA1 shows that high momentum muons originating a long way upstream of the detector, so called *beam-halo*, could be misinterpreted as high  $Q^2$  interactions and this kind of background is best vetoed by this type of detector [48]. Nevertheless, the potential of this trigger element was not fully used in the year 1992.

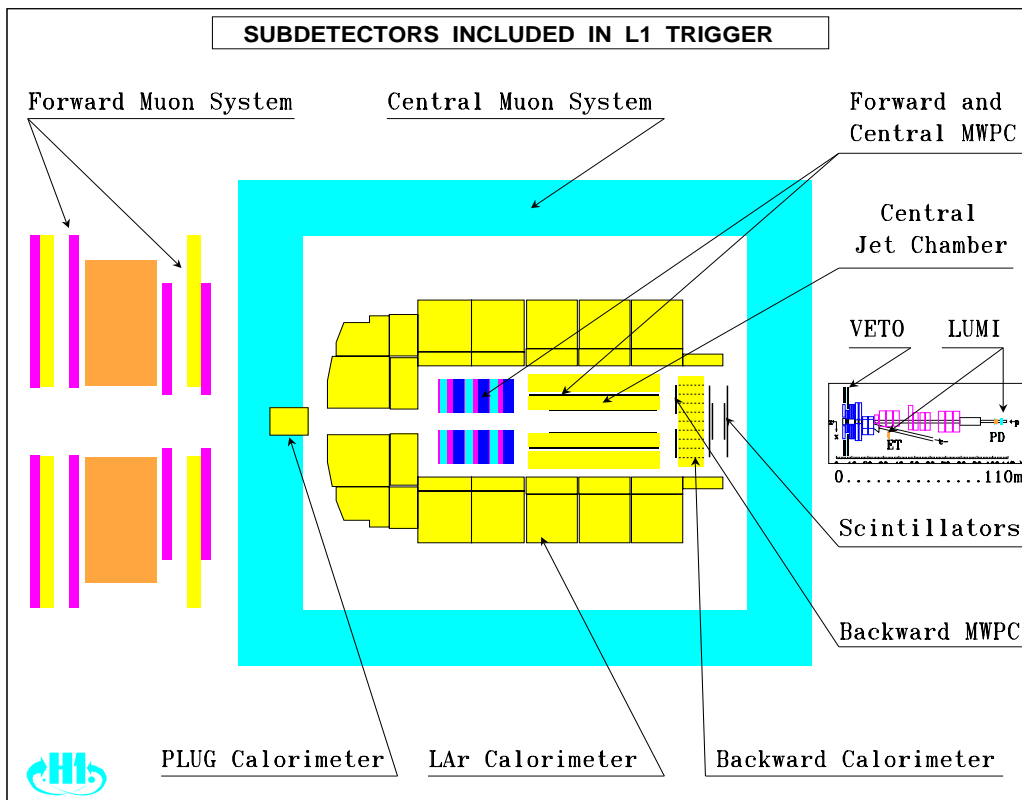
### TOF

The veto function of the TOF is based on the time of flight difference of  $\sim 14$  ns between the arrival of particles originating upstream and inside the interaction region.

Most of the secondary particles from the background interactions will be absorbed by the different beam line and shielding elements, but the particles concentrated in a narrow cone around the beam axis will enter the H1 detector or hit the synchrotron radiation absorber mask at around  $z = -3$  m. Monte Carlo simulations showed that there is substantial yield of secondary particles of high energies, which cause big energy depositions in calorimeters and a lot of tracks in the central region [48]. A large fraction of these out of time events is vetoed by the TOF, therefore most physics L1-triggers require a veto from this detector.

Signals from particles originating in the interaction region (*interaction (IA) window* or *positive TOF*) are used as well, mainly for triggering of the so called high-y events. TOF triggers in the IA-window exploit the information from the leakage of high energy electromagnetic showers and/or from the punch-through hadrons accompanying low energy electrons.

In addition, the TOF wall also covers a small beam-halo window left in the veto wall because of the physical constraints of beam-line elements.

Figure 3.1: *H1 detectors in L1 trigger*

## Chapter 4

# Trigger for NC DIS

## 4.1 General requirements

Triggers are needed in order to reduce the rate of potentially interesting events to a level manageable by the data acquisition system. In the presence of a large number of different event topologies and similarities even with background events it is usually impossible to come to a required unique solution in a very short available time. At this point one has to be very cautious, because the price for the higher selectivity (lower rates) could be uncontrollable losses of certain events class leading to a bias in the trigger. A reasonable compromise between selectivity and controlled losses must be chosen.

A trigger is not necessarily associated directly with a particular physics process. Triggers are usually designed to identify and measure the physics objects or quantities which characterize the physics signal. So called *physics triggers* as electron, muon, jet or missing transverse energy  $E_T$  (neutrino) triggers have been designed. Basic requirements for the trigger system aimed for any physics class are the following:

- **high efficiency** - preferably  $\geq 50\%$  , computable and known to adequate precision
- **minimum bias** - the resulting trigger efficiency should not depend on the physical model
- **background rejection power (selectivity)** - fraction of triggered background events should be minimal
- **simplicity** - the trigger must be as simple as possible, in order to be well controllable and understandable
- **reliability (robustness)** - stable and reliable performance, not very sensitive to the detector performance (noise) and different background conditions (e.g. beam quality)
- **redundancy** - it is desirable to have at least two independent triggers covering the same kinematical region to cross-check their efficiency, to calculate the acceptance
- **overlapping triggers** - smooth covering of the whole kinematical region, overlapping on the boundaries to avoid discontinuities in the efficiency

## 4.2 NC DIS Triggers

When looking for the efficient trigger for NC DIS, it is clear that the main trigger must be an  $e^-$ -trigger, based on the calorimeter information. Deposition of substantial, well

localized energy in the calorimeter is the most powerful electron selector. Calorimeter triggers relying on the electromagnetic showers energy measurement have a high efficiency, they are robust, relatively simple, controllable and independent of a model assumptions.

Tracker detectors are used to trigger on the hadronic final states of the DIS. Since the processes of initial and final state QCD radiation, fragmentation and hadronization processes at HERA energies are only extrapolated from scattering at lower energies, they are not well known and there exist a lot of different models trying to predict the event topology. Therefore trigger algorithms prepared on the basis of MC simulation are model dependent and can introduce bias. Tracker triggers will be used mainly for cross-checking the calorimeter trigger performance and as a main triggers only in the regions not accessible to calorimeter triggers. They are very effective on the L4 level, filtering out the beam-wall and beam-gas background events.

Triggers combining calorimeters and tracking detectors are used to cover some regions inaccessible by calorimeter triggers alone.

Thus we divide our triggers into three classes:

- *calorimeter triggers*
- *tracker triggers*
- *combined triggers*

When studying the kinematics of the NC DIS (Fig. 1.2). and taking into account that our main triggers should be calorimeters, we come to the natural division of the NC DIS events into two classes:

1. **low  $Q^2$  events** -  $Q^2 \leq 100 GeV^2$ , scattered electron is in the BEMC
2. **high  $Q^2$  events** -  $Q^2 \geq 100 GeV^2$ , scattered electron is in the liquid argon calorimeter

Of course, there is no sharp boundary line at  $Q^2 = 100 GeV^2$ . The existing overlap in the geometrical acceptance between the BBE part of the LAr and the BEMC and the smearing of the  $z$ -vertex position are the reasons for the kinematical overlap in  $Q^2$  between 80 and 150  $GeV^2$ .

In our further studies we will concentrate mainly on the low  $Q^2$  physics with the aim to find efficient trigger algorithm covering this very promising kinematical region, which is going to be the so called *first days physics*.

## 4.3 Background to the NC DIS Events

### 4.3.1 Physics Background

The main physics background for the NC DIS at low  $Q^2$  is coming from the photoproduction process. These events have usually low energy activity in the H1 detector and in addition resolved photon interactions tend to produce hadrons in the backward region. The potential of the L1 trigger to separate photoproduction from NC DIS process is in this region very limited. For a large fraction of these events the electron is detected in the

electron tagger. But still high rates of non tagged  $\gamma p$  events produce signals in the BEMC. Hadrons and photons could mimic a NC DIS electron. Especially the region of low cluster energies ( $< 10 \text{ GeV}$ ) close to the beam pipe is expected to be strongly contaminated by these events.

### 4.3.2 Machine Background

The biggest source of background at HERA comes from the electron synchrotron radiation. This radiation is predominantly soft and close to the beam axis thus should cause no trigger problems [48]. The main problem for the first level (L1) trigger at HERA is the rate of background events originating from the proton beam. An example of a typical HERA background event is shown in the Fig. 4.1. According to the production mechanism we distinguish two dominant sources induced by the proton beam [3]:

- **Beam-gas** interactions of primary protons with the residual gas in the beam pipe
- **Beam-wall** interactions of the off-momentum protons from the beam with the beam pipe wall producing high energy hadronic showers

Due to the fact that these are both strong processes and the  $e^-p$  collision is an electroweak process, the background rates are much higher than the physics ones.

#### Rates prediction

The rates for the machine background events are difficult to estimate reliably, they are much more uncertain than the physics rates. Nevertheless the following estimates were made.

- **Beam-gas** interaction rate strongly depends on the assumptions about the beam pipe vacuum quality, i.e. about the residual gas density and about the composition of this gas. For the HERA vacuum the values ranging from  $1 \times 10^{-9}$  to  $3 \times 10^{-9} \text{ Torr}$  were used.

Concerning the rest gas composition, e.g. the PETRA as well as the SIN vacuum group claim that the rest gas is mostly  $H_2O$ . At HERA the rest gas composition [49] is expected to be from 50%  $H_2$  and a heavier components  $\sim 50\%$  ( $H, C, O$ ) or air might be present in the warm HERA sections. Second important factor influencing the final rate estimate is the number of protons in the ring or the proton beam current. Here the designed value of  $2 \times 10^{13}$  protons in the ring is used (this corresponds to  $\sim 160 \text{ mA}$ ).

Another factor increasing the beam-gas events rates is the length of the collider straight section before the interaction point. HERA experimental areas are sensitive from  $\sim 100 \text{ m}$  upstream the proton beam.

The total rate of the beam-gas interactions  $W$  can be calculated from the following equation [50]:

$$W = n_p \cdot \nu_p \cdot \sigma \cdot A^{0.7} \cdot n_{gas}$$

where:

- $n_p$  - proton beam density ( $2 \cdot 10^{13}/6.3 \cdot 10^5 [cm^{-1}]$ )
- $\nu_p$  - protons relative velocity ( $3 \cdot 10^{10} [cm \cdot sec^{-1}]$ )
- $\sigma \cdot A^{0.7}$  - p-gas cross section ( $35 \cdot 10^{-27} \cdot A^{0.7} [cm^2]$ )
- $A$  - gas atomic weight
- $n_{gas}$  - number of gas atoms at  $10^{-9} torr (7.2 \cdot 10^{13}/A)$

From these assumptions the obtained rate of the beam-gas events is  $\sim 3kHz/m$  and rate of events producing at least one  $t_0$  in any of H1 subtriggers is predicted to be  $\sim 35 kHz$  [79].

- **Beam-wall** interaction rate is determined by the lifetime of the proton beam and of course by the number of protons in the ring. Proton beam losses occur along the whole HERA ring but the main losses are expected at collimators in the straight section West of the HERA ring. They absorb most of the off-momentum protons. However a small fraction of these protons survive ( $\sim 1\%$ ) [3] and impact at the QS quadrupole magnet ( $z \simeq -40 m$ ). Decisive for the rates observed in the H1 detector are therefore the proton beam losses at this QS quadrupole magnet. Assuming a proton beam lifetime of 20 hours, an average proton loss rate  $5.0 \cdot 10^5 s^{-1}$  at this critical place is expected. So the final beam-wall interaction rate in the experimental areas is expected to be  $\sim 70 kHz$  [79]. It is only by factor  $\sim 2$  higher, when compared to the beam-gas events (BGE), but additionally the beam-wall events (BWE) energy spectrum is harder, more aggressive than the beam-gas background.

### Rates first measurements

Experimentally it is not easy to identify unambiguously and separate beam-wall and beam-gas background events. Therefore only the total measured rate is given. From the first comparisons, with the proper scaling to the delivered beam currents, it seems that the predictions were a little bit too pessimistic. The observed rate, which is strongly correlated with the beam conditions and can change from run to run, was by factor  $\sim 2.5 - 5$  smaller as expected [79]. Nevertheless, taking into account all uncertainties connected with the estimation of these quantities, this result can be considered as a good agreement. Simulations of the BWE and BGE (see page 45) based on the above mentioned assumptions proved to be very useful and inevitable tool in the process of preparation of suitable trigger algorithms for specific physics processes.

Synchrotron radiation as a source of high background rates was originally considered as unimportant. But first data analysis indicate that direct hits of BEMC photodiodes creates a lot of fake cluster triggers. For more details see page 99.

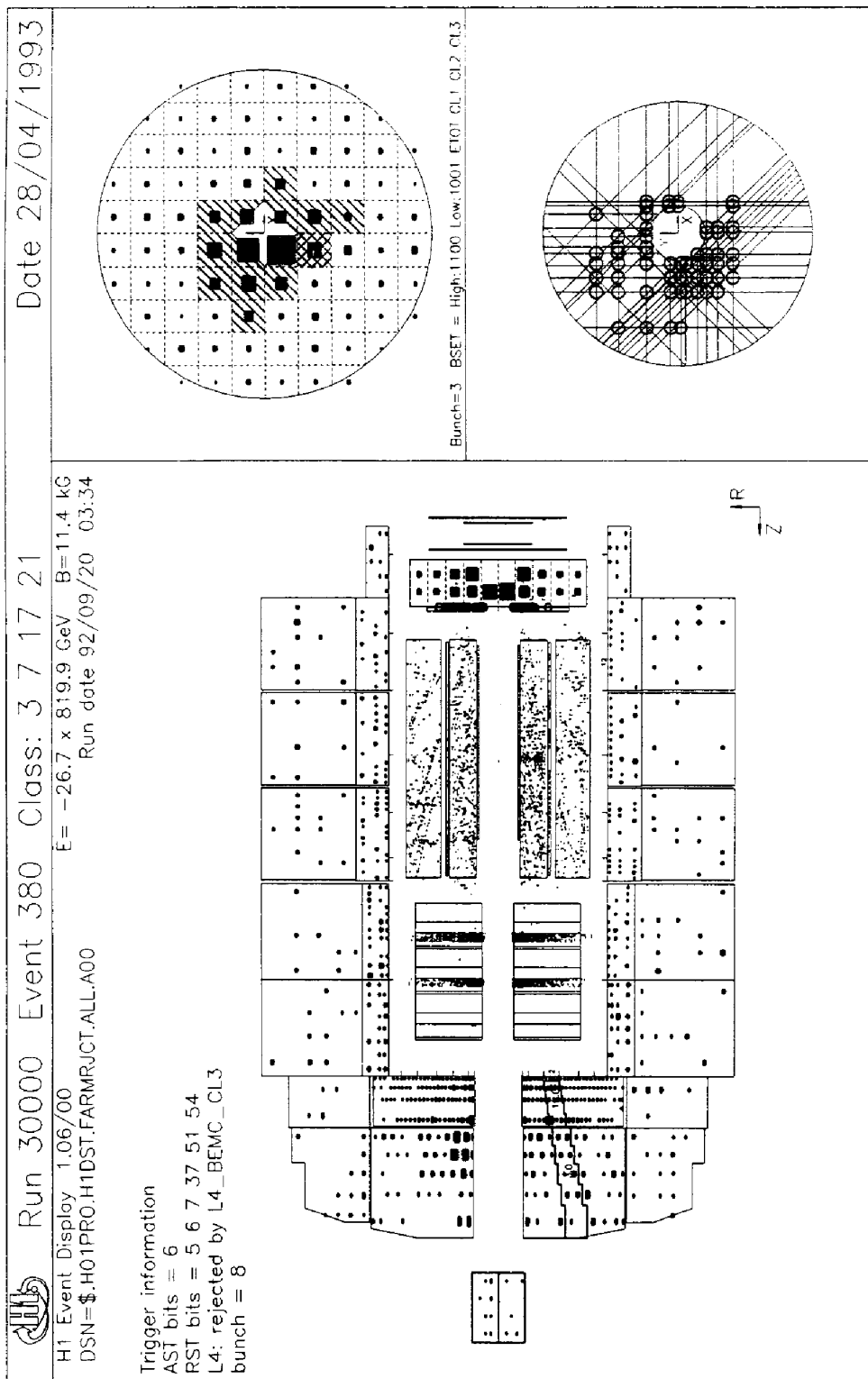


Figure 4.1: Typical HERA background event in the H1 detector with large energy deposit in the BEMC stacks concentrated around the beam pipe and many BPC hits.

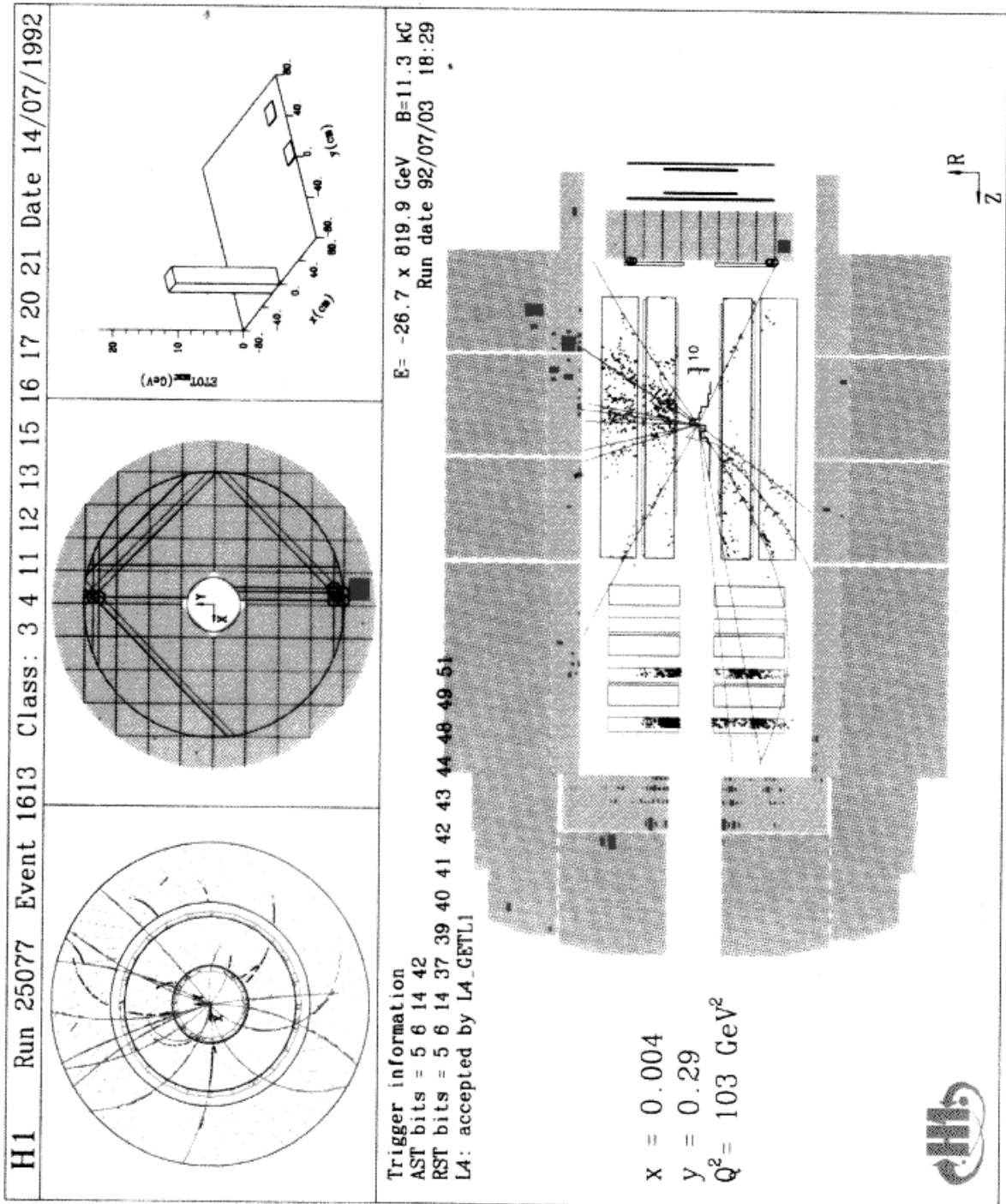


Figure 4.2: NC DIS event in the H1 detector with electron in the BEMC triggered by the BSET trigger.  $R - \phi$  projection of the tracks in the central jet chamber, and a typical back-to-back kinematics of the scattered electron is to see in the BEMC with hits in the BPC.

---

## Chapter 5

# Trigger Simulations

The inevitable prerequisite for designing any detector or trigger hardware in the high energy physics complicated experiments is the Monte Carlo (MC) simulation.

Trigger studies should answer these basic questions:

1. what are the signatures of the physics process we want to trigger on?
2. what kind of background processes could compete with the physics and what are the signatures of these processes ?
3. what is the considered detector response to the particles entering this detector ?
4. which trigger elements or what trigger logic could be built using the information provided by the detector ?
5. how the different trigger elements from different detectors could be combined and used for the given physics process?
6. what is the trigger efficiency of the different trigger schemes for specific physics classes, what are the corresponding background rates ?

First ideas and hints to answer the above mentioned questions can be obtained from the studies on the 4-vector output from the MC generators. MC generators are used mainly for the first task and partially for the second one, when considering background from other physics processes.

It is however insufficient to simulate complex detector systems and evaluate reliable trigger algorithms within this approach. Simple smearing of 4-vectors is insufficient to reach the required level of precision and sophistication.

The differences in terms of CPU time requirements between the MC event generator and the full detailed detector simulation program are enormous. Therefore various methods are developed to speed up the simulation. Usually 2–3 different simulation packages, with different level of sophistication, with different precision and proportionally different CPU time requirements are used. The usage of the certain version is determined by the precision required.

For detector studies a very detailed geometry description and sophisticated tracking of the individual particles is needed. From these kind of studies the absolute response and the resolution of the detector is obtainable. Typical CPU time consumption is of the order of  $1s/GeV$  and scales lineary with the particle energy [73].

This approach is not usable for the event simulation for physics analysis (e.g. acceptance calculation, trigger efficiency). The CPU time reduction can be achieved by simplifying the detector geometry description, averaging the detector media properties, and parametrizing the shower developments in the calorimeters or by applying higher cut-offs for particle tracking. All these measures should not deteriorate the precision of the final results, simulation still has to retain the accuracy needed for the studied task.

For the feasibility studies requiring only very limited precision, a strongly simplified detector geometry, parametrization of the showers development and high tracking cut-offs are satisfactory. Within this attitude the speed of  $0.1s/100 GeV$  showers with a logarithmic dependence of the CPU time on the energy was achieved [73].

In the H1 collaboration the following detector simulation programs, with different levels of simplification are used (see Appendix A):

- H1PSI - very coarse detector description, shower parametrization
- H1FAST - averaged calorimeter medium, parametrized shower development, but still detailed simulations in cracks
- H1SIM - detailed detector description, detailed simulation

When comparing CPU time consumption, H1SIM needs e.g.  $1000\times$  more time than the simple MC event generation and H1FAST is  $\sim 10\times$  faster than H1SIM [73]. The event processing time of the H1PSI is about 0.06 sec on the IBM 9000/720 and this is gain factor of  $\sim 500$  when compared to the H1FAST time consumption.

## 5.1 BSET Trigger Design Simulations

The design studies of the electron trigger for the BEMC were limited by the fact that the detector itself was already designed and being completed at DESY. The basic question was how could we use the existing structure to build an efficient electron trigger. Originally the BEMC was proposed to be only as a part of the LAr calorimeter trigger, which in fact did not use the whole potential of this device. The largest deficiency of this proposal was the too coarse granularity of the trigger. The BEMC was divided into eight big towers (1 big tower is defined as a sum from 4 resp. 18 stacks, see Fig. 2.2) and as a final trigger element was considered only the total sum from all BEMC big towers - the total BEMC energy. In the background conditions at HERA, especially in the H1 backward area, this would lead to a high trigger threshold ( $E_{tot} \sim 15 - 20 GeV$ ) and thus very limited access to the most interesting NC DIS physics in the kinematical region of *low x, high y*.

Therefore additional design studies with the aim to use the smallest available energy sum - the *stack energy* - were done in the following three steps:

1. The size of the electromagnetic (EM) and hadronic showers in terms of the number of hit stacks and the energy sharing between the adjacent stacks was studied. The longitudinal segmentation of the BEMC stacks was also investigated with the aim to use the so called hadronic part of the stack for electron identification. From these studies we have defined *clusters*, their size and energy thresholds for given electron energies.

2. In the second step we have tried to understand the event topology and characteristics of the physics processes we want to trigger on and also the features of the possible background sources.
3. In the last step we have defined and tuned trigger algorithms and thresholds in order to achieve reasonable trigger efficiencies and simultaneously acceptable rates from all background sources.

### 5.1.1 Electromagnetic Showers in the BEMC

#### Radial size of EM showers

This size was studied in the terms of the proposed basic BEMC trigger element - stack energy. We have considered the following questions:

- energy sharing between the hit stacks, energy deposition in the leading stack
- number of hit stacks as a function of the stack thresholds
- energy dependence of the first two parameters
- effect of the expected noise contribution

From the EM cluster size and from the simple geometrical considerations one could expect always at least 1 stack with at least 25% of the total cluster energy. The actual fraction of events with this kind of energy sharing is very small and in most events the leading stack contains  $> 50\%$  of the cluster energy (Fig. 5.1d). The reason for this is in the interplay of the BEMC non-projectivity in the  $\theta - \phi$  plane and the lateral size of electromagnetic showers. From Figs. 5.1b,c we can see the regions hit by 30 GeV electrons in which the leading stack has less than 40% and 50% of the total deposited energy respectively. A clear angular dependence can be seen. At bigger radii the regions with the considered energy sharing are moving from the cracks more to the centers of the hit stacks. These regions are the same as those where the energy losses in the cracks between stacks are important and where the largest energy corrections have to be applied to the measured energy [77].

From the energy sharing between the stacks and from the fraction of energy deposited in the leading stack, i.e. in the stack with maximal energy deposit, we have defined **stack high thresholds (HT)** as a seed for the trigger cluster. Fractions of the total cluster energy detected in the leading stack are very similar for the whole electron energy spectrum. An example for 30 GeV electrons is shown in Fig. 5.1(d). The general rule outcoming from these studies is that stack HT should be set to  $\sim 30 - 40\%$  of the electron energy we want to trigger on (Fig. 5.2). It means e.g. that with the stack  $HT = 3 GeV$  we will safely trigger on  $E_e > 10 GeV$ . We will trigger also on most of the electrons  $E_e > 5 GeV$ , but here some fraction of events could be lost already due to the HT value. This should be kept in mind when setting the trigger thresholds.

In principle we could trigger on the simple requirement of the stack energy above HT. But this simple condition is not acceptable due to the high background rate. We need higher thresholds but still to be able to trigger on low energy electrons. This dilemma can be solved by summing up energy depositions also from stacks surrounding the leading

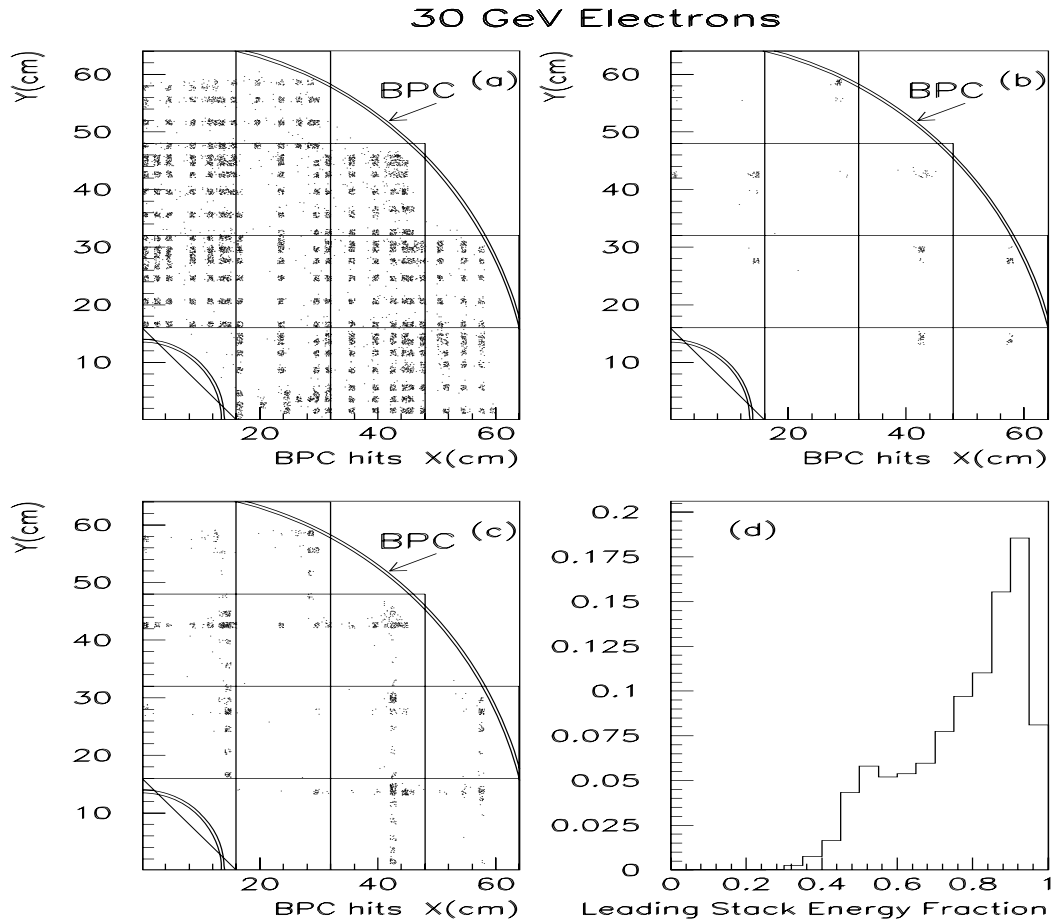


Figure 5.1: Simulation of 30 GeV electrons hitting BPC and BEMC under realistic angles for part of the detectors quadrant. Shown are BPC hits coordinates and the BEMC stacks: (a) all events; (b), (c) only events in which energy in the leading stack was  $< 40\%$ , resp.  $< 50\%$  of the cluster energy; (d) Cluster energy fraction in the leading stack for all simulated events.

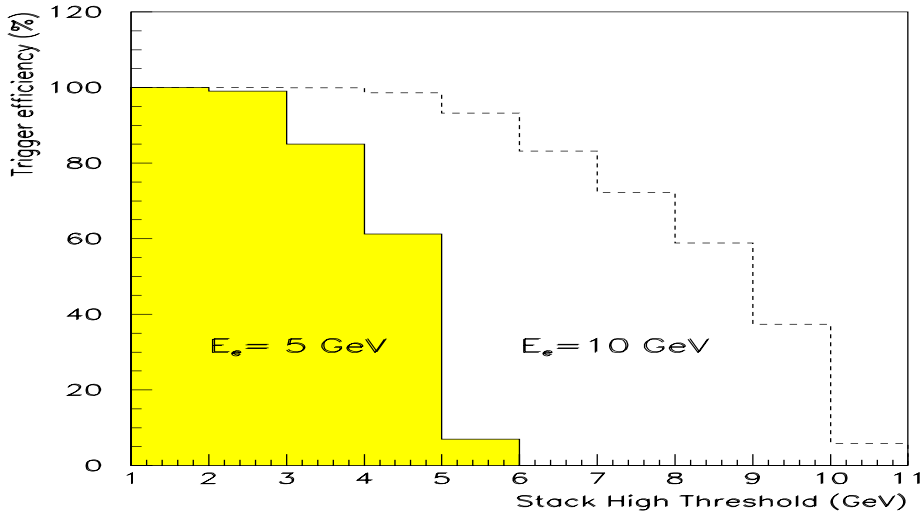


Figure 5.2: The effect of the stack high threshold values ( $HT$ ) on the trigger efficiency for 5 and 10 GeV electrons. No low thresholds and no cluster thresholds are applied. At least 80% of the incident energy is required to be deposited in the detector.

stack. For this purpose we have defined the so-called **low thresholds**  $LT$ .  $LT$ s enable contribution to the BEMC **total trigger energy** ( $BTOT$ ) and to the **trigger cluster energy** ( $TCLUS$ ).  $TCLUS$  is built only in the case that there exists at least 1 stack above  $HT$ , i.e.  $HT$  works as a  $TCLUS$  initiator. Neighbouring stacks above  $LT$  are contributing to the trigger cluster energy sum. In order to have a good correlation between the trigger cluster and the real cluster, the  $LT$  should be as low as possible. The lower the  $LT$ , the better the correlation between real cluster and the trigger cluster. These  $LT$ s are set to 3-4  $\sigma$  above the noise level (called also noise thresholds).

Distributions of the number of hit stacks at four stack thresholds 0.4, 0.7, 1.1, and 2.0  $GeV$  for electron beam energy 30  $GeV$  are shown on the Fig. 5.3. From this detailed MC simulation with H1SIM we see that down to the stack threshold of  $\sim 1.0$   $GeV$  the maximal number of stacks found above this threshold is 4. This is valid for all electron energies up to the maximal electron beam energy 30  $GeV$  which is designed for HERA. This result provides us the **trigger cluster** definition as a **group of  $2 \times 2$  adjacent stacks** above the defined threshold. Only below  $\sim 1.0$   $GeV$  there is some small probability to have more than 4 stacks in the cluster and in this case the proper trigger cluster definition would be  $3 \times 3$  stacks.

### Longitudinal size of EM showers

The longitudinal shape of the electromagnetic showers can be measured from two samplings: from energy deposit along the whole stack and from the energy detected in the last third of the stack ("hadronic" section). The fraction of the total cluster energy leaking into this hadronic part ( $R = E_{back}/E_{clus}$ ) was considered as a potential trigger element,

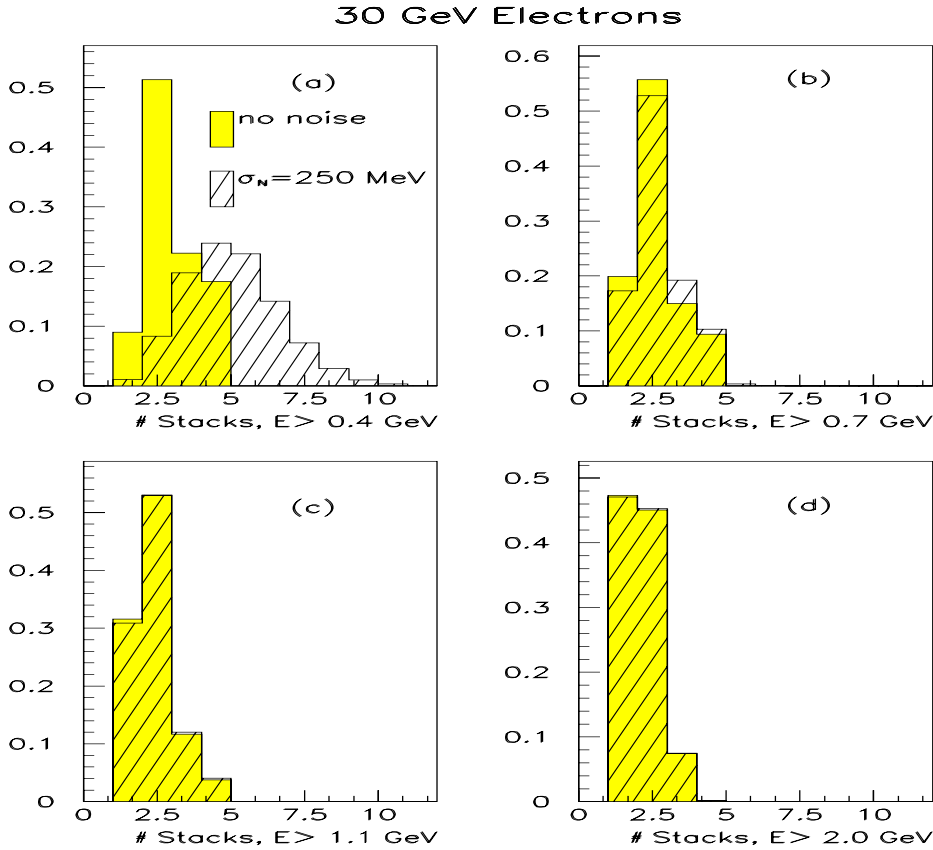


Figure 5.3: Simulation of 30 GeV electrons hitting BPC and BEMC under realistic angles without and with expected noise contribution  $\sigma = 250$  MeV per stack. Shown are number of hit stacks with energies above defined stack thresholds. The content of the histograms is normalized to 1.

which could work as a veto against the HERA machine induced background and simultaneously as a tool distinguishing electrons from hadrons originating in the interaction region. Electromagnetic showers in the BEMC are rather short and in  $> 99\%$  of cases the leakage  $R$  is smaller than 0.2. But fluctuations in the shower development, mainly in the crack regions, create tails reaching  $R \sim 0.6$  (Fig. 5.4).

From the longitudinal shape of the electromagnetic showers only, the energy fraction value  $R > 0.2 - 0.3$  can be considered as a potential veto trigger element against all kinds of background competing with electron identification.

### BEMC Angular Acceptance

The trigger efficiency can be strongly affected by the energy leakage out of the detector. Leakage problems arise at angles above  $173^\circ$  (close to the beam pipe) where electrons hit the BEMC near to the edge and the part of energy is lost due to the transversal size of the shower. Due to the triangular form of the innermost BEMC stacks the energy losses

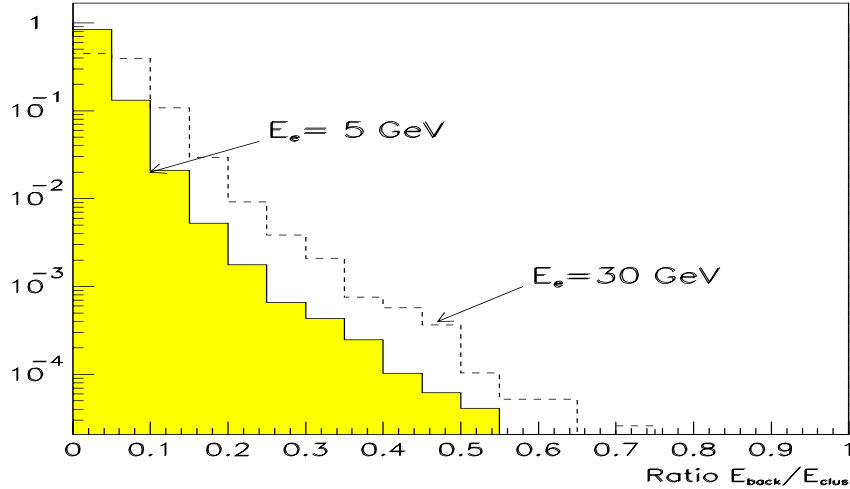


Figure 5.4: Longitudinal shape of 5 and 30 GeV electromagnetic showers in the terms of the energy ratio  $R = E_{back}/E_{clus}$ . Only events with energy deposit of  $> 80\%$  from the incident particle energy are considered.

are also dependent on the azimuthal angle  $\phi$  (Fig. 2.2).

The second area with leakage problems appears at angles smaller than  $156^\circ$  (Fig. 2.3). In this case BEMC depth seen by the traversing particle is not sufficient for full containment and since the geometry is not projective, the side leakage also plays an important role. Overlap with the liquid argon calorimeter is not very good and large energy corrections should be applied in this region.

Other areas where some fraction of the energy is lost, even in the good angular region, are in between the BEMC stacks, in the so called cracks.

### 5.1.2 Hadronic Showers in the BEMC

The BEMC with a total depth of  $1\lambda$  is very short for the full manifestation of the typical properties of hadronic showers which are usually needed to separate them from EM showers. More than  $1/3$  of all hadrons pass through the BEMC as a minimum ionizing particles and produce a typical peak at few hundred MeV (Fig. 5.5a). This means that they are invisible to the trigger. The rest of hadrons deposit more energy but with big fluctuations, causing large tails in the visible energy spectrum. Trigger efficiency for these kind of events is very small. Nevertheless this small efficiency is compensated by the high rates from photoproduction processes and therefore it is useful to separate electrons from hadrons already on the trigger level. Taking into account noise and thresholds there is no difference in the lateral size of EM and hadronic showers. Only the longitudinal size of the showers, expressed via parameter  $R = E_{back}/E_{clus}$ , is of some use (Fig. 5.5b) for  $e^-/h$  separation. With condition  $R < 0.1$  the hadronic rates could be suppressed by a factor 2 – 4. From the shapes of EM showers the  $R < 0.3 - 0.4$  values are desirable. But then

the achieved hadrons rate suppression factor is very small ( $< 2$ ) and therefore the usage of  $R$  parameter in the trigger is doubtful. The final decision will be made only after studies of the efficiency of the suppression of beam induced background.

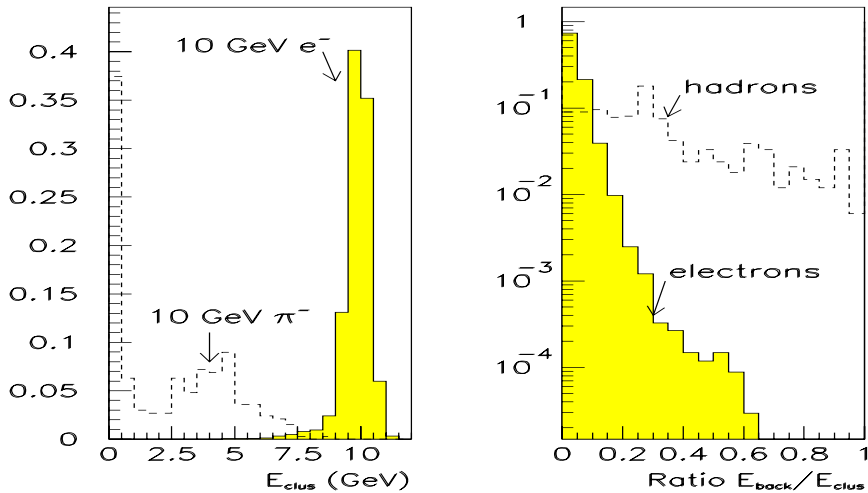


Figure 5.5: (a) Energy spectra of 10 GeV  $\pi^-$  and  $e^-$ . (b) A first look at the parameter  $R$  for the same particles is rather promising for  $e^-/\pi^-$  separation. But taking into account stack thresholds determined by the noise conditions, the achieved reduction of trigger rates is very small.

### 5.1.3 NC DIS and Photoproduction Events in the BEMC

#### Topology of the NC DIS in the BEMC

For NC DIS events topology studies in the BEMC mainly DJANGO MC generator was used [65]. DJANGO is an interface written in order to merge two stand alone MC generators: HERACLES [66], simulating electroweak processes with included first order radiative corrections, and LEPTO [67] for the subsequent simulation of QCD processes and fragmentation. MC generator studies indicate that the rate of hadrons and photons from the hadronic final state hitting BEMC together with the scattered electron starts to be comparable to that of electron itself only below  $E_e \sim 8 GeV$  (Fig. 5.6). In the table 5.1 the fractions of events with an additional particle in the BEMC are shown for different  $E_e$  bins and different MC generators. In the kinematical peak region ( $E_e > 22 GeV$ ) only 4 – 12 % of events have an another particle hitting the BEMC. The mean energy of these particles is  $\sim 1 GeV$  and the maximal energy limit  $4.7 GeV$  follows from the kinematics. The typical signature of these events will be therefore 1 high energy cluster in the BEMC.

Events in the kinematical peak are used for the absolute energy scale determination. But from the physics point of view, more interesting are events at higher  $y$ , i.e. at  $E_e < 22 GeV$ . The smaller the  $E_e$  the higher the probability of having another particles in the

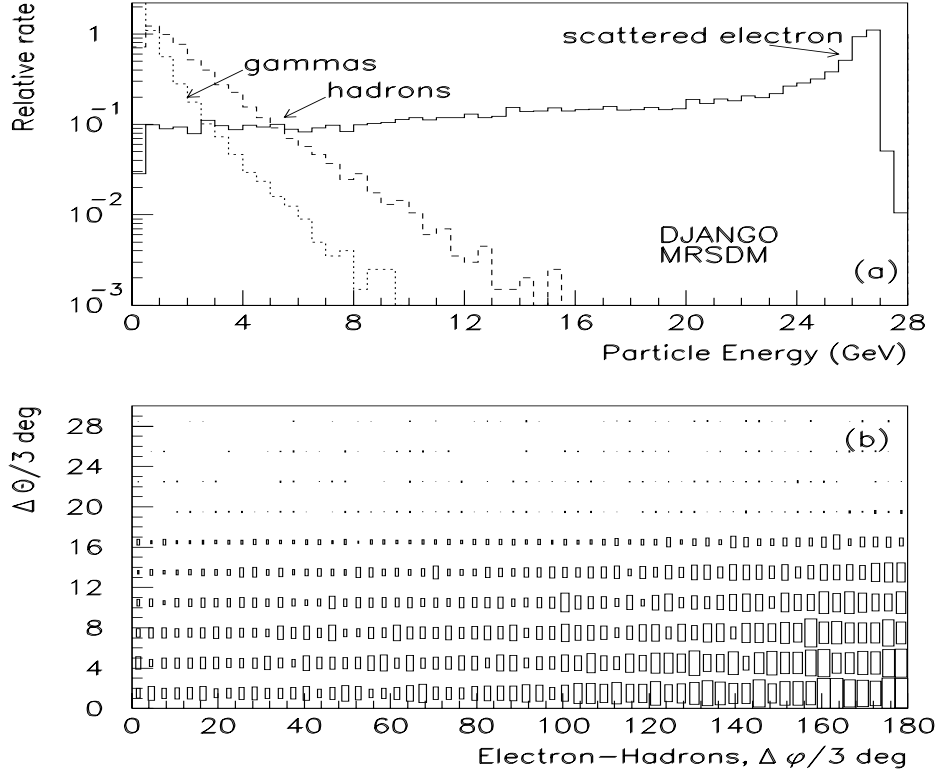


Figure 5.6: (a) Relative rates of electron and other particles hitting BEMC as a function of particles energy; (b) Angular separation,  $3^\circ$ /bin, between electron and hadrons hitting BEMC.

BEMC and the higher is also multiplicity and the maximal possible energy of these particles. On the Fig. 5.7 is shown the particles multiplicity distribution and resulting number of stacks found above HT resp. LT. The distributions are for two kinematical regions when the scattered electron energy in the BEMC is  $> 10 \text{ GeV}$  resp.  $4 \text{ GeV} < E_e < 10 \text{ GeV}$ .

Mean multiplicities and energy spectra of these electron "companions" are of course dependent on the fragmentation and hadronization schemes used in the different MC generators.

From the studies of electron angular separation from other particles hitting BEMC, it follows that electron appears rather isolated and accompanying particles tend to be scattered at the same polar angle  $\theta$  but back to back in azimuthal angle  $\phi$  (Fig. 5.6). The probability of hitting the same stack as electron is negligible ( $< 1\%$ ), and the probability of having another particle in the cluster of the size  $3 \times 3$  stacks is still rather small  $\sim 3.5\%$ .

For the trigger the consequences are clear: one has to consider the possibility of the existence of more energy clusters in the BEMC. With very high probability the electron will produce cluster with the highest energy (*leading cluster*) and photons and/or hadrons

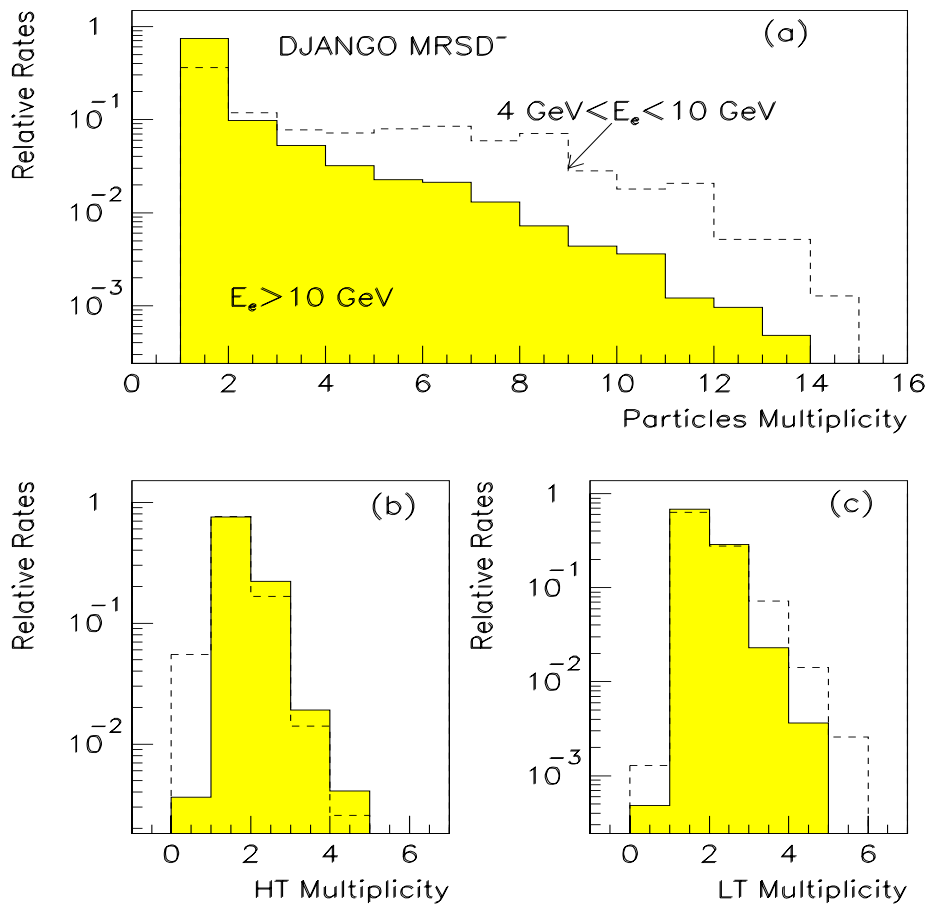


Figure 5.7: (a) Number of particles hitting the BEMC (with electron) for two different kinematical regions and corresponding number of stacks above 2.3 GeV (b) resp. 1.3 GeV (c).

particles	MC generator	$E_e (GeV)$			
		< 10	10 – 15	15 – 22	> 22
any particle	LEPTO	0.99	0.99	0.80	0.12
	DJANGO	0.63	0.63	0.42	0.04
hadrons	LEPTO	0.97	0.95	0.68	0.06
	DJANGO	0.56	0.55	0.32	0.02
gammas	LEPTO	0.85	0.77	0.52	0.07
	DJANGO	0.51	0.44	0.25	0.02

Table 5.1: Fraction of events with additional particles in BEMC for different scattered electron energies. The difference between two generators is in this case due to the electroweak radiative corrections applied in the DJANGO. It means that effective energy of the initial electron beam is smaller.

can produce additional clusters of smaller energies. Number of these clusters seen also by the trigger depends on the thresholds setting. Our goal is to trigger on the electrons down to  $4 - 6 GeV$  and this means that stack high threshold must be  $\sim 2 - 3 GeV$ . Differences in trigger efficiencies, when requiring exactly 1 trigger cluster (EQ1) or admitting also more (GE1) are shown on the Fig. 5.9a,b. The fraction of events with more than 1 trigger cluster is small, but the losses due to the requirement of only 1 cluster would introduce trigger bias into the most interesting kinematical region. Any exact cluster counting is not applicable for BEMC for many reasons:

- particles multiplicity hitting BEMC depends on the hadronization which is unknown and the subject of different model predictions
- limited BEMC angular acceptance
- BEMC is only an electromagnetic calorimeter with a bad hadronic energy measurement

Therefore only the most simple information about the cluster multiplicity can be used in the trigger:

- exactly 1 cluster has been identified (EQ1)
- 1 or more clusters were found (GE1)

Trigger element EQ1 could be used in the kinematical peak region, where the hadronic contribution to the trigger signal is negligible and on the other hand it could help at the background rejection. Trigger element GE1 is safe in the whole kinematical region.

### Photoproduction in the BEMC

Photoproduction processes ( $\gamma p$ ) are interactions of quasi real photons ( $Q^2 \rightarrow 0$ ) with the proton [69]. Due to very low momentum transfer  $Q^2$  the electron remains in the beam

pipe and takes away a large fraction of the total available energy ( $26.7 \text{ GeV}$ ). Therefore only hadrons and/or overlapping  $\gamma/h$  could mimic the electron.

For the generation of the photoproduction events we have used two MC programs: PYTHIA [70] (for hard scattering) and RAYVDM [71] (for soft processes). The energy spectrum of the particles from the  $\gamma p$  interactions hitting the BEMC has a peak at  $\sim 1 \text{ GeV}$  and tails reach up to  $12 - 15 \text{ GeV}$ . As a result of their high cross section these events could be a serious source of background for NC DIS trigger at  $y > 0.7$ . Although the scattered electron from NC DIS will be isolated and the fake 'electron' from  $\gamma p$  interaction will be mostly accompanied by other particles, this feature is not usable in the trigger, due to the low energy of  $\gamma p$  produced particles. After applying realistic stack thresholds all differences in the event topologies escape and are not projected nor into the cluster size, nor into the total number of stacks above LT or HT. To get rid of the photoproduction background is a big problem even for the off line physics analysis, where information from the whole H1 detector is available. The expected contribution to the NC DIS BSET trigger rates at the design luminosity depends on the thresholds and e.g for CL1=4 GeV it could reach a few Hz.

#### 5.1.4 Machine Background Simulations

The background event rate from the HERA machine is expected to be five orders of magnitude larger than that from NC DIS. It is necessary to study the signatures of the background events and to find effective algorithms to reduce their rates to the acceptable level. The main background load is delivered to the detectors close to the beam pipe : Plug, IF part of the LAr calorimeter and BEMC. Tails of the energy deposits reach a few hundred GeV. It is clear that these are the most difficult trigger areas of the H1 detector. Of course also tracking detectors suffer, mainly because they are sensitive down to energies of a few  $100 \text{ MeV}$ . Tracks pointing outside the H1 detector are a clear signature for this kind of background (Fig. 4.1).

The problematic region of the LAr calorimeter is expected to be the inner forward (IF) part, where the energy thresholds have to be set much higher than in the rest of the calorimeter. The thresholds in the forward and central barrel part (FB, CB) are not determined by the background energies but rather by the noise level of the calorimeter.

In further studies we will concentrate on the BEMC as the main detector for measuring and triggering electrons scattered with low  $Q^2$ ,  $x$  values. Triggering in this area is difficult because the background energy spectrum covers the whole physics energy spectrum and with much higher rates (Table 5.2, 5.3).

**Beam-Gas Simulations** Beam-gas interactions are simulated in three steps, with three different MC packages: MODC (modified cluster generator), BEAMLIN and H1SIM.

MODC [49] is an empirical MC simulation package, i.e. it is a mixture of some basic physics ideas on hadron-hadron collisions tuned to the UA5 experimental data. The primary interaction of the proton beam with the HERA rest gas molecules, which can take place starting at  $z \simeq -80 \text{ m}$ , is simulated by the MODC and further transport of secondaries as well as tracking up to this interaction point is made by the BEAMLIN simulation program. For the simulation of secondary hadronic interactions with the beam pipe the standard GHEISHA module in the framework of the GEANT simulation package

is used. There are no secondary beam-gas interactions. At  $z = -3.37\text{ m}$  H1SIM takes over the 4-vectors of produced particles, which are stored in the standard BOS banks by the MODC+BEAMLIN programs. Then the simulation in the H1 detector itself follows [79].

The beam-gas events (BGE) which originate in the interaction region are most difficult to be recognized. The histogramming technique used by the *ZVTX* trigger in coincidence with veto from TOF reduces the rate to few hundred Hz or less. This is still too much and additional subtriggers are put into the coincidence such as e.g.  $DC - r\phi$  and/or BSET trigger.

**Beam-Wall Simulations** Beam-wall events (BWE) rate is determined mainly by the proton beam life time. Usually the values between 10-40 hours are considered. Very important is also the efficiency of the collimators (scrapers) in the straight sections of the HERA ring, which are supposed to reduce the off-momentum proton flux by factor  $\sim 100$ . It means that already from this very first simple considerations any BWE rate calculation starts with an uncertainty factor of  $\geq 4$ . Final decisive element influencing the BWE rate is the beam pipe geometry and geometry of the quadrupole magnets QS  $\simeq 40\text{ m}$  in front of the H1 detector [79].

BWE generation begins therefore at the QS magnets, where the hadronic interactions of the  $820\text{ GeV}$  protons are simulated with GEISHA or FLUKA programs. Products of these interactions are further transported over 36 m by the BEAMLIN program. At the same point as in the case of BGE simulations ( $z = -3.37\text{ m}$ ) H1SIM program takes over all particles produced in both previous steps and from this moment further secondary interactions in the volume of H1 detector can occur [79].

### Background Events in BEMC

BEMC is the first major detector hit by the proton induced background and the trigger is exposed to very high rates and large energy depositions. Typical rates and energy spectra per stack as a function of radial distance from the beam axis (stacks are grouped into so called rings) are shown on the Fig. 5.8. Effective separation of the physics and background signals mainly in the innermost part of the detector, closest to the beam pipe, is a big challenge.

Off-momentum protons interact with the different elements in and/or with the beam pipe itself and produce hadronic showers. Large fraction ( $> 98\%$ ) of these events depositing energy in the BEMC will be tagged by the TOF veto counter ( $\overline{TOF}$ ) and thus can be rejected at L1. But even the remaining 2% means a trigger rate of the order of few hundred Hz. Unfortunately, an ion getter pump (at  $z = -2.06; -2.24\text{ m}$ ) and a synchrotron radiation mask (at  $z = -1.7\text{ m}$ ) are placed directly between the TOF scintillator planes in the beam pipe and under the BEMC resp. Background events originating at these scatter sources cannot be vetoed by the coincidence signal from both TOF planes. A looser trigger condition requiring a veto signal only from one TOF plane ( $\overline{TOF1}$ ), closer to the BEMC, reduces the rate by additional factor  $\sim 3 - 4$ .

As the highest rates with biggest energies are coming from the 4 innermost triangular stacks, we have tried to treat them separately. First we have excluded them from the trigger as a possible cluster initiators ( $I_{out}$ ), i.e. HT was set to  $> 100\text{ GeV}$ . But low thresholds are treated the same way as other stacks, i.e. they are allowed to contribute to the energy sums.

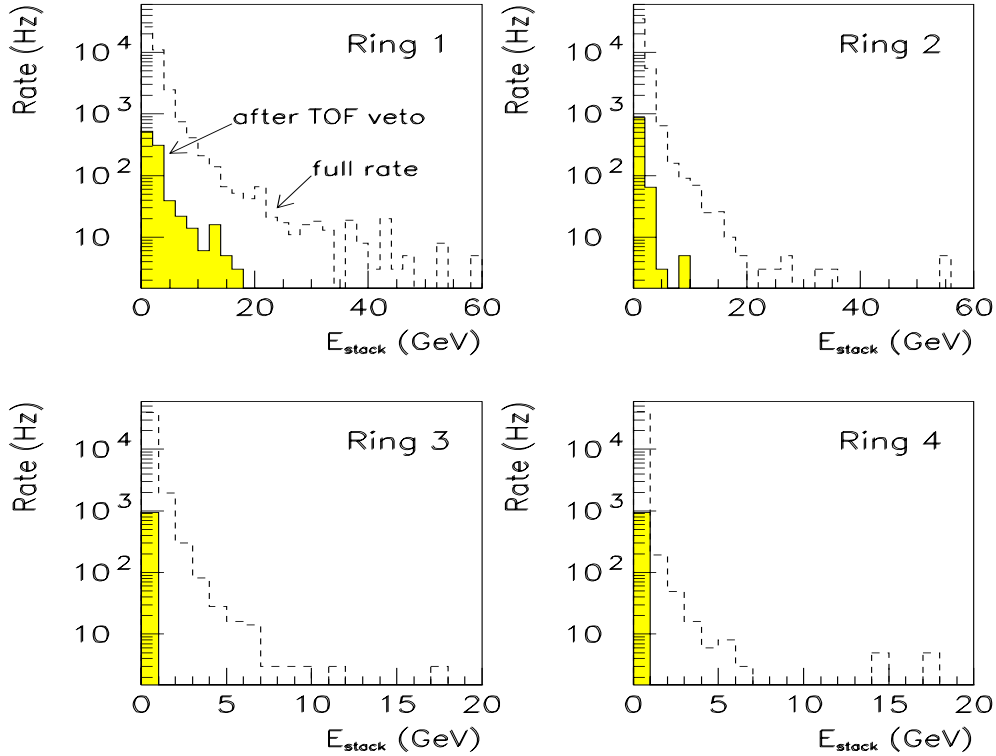


Figure 5.8: Radial dependence of rates and energy spectra for individual stacks grouped into so called rings. Highest rates and biggest energies are deposited in the innermost ring 1. TOF veto is very effective mainly for outer rings 3 and 4.

This operation alone helped to reduce the background rate by factor  $\sim 3 - 10$  depending on the trigger element considered. A less severe condition of setting HT at  $10 \text{ GeV}$  ( $I_{10}$ ) brought also a small improvement and we have thus achieved a rate reduction by a factor  $\leq 2$ . This trigger condition is meant for triggering of electrons in the kinematical peak ( $E_e > 22 \text{ GeV}$ ) and enabling thus in situ calibration of the triangular stacks. For these kind of events we can require only one of these innermost stacks to be above HT. This brings another factor  $\sim 2$  into the background rejection. Another possibility is to set also other stacks to different HT - so called ring dependent thresholds could be used. The closer the stack to the beam axis, the higher its HT. But due to the bad  $r - \phi$  symmetry of the BEMC stacks, this threshold setting would complicate the off-line trigger acceptance calculation. Typical rates expected from the BSET trigger elements itself and put into coincidence with TOF and/or special treatment of the innermost triangular stacks are shown in the Table 5.2.

Another potential trigger element mentioned in the studies of longitudinal shape of the showers, namely the ratio  $R = E_{BACK}/E_{CLUST}$ , brings only very small rejection of

the events triggered by GE1, CL1, CL2, CL3 or BTOT. The rejection factor depends on the LT. The lower the LT could be set the better rejection achieved. But at realistic  $LT \sim 1.0 GeV$  and at  $R < 0.3$  the achieved reduction by factor  $\sim 1.1$  is not attractive enough to be realized in the hardware. Even at  $LT = 0.5 GeV$  and  $R < 0.2$  maximal reduction achieved was only  $\sim 1.5$ . Main reason for this small effectivity is the fact that innermost triangular stacks, where the background energy is concentrated, have no hadronic part and thus the ratio for these events is  $R = 0$ .

Up to now we have considered only the BSET trigger itself (with an inevitable  $\overline{TOF}$ ) and we have found that triggering down to the cluster thresholds of  $6 - 8 GeV$  is possible, i.e. background rates are acceptable even at full design luminosity. But triggering at smaller energies will be a bigger problem and more stringent conditions must be used. For this purpose the coincidence with other subdetectors is required.

The TOF detector provides also TOF-IA (interaction window) signal tagging events from the interaction region. In the ideal case there should be no background events with this trigger bit.

Another direct neighbour is the BPC providing only simple information yes/no about hits in 3 out of 4 wire planes (BPC-S). There is no spatial information available on L1 which could be correlated with the BEMC cluster. Therefore this trigger coincidence is not very powerful and another shortcoming is that BPC does not cover the whole BEMC.

In the simulation we have tested matching of the BEMC stack above HT with the BPC hit wires (BPC-M) <sup>1</sup>. For this purpose we have grouped 16 wires into 1 readout unit called strip. This way we have obtained 20 strips per plane, each of 8 cm width. For stacks above HT the corresponding, matching strips in 3 out of 4 planes were looked for. Matching requirement strongly reduces the BSET trigger rates as can be seen from the Table 5.3-column BPC.

Central tracking detectors as CJC and MWPC are much more effective in the coincidence with BSET as BPC-S and are comparable with BPC-M.

The summary of expected background rates from the BSET trigger elements combined with tracking triggers is shown in the Table 5.3.

### 5.1.5 Proposed BEMC Electron Trigger Elements: Summary

As seen before the basic trigger element is a stack energy and for each stack two thresholds are defined,  $LT$  enabling contribution to the energy sums, and the  $HT$  used as a high energy cluster initiator. Notion of the high energy cluster arose from the fact that the size of the electromagnetic showers is limited to a few adjacent stacks. The groups of hot stacks - **clusters** - are found from the 2-dimensional [X,Y] projections. With this procedure only a limited cluster counting precision is achievable ( $EQ1$ ,  $GE1$ ), but as shown before there is no use of exact cluster multiplicities counting. Cluster search is done simultaneously on both threshold planes, i.e. between stacks above  $LT$  as well as between stacks above  $HT$ .

The proposed BSET trigger elements used in the simulations to define more efficient trigger algorithm for NC DIS are:

- number of clusters in the low threshold plane

---

<sup>1</sup>In the meantime realized also in the hardware and prepared to be used on the L3 trigger level.

BSET *TE	BSET Triggers Rates (Hz)							
	EQ1	GE1	BTOT	CL1	CL2	CL3	LTOR	IST
BWE	9720	18115	17755	14470	11420	5120	25770	14865
BGE	6741	8532	7257	5280	3402	750	15747	6465
<b>TOF*</b>								
BWE	200	225	105	90	60	15	460	205
BGE	186	192	96	51	54	9	480	174
<b>TOF1*</b>								
BWE	60	60	15	15	10	5	110	55
BGE	60	60	33	30	24	0	129	48
<b>I<sub>10</sub>*</b>								
BWE	8345	11700	17755	10155	8450	3970	25770	1245
BGE	3588	4029	7257	2811	2049	534	15747	447
<b>I<sub>10</sub> * TOF*</b>								
BWE	45	50	105	30	25	15	460	20
BGE	39	42	96	30	30	6	480	15
<b>I<sub>10</sub> * TOF1*</b>								
BWE	15	15	15	10	10	5	110	10
BGE	19	15	33	6	6	0	129	3
<b>I<sub>out</sub>*</b>								
BWE	2920	3250	17755	2140	1135	185	25747	0
BGE	1932	2067	7257	1014	483	48	15747	0
<b>I<sub>out</sub> * TOF*</b>								
BWE	20	20	105	5	0	0	460	0
BGE	18	18	96	6	6	6	480	0
<b>I<sub>out</sub> * TOF1*</b>								
BWE	0	10	15	0	0	0	110	0
BGE	12	12	33	3	3	0	129	0

Table 5.2: Trigger rates from beam-wall (BWE) and beam-gas (BGE) background events for BSET trigger elements alone and put into coincidence with vetos from TOF and/or special treatment of the innermost stacks ( $I_{out}$  - excluded completely,  $I_{10}$  -  $HT=10$  GeV). Cluster and total energy thresholds CL1, CL2, CL3, BTOT are 4, 7, 15 and 4 GeV respectively. Stack thresholds are  $HT = 2.3$  GeV and  $LT = 1.3$  GeV.

$BSET^*$	Combined Triggers Rates (Hz)						
	ZVTX		DC - $R\phi$	BPC		FWR	Tracks
	$-t_0$	$-\text{sig1}$	$-\text{thr0}$	-S	-M	$-t_0$	$-t_0$
<b>GE1 * TOF*</b>							
BWE	80	25	40	195	45	70	90
BGE	81	15	30	156	12	66	102
<b>GE1 * TOF1*</b>							
BWE	25	10	15	50	0	20	25
BGE	30	6	15	51	3	24	36
<b>GE1 * I<sub>10</sub> * TOF*</b>							
BWE	15	5	10	45	0	15	15
BGE	81	15	36	156	12	66	112
<b>GE1 * I<sub>out</sub> * TOF*</b>							
BWE	5	0	5	20	0	5	5
BGE	3	3	3	18	0	3	3
<b>CL1 * TOF*</b>							
BWE	45	10	15	85	25	30	45
BGE	39	12	15	63	3	30	45
<b>CL1 * TOF1*</b>							
BWE	10	5	0	15	0	5	10
BGE	18	6	9	24	0	15	18
<b>CL1 * I<sub>10</sub> * TOF*</b>							
BWE	10	5	5	25	0	10	10
BGE	39	12	15	63	3	30	45
<b>CL1 * I<sub>out</sub> * TOF*</b>							
BWE	0	0	0	5	0	0	0
BGE	3	3	0	6	0	3	3
<b>BTOT * TOF*</b>							
BWE	55	10	25	90	-	40	60
BGE	48	15	18	78	-	42	57
<b>BTOT * TOF1*</b>							
BWE	10	5	0	15	-	5	10
BGE	18	6	9	27	-	18	21

Table 5.3: Trigger rates from beam-wall (BWE) and beam-gas (BGE) background events for BSET trigger elements GE1, CL1 and BTOT put into coincidence with different tracker triggers. BPC is shown for standard mode (S) and mode requiring matching stack above HT in BSET (M). Tracks  $-t_0$  is OR'd from ZVTX-, forward ray (FWR) and CJC  $t_0$ . Meaning of the TOF vetos and values of BSET thresholds are the same as in the previous table.

- number of clusters in the high threshold plane (**EQ1, GE1**)
- three cluster energy sums (**CL1, CL2, CL3**)
- BEMC total energy (**BTOT**)
- number of hits above  $HT$  in the innermost stacks (**IST**)
- at least 1 stack above  $LT$  (**LTOR**)

## 5.2 Trigger Algorithms for NC DIS

### 5.2.1 Low $Q^2$ Events

The BEMC detector and trigger are vital for the NC DIS at low  $Q^2$ . The main task of the trigger on L1 is to reduce high background rate below 100 Hz and still retain high efficiency for NC DIS events. From the trigger point of view we have found three regions in the BEMC angular acceptance (Fig. 1.2) with different levels of difficulties:

1. *low y* region                      - electron energy  $E_e > 10 GeV$ ,  
relatively small problems with trigger algorithm and rates
2. *low x – high y* region        -  $E_e < 10 GeV$ , problems with background rates
3. *large  $\theta_e$*  region                - problems with background rates and  
energy leakage for both previous  $y$  regions

#### Low $y$ Trigger

When considering electron energies above  $\sim 10 - 15 GeV$  the rates from the BSET cluster trigger are reasonable and efficiency for the NC DIS is very high. Cluster trigger CL3 with  $E_{th} = 15 GeV$  can be used as a kinematic peak trigger (Fig. 5.9) and as a trigger monitoring the TOF performance.

But this kinematical region is not the most interesting one, although very useful for the determination of the BEMC absolute energy scale.

#### Low $x$ - High $y$ Trigger

The more interesting *low x – high y* region, where signatures of new physics are expected, will be covered by GE1, CL1, CL2 and BTOT trigger elements (Fig. 5.9). But running with lower calorimeter thresholds means immediate increase of the background rates. Nevertheless in the first period of HERA operation at only  $\sim 1\%$  of the design luminosity, it should be possible to run CL2 trigger stand alone at rather low thresholds ( $3 - 4 GeV$ ) due to the fact that also background rates are expected to be 2 orders of magnitude smaller.<sup>2</sup>

At full design luminosity the minimal trigger cluster threshold value at which it is aimed to run the stand alone BSET trigger CL2 is  $6 - 8 GeV$ . This would mean  $> 90\%$  trigger efficiency for  $8 - 10 GeV$  electrons. Therefore the calorimeter CL2 trigger alone gives a rather poor efficiency for  $y > 0.6$  (Fig. 5.11). To trigger electrons below 8-10 GeV

---

<sup>2</sup>It was really the case, see Chapter 7.

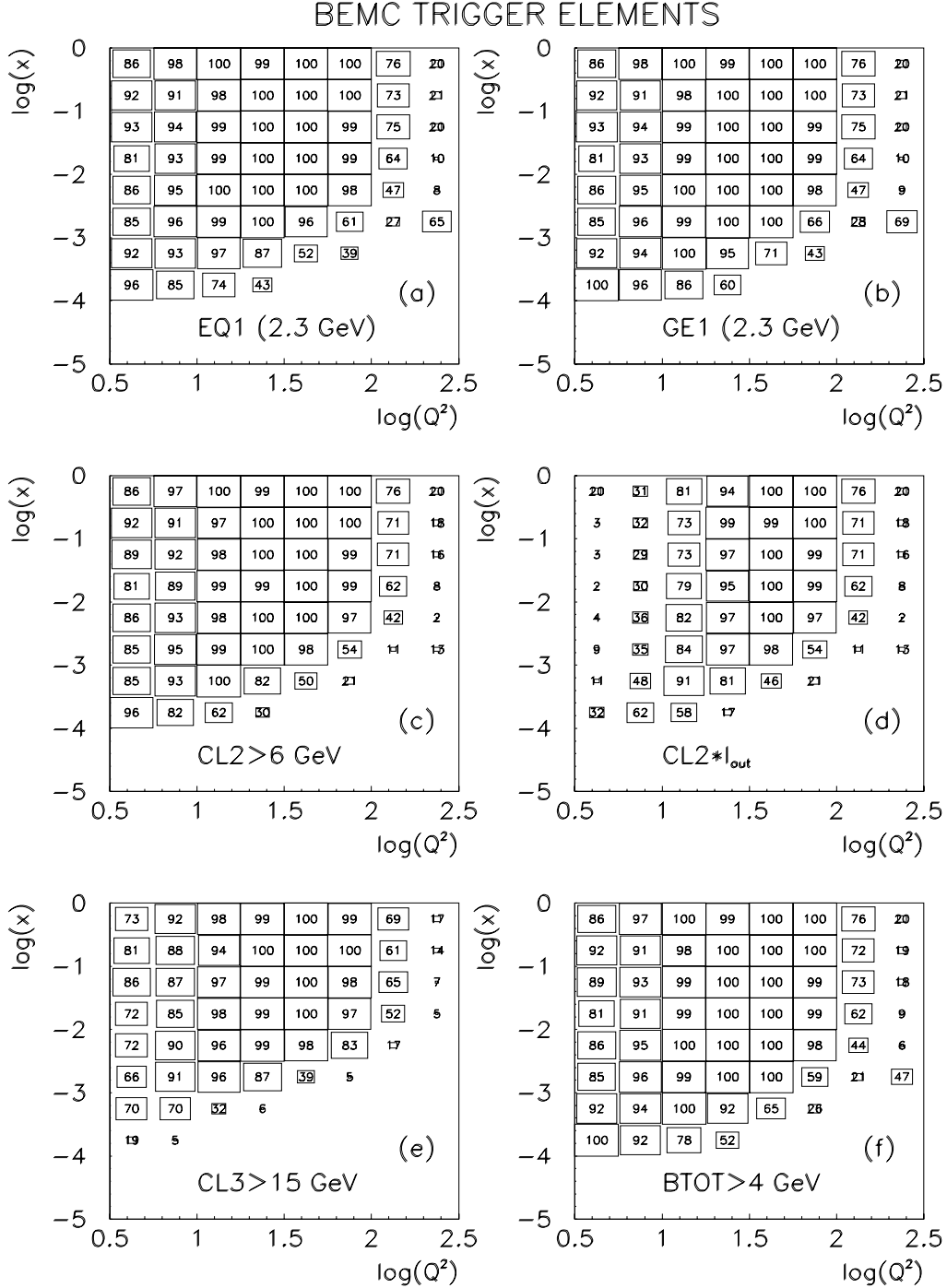


Figure 5.9: Trigger acceptance of BSET trigger elements for events generated flat in  $\log(Q^2)$ - $\log(x)$  plane according the  $MRS D^-$  distribution from LEPTO 6.1. (a)-(b) Importance of the GE1 condition at high  $y$  when compared to EQ1. (c)-(d) The effect of excluding the innermost stacks from the cluster trigger is shown for CL2. Cluster trigger threshold values clearly affect efficiency in the whole BEMC for high  $y$  region and independently from  $y$  at the BEMC inner and outer borders (b)-(f).

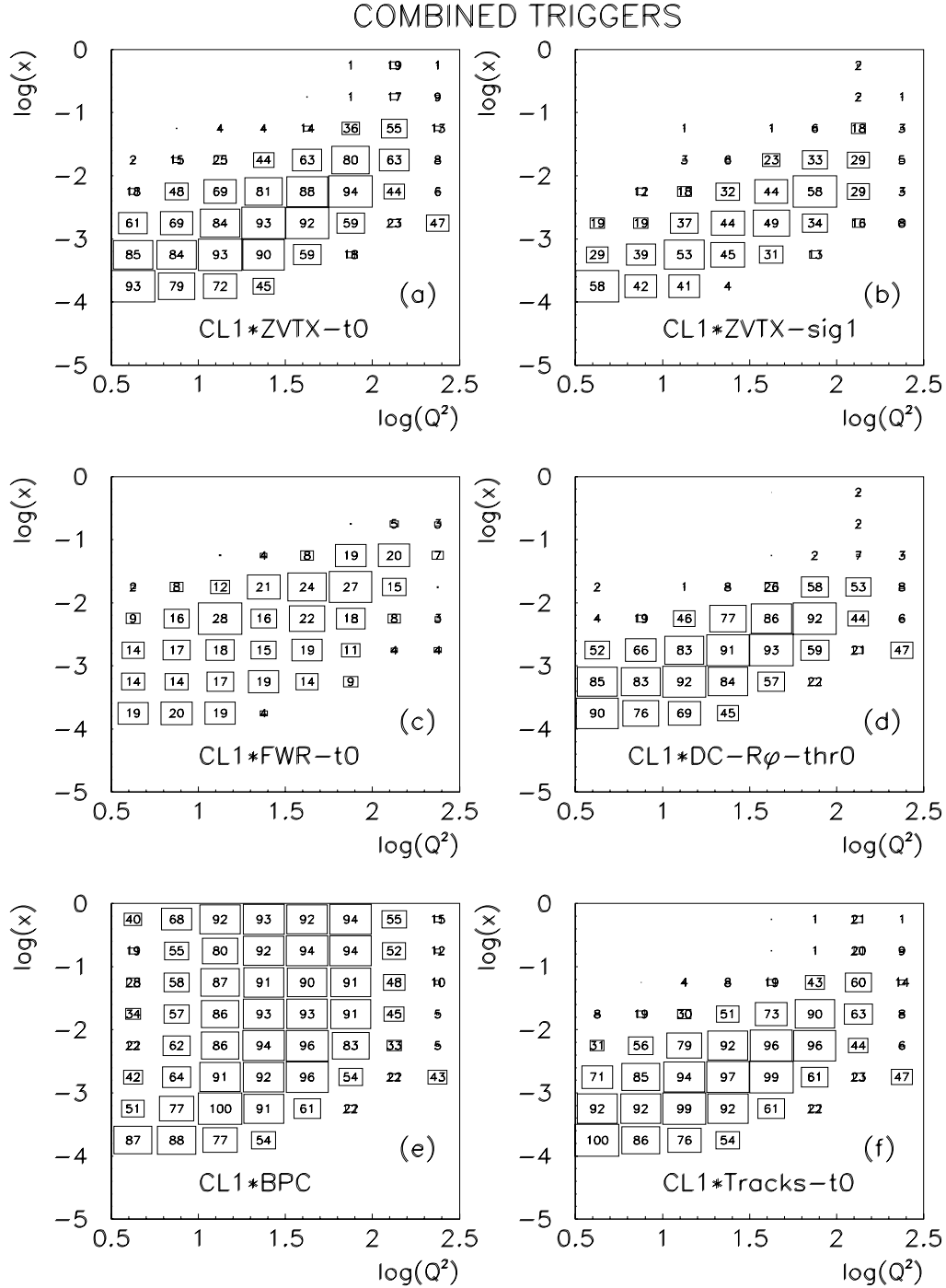


Figure 5.10: Trigger acceptance of the BSET CL1 trigger ( $> 4\text{ GeV}$ ) in coincidence with tracker triggers.

the CL1 cluster trigger threshold must be set to 4-5 GeV. Also GE1 at 2-3 GeV could be considered, but both of course only in coincidence with other triggers. Another possibility is to run CL1, GE1 also stand alone but with the so called prescaling. This means that according the prescale factor  $n$  only each  $n^{\text{th}}$  trigger would be accepted. This mode of operation is acceptable only if the prescale factor is not too big allowing accumulation of reasonable amount of the data. The possible triggers are briefly discussed hereafter.

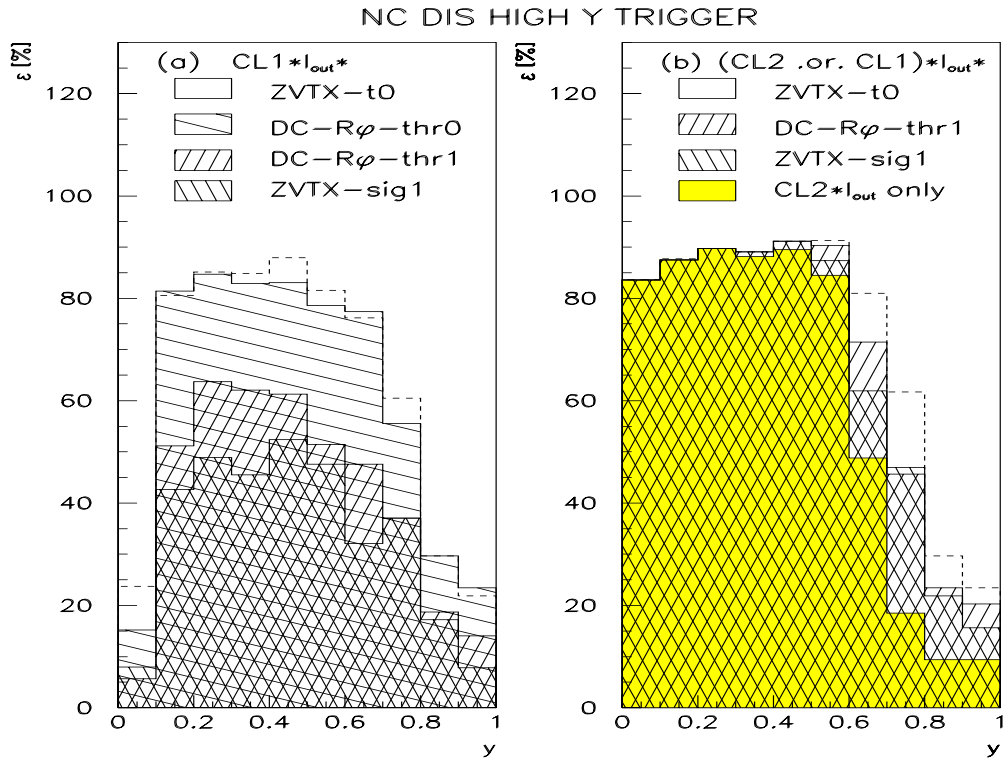


Figure 5.11: The trigger  $y$ -dependence for  $4 \text{ GeV}^2 < Q^2 < 100 \text{ GeV}^2$  with excluded innermost triangles from the cluster trigger. (a)  $CL1 > 4.0 \text{ GeV}$  combined with tracker triggers. (b) It is seen that efficiency of  $CL2 > 7 \text{ GeV}$  steeply falls down at  $y > 0.6$  and that combined triggers are needed for the high  $y$  region.

### BSET in Coincidence with other Triggers

Common characteristics of all triggers put into coincidence with the BSET low threshold triggers in order to cover the high  $y$  region (Fig. 5.11) is that they are relying on correlations between a low energy electron in the BEMC and a hadronic activity in other parts of the H1 detector. Partons hadronization especially at low  $x$  is not very well known. It is a subject of extrapolations from higher  $x$  behaviour and therefore could be model dependent. As far as we don't have a reliable electron trigger at high  $y$ , the trigger efficiency cannot be measured directly from the data. Monte Carlo simulations are needed and model

dependence must be studied. A short overview of the properties of the triggers proposed to cover the high  $y$  region in the kinematical plane is given here.

**BSET\*TOF-IA** Here we use the fact that the BEMC is only an electromagnetic calorimeter, very transparent to hadrons which are mostly simply punching through the BEMC and TOF. So TOF-IA is most effective at *high*  $-y$  and at *large*  $-\theta_e$  (Fig. 5.12). Limited TOF angular acceptance ( $\theta_e > 160^\circ$ ) and possible dependence on the parton fragmentation assumptions complicate the final trigger acceptance (efficiency) calculation.

**BSET\*BPC** Very high sensitivity to charged particles and its position in the backward region close to the beam pipe are reasons why BPC delivers high trigger rates. Major drawbacks are a not complete coverage of the BEMC and the lack of spatial information about hits on the trigger level. Requiring BPC coincidence with BSET cuts off the inner- and outer- most regions of BEMC (Fig. 5.12a). In order not to lose these events, these boundary BEMC regions should be predefined as always active for the BPC trigger. This needs some hardware changes in order to extract BSET information about activities in the outermost two columns resp. rows.

Nevertheless the BPC could be used, without any changes, as a veto against synchrotron radiation background if this turns out to be a serious problem.

**BSET\*ZVTX** ZVTX trigger requires activity in the central and/or forward H1 region. It is not efficient to low  $y$  events, for which quasielastically backwards scattered electron and proton remnants in the very forward H1 region are typical characteristics.

**BSET\*DC-R $\phi$**  The central drift chamber trigger angular acceptance is limited to  $\theta \sim 25^\circ - 155^\circ$ . Therefore its efficiency for  $\theta_e > 155^\circ$  is in fact only the reflection of hadronic activity in the central region.

**BSET\*FRW- $t_0$**  Forward ray trigger covers the angular range  $\theta \sim 7^\circ - 25^\circ$  and is sensitive up to rather low  $y$ . In order to explain the efficiency at low  $Q^2$  the same arguments as for the previous trackers are valid.

**BSET\*(Trackers OR TOF-IA)** *Tracks*- $t_0$ , i.e. the 'OR' from all available tracker  $t_0$  ensures coverage of the whole H1 angular range but at the same time is very sensitive to the background conditions. A better background rejection can be achieved by coincidence requirements as e.g. *ZVTX* - *sig1* \* *DC* - *R $\phi$*  - *thr0*. On the other hand simultaneous decrease of physics efficiency is unavoidable. Reasonable compromise is determined by the background conditions.

To cover the central and backward parts the 'OR' between *ZVTX* - *sig1* and *TOF* - *IA* is very efficient. The background rates are in this case dominated by the *ZVTX* trigger, the contribution of *TOF* - *IA* should be negligible.

### Trigger at Large Angles

Excluding the innermost triangles from the BSET cluster trigger allows to reduce the CL2 (at 6 GeV) rate almost by factor 20. The loss of events is  $\phi$  dependent for  $\theta_e \sim 173^\circ - 175^\circ$ .

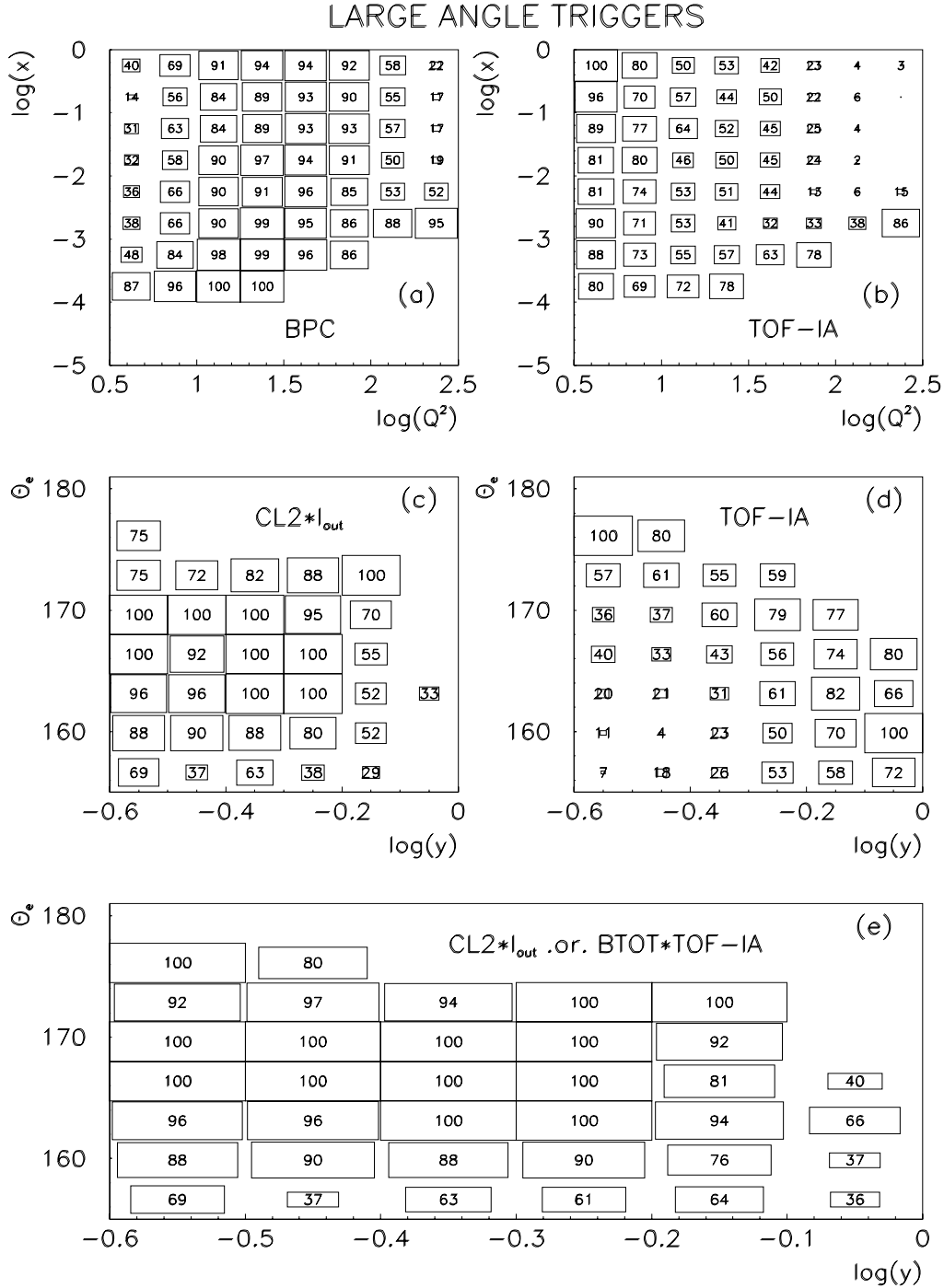


Figure 5.12: (a), (b) BPC resp. TOF-IA trigger acceptance in  $\log(x)$ - $\log(Q^2)$  plane. (c) CL2 trigger acceptance at large  $\theta_e$  and high  $y$  with excluded innermost stacks. (d) Stand alone TOF-IA is complementary to CL2\*I<sub>out</sub> (the same as (b) but now in  $y$ - $\theta_e$  plane). (e) Resulting acceptance if CL2 trigger is 'OR'ed with BEMC total energy put into coincidence with TOF-IA signal. Significant improvements at large angles and high  $y$  are observable when compared to (c).

But this is no tragedy because the  $Q^2$  of rejected events is below  $10 \text{ GeV}^2$  and this is a region of bad acceptance where the systematic errors of the structure function  $F_2$  measurements are above 10% (Fig. 1.3). So the real losses due to the exclusion of the innermost BEMC stacks from the trigger are negligible. Part of the physics could still be recovered by considering events with interaction points in the very forward region.

Scattering at low  $x$  and very large angles  $\theta_e$  (in H1 coordinate system) or in other words with a very small deflection of incoming electrons reminds fixed target experiments. Hadrons from the current jet are in this case mostly produced into the backward region (Fig. 1.2). As already mentioned, parton fragmentation depends on the model assumptions and the central tracking detectors could or could not be sensitive to these kind of events.

A solution avoiding tracker triggers could be TOF-IA. TOF-IA is sensitive not only to punch-through hadrons but also to high energy electrons ( $\sim 30 \text{ GeV}$ ) and close to the beam pipe to all electrons hitting only the BEMC edge. In order to profit from disabled triangular stacks HT ( $I_{out}$ ) and still to be sensitive at large  $\theta_e$ , the BTOT energy trigger could be used in coincidence with TOF-IA (Fig. 5.12e).

Despite all these problems the data with quasielastically scattered electron in the triangular stacks will be needed for their energy calibration. One solution could be to have dedicated runs for this purpose with the same or slightly higher  $HT$  as are used for all other stacks.

Another possibility is to set the innermost stacks  $HT$  at  $10 \text{ GeV}$  ( $I_{10}$ ) and to take data during all runs. For the CL3 trigger it would mean higher, but still acceptable background rate (Table 5.2). CL3 trigger can be even prescaled and for CL2, CL1 the veto from innermost stacks above HT ( $\overline{IST}$ ) is equivalent to the exclusion of these stacks from the cluster trigger completely.

### 5.2.2 High $Q^2$ Events

As the results of the simulations show this region could be covered very well by any of the LAr triggers. Most powerful is the  $e^-$ -trigger. The energy depositions and rates from the beam-wall and beam-gas background in the barrel part of the LAr are small. Therefore the limiting factor for the lowest threshold here is the noise in the calorimeter read-out and trigger chain. The most difficult is the inner forward (IF) part of the calorimeter, where high rates with big energy deposits from the proton induced background are expected. Therefore the trigger threshold must be much higher than in other parts.

The most effective LAr triggers for the high  $Q^2$  NC DIS found from the simulation studies are the following ones:

1. electron trigger (Fig. 5.13)
2. transversal energy -  $E_T$
3. topological sums -  $E_{BAR}, (E_{FB}, E_{CB})$

The LAr electron trigger [40] is based on two energy thresholds requiring some minimal energy in the electromagnetic part of the BT and allowing some maximal energy leakage into the corresponding hadronic part. This hadronic veto is supposed to reject hadrons which could fake electrons. Both these thresholds vary for the different parts of the LAr calorimeter (Table 5.4). They take into account the event kinematics and also the fact,

that the electromagnetic calorimeter has not the same depth in all its parts (it changes from  $20X_0$  in the central barrel to  $30X_0$  in the forward barrel).

BT part	CALORIMETER PART		
	IF (inner forward)	FB (forward barrel)	CB (central barrel)
EM threshold (GeV)	30	10	8
HAD veto (GeV)	5	4	3

Table 5.4: *LAr second electron trigger thresholds in different parts of the calorimeter*

Therefore one has to set carefully the proper thresholds. E.g. a too low hadronic veto threshold could create holes in the trigger efficiency coverage of the  $\log(x)$ - $\log(Q^2)$  plane. However this could be compensated by the transversal energy  $E_T$  or e.g. barrel energy trigger. This is an illustration of the importance of trigger redundancy in the same kinematical region.

### 5.2.3 Subtriggers for NC DIS: Summary

From the trigger elements available at L1 level a lot of different combinations could be built. Some of them which have been simulated for NC DIS scattering are summarized below. Many of them are very similar in their acceptance and of course not all must be enabled simultaneously. With only a few of them the kinematical region of interest could be effectively covered. For example the achieved acceptance for the NC DIS with combination ('OR') of subtriggers 2, 6, 12, 16, 21 is shown on the Fig. 5.13.

1.  $CL2 * \overline{TOF}$
2.  $CL2 * \overline{IST} * \overline{TOF}$
3.  $CL3 * \overline{TOF}$
4.  $CL1 * ZVTX - t_0 * \overline{TOF}$
5.  $CL1 * ZVTX - sig1 * \overline{TOF}$
6.  $CL1 * DC - R\phi - thr0 * \overline{TOF}$
7.  $CL1 * BPC * \overline{TOF}$
8.  $CL1 * TOF - IA * \overline{TOF}$
9.  $CL1 * FWR - t_0 * \overline{TOF}$
10.  $CL1 * Tracks - t_0 * \overline{TOF}$
11.  $CL1 * ZVTX - sig1 * DC - R\phi - thr0 * \overline{TOF}$
12.  $CL1 * \overline{IST} * DC - R\phi - thr0 * \overline{TOF}$

13.  $GE1 * ZVTX - sig1 * DC - R\phi - thr0 * \overline{TOF}$
14.  $BTOT * ZVTX - sig1 * \overline{TOF}$
15.  $BTOT * DC - R\phi - thr0 * \overline{TOF}$
16.  **$BTOT * TOF - IA * \overline{TOF}$**
17.  $GE1 * ZVTX - sig1 * \overline{TOF}$
18.  $GE1 * DC - R\phi - thr0 * \overline{TOF}$
19.  $GE1 * TOF - IA * \overline{TOF}$
20.  $ZVTX - sig1 * DC - R\phi - thr0 * \overline{TOF}$
21.  **$LAr - Electron * \overline{TOF}$**
22.  $LAr - E_T * \overline{TOF}$
23.  $LAr - E_{BAR} * \overline{TOF}$

A limiting factor for the central part of the LAr calorimeter trigger will be the noise in the trigger itself. The robust LAr triggers as electron,  $E_T$  or  $E_{BAR}$  topological sums will cover the high  $Q^2$  region ( $Q^2 > 100 GeV$ ).

In the low  $Q^2$  region the situation is more complicated. Background conditions are in this case dominating factors which determine the BSET energy thresholds.

Stand alone BSET cluster trigger could be used probably up to  $y \sim 0.6$ . For higher  $y$  values BSET energy triggers must be put into coincidence with trackers or TOF-IA triggers in order to cope with high background rates. Coincidence between tracker triggers only, as e.g.  $ZVTX*DC-R\phi$  is also very useful for the problematic high  $y$  region. Tracker triggers are very efficient, a part from at low  $y$ , in the whole kinematical region but for these still more studies will be needed mainly on the possible model dependence.

A dedicated electron trigger at *large*  $\theta$  – *high*  $y$  allowing to calculate trigger efficiency directly from the data as well as redundancy in the low  $Q^2$  trigger is missing at present.

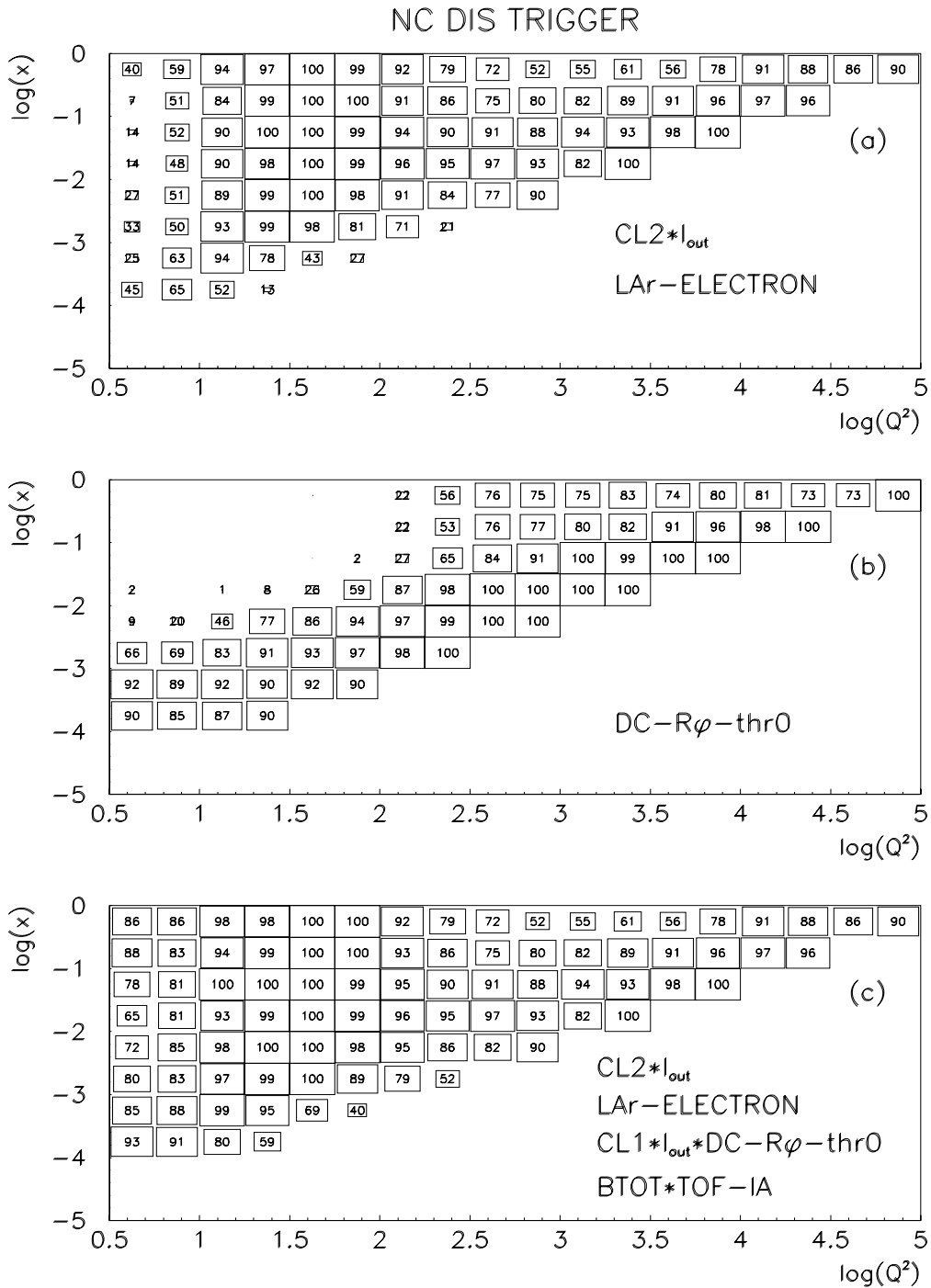


Figure 5.13: (a) Trigger acceptance of LAr electron trigger and BSET CL2 with innermost ring excluded from the cluster trigger. (b) Acceptance of central drift chamber trigger. (c) L1 trigger acceptance for combination of 4 subtriggers only.

## Chapter 6

# BSET Trigger - Hardware Realisation

## 6.1 Trigger Elements and Algorithm

The basic idea of the BSET trigger [53] is to look for well localized high energy depositions in the BEMC stacks. Groups of stacks with signals above preset thresholds are called clusters.

Cluster recognition is performed in a few steps. For this purpose the analog sums of EM channels from the same stack (*stack energy*) are used as primary trigger elements (*TE*) for the BSET trigger electronics. On the first level of pattern recognition the *cluster* is formed from up to  $2 \times 2$  adjacent TE's (Fig. 6.1a). For each stack a set of 2 thresholds is defined. The programmable hardware of the BSET allows to require up to four conditions (C1-C4) to be fulfilled by the accepted event.

The BEMC subtrigger elements are then sent to the H1 central trigger logic, which can select any of these elements and combine them to form final H1 first level subtriggers.

**C1: Number of clusters in the low threshold plane** To recognize the number of clusters, the signals of the TE are compared in ATD modules (Amplitude and Time Discriminator) to the low threshold (LT). LT is set typically  $2 - 3 \sigma$  above noise level. The resulting pattern of the output signals above LT ( $L_{th}$ ) is then analyzed by the Cluster Identification Module (CIM) in three steps:

1. A search for a hit in the innermost 4 stacks is done. Each found hit together with the three adjacent stacks (if they have signal above threshold) is counted as one cluster. This information is recorded and the signals of those stacks are excluded from further analysis (Fig. 6.2).
2. The remaining pattern is analyzed using [X,Y] projections and memory look-up tables (LUT).
3. The resulting number of clusters is determined as a sum of those found in both previous steps.

The first step of the cluster counting can be disabled by jumpers on the CIM module and the second and third step are fully programmable. This means that the cluster size in the X and Y projections is not hardwired but can be redefined by the software and one can require some topological criteria, e.g. to have clusters back-to-back in the azimuthal angle  $\phi$ .

**C2: Number of clusters in the high threshold plane** To recognize a candidate for an energy cluster, the stack energies are compared with the high thresholds (HT) in the ATD Modules. The stacks above HT, producing  $H_{th}$  signals, are the high energy cluster initiators ("seeds") (Fig. 6.1b,c,d). The resulting pattern of the  $H_{th}$  output signals is analyzed by the second CIM module the same way as in the case of low thresholds.

Both CIM modules are programmable to produce "KEEP" signals for 16 different cases e.g.:

- only one cluster is detected,
- at least one cluster is detected,
- at least two clusters are detected,
- more than two clusters are detected, etc.

**C3: Cluster energy sums** If at least 1 high energy cluster is found in the step C2, the cluster energy  $E_{cl}$  is determined.

If the stacks (TE) surrounding the "seed" (stack above HT) have signals above LT their energies are summed up (Fig. 6.1b,c,d). This sum is the cluster energy. Proper TE are selected by the Cluster Separation Module (CSM) and their signals are summed up in the Cluster Energy Modules (CEM).

In the case that more than 1 cluster was found one cannot assign to each cluster its energy and cluster energy is the energy sum of all clusters found (Fig. 6.1).

In the Energy Comparator and Timing Module (ECTM) three thresholds for cluster energies  $E_{cl}$  are implemented. These thresholds are used for independent down-scaling for different kinematic regions or in combinations with triggers from other subdetectors.

**C4: BEMC total energy** The total energy deposited in the BEMC  $E_{tot}$  is the sum of all stack energies above LT. The TE are summed in the CEM module and compared to the threshold level in the ECTM module. There is one threshold for the total energy deposited in the BEMC.

## 6.2 BSET Hardware

The BSET electronics is realized in 3 crates located in the H1 trailer. The analog electronics is located in 2 VME crates (VME mechanics and power supply distribution) and the digital electronics occupies one standard VME crate. The crates are located in the rack adjacent to the BEMC front-end electronics and are controlled by the dedicated BEMC OS-9 test station (TS) or by the main calorimeter processor. A schematic diagram of the BSET is shown in the (Fig. 6.3).

### 6.2.1 GAIN Card and ATD Module

Different stack types (quadrants, trapezoids and triangles) have different light collection properties. To achieve equal response from all stacks the signal weighting is needed. The trigger element analog signals from the stacks (88  $TE$ ) are equalized in the GAIN card and

### The BSET Trigger Clusters

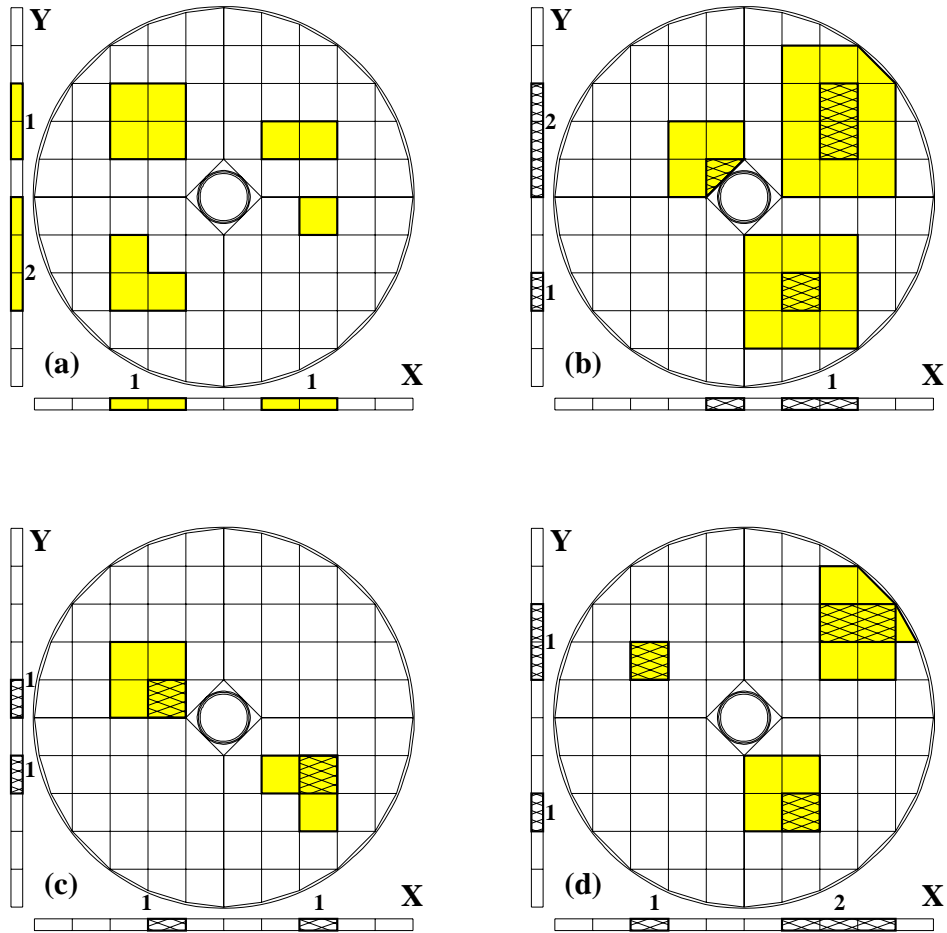


Figure 6.1: (a) Examples of possible cluster configurations and their numbers as found in the  $(X,Y)$  projections. Limited precision of the clusters counting with this method is shown - only 3 out of 4 clusters are identified. (b) Cluster seeds (above HT - hatched) and all stacks which can contribute (shaded) to the cluster sum if they are above LT. (c), (d) Typical examples of the cluster form and size.

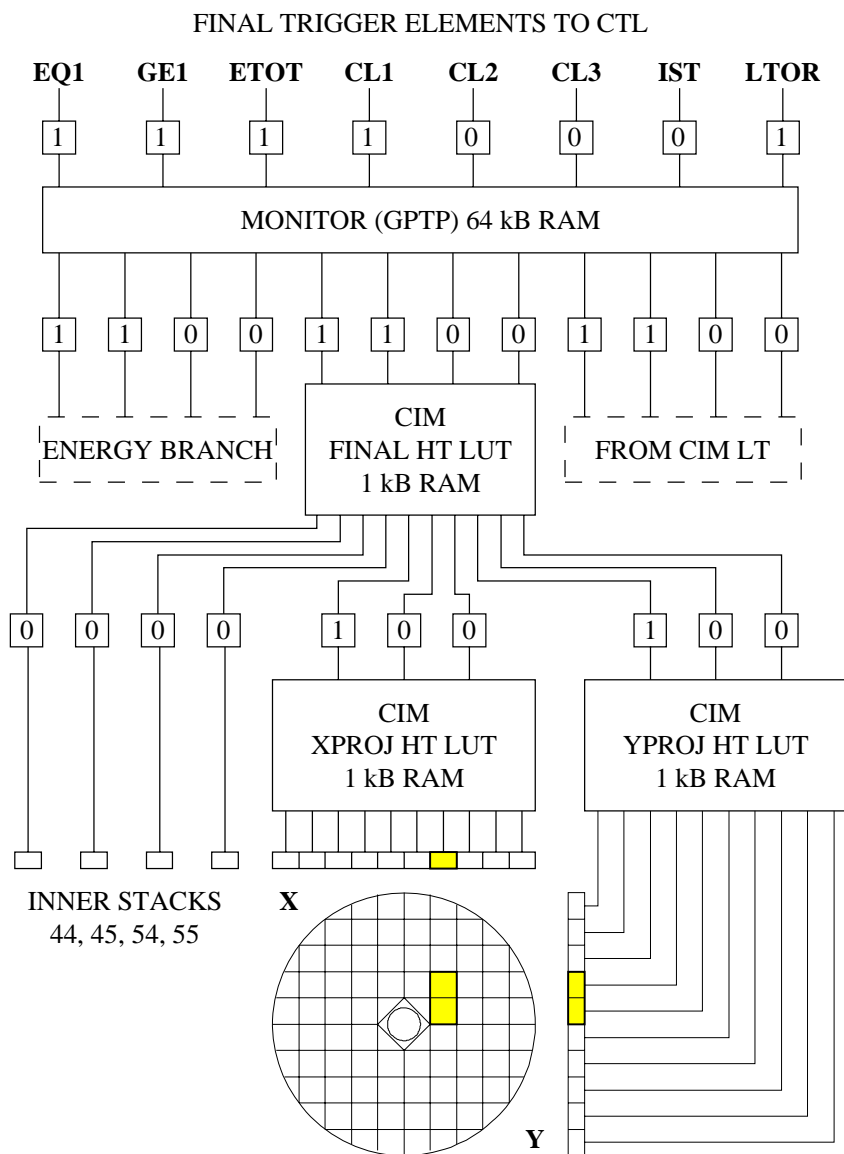


Figure 6.2: Final BSET trigger elements production starting from the  $(X, Y)$  projections with following pattern recognition in the look-up tables (LUT). For simplicity reasons only high threshold (HT) path is shown - LT branch is completely analogical. In parallel analog energy branch produces energy sum bits (BTOT, CL1, CL2, CL3).

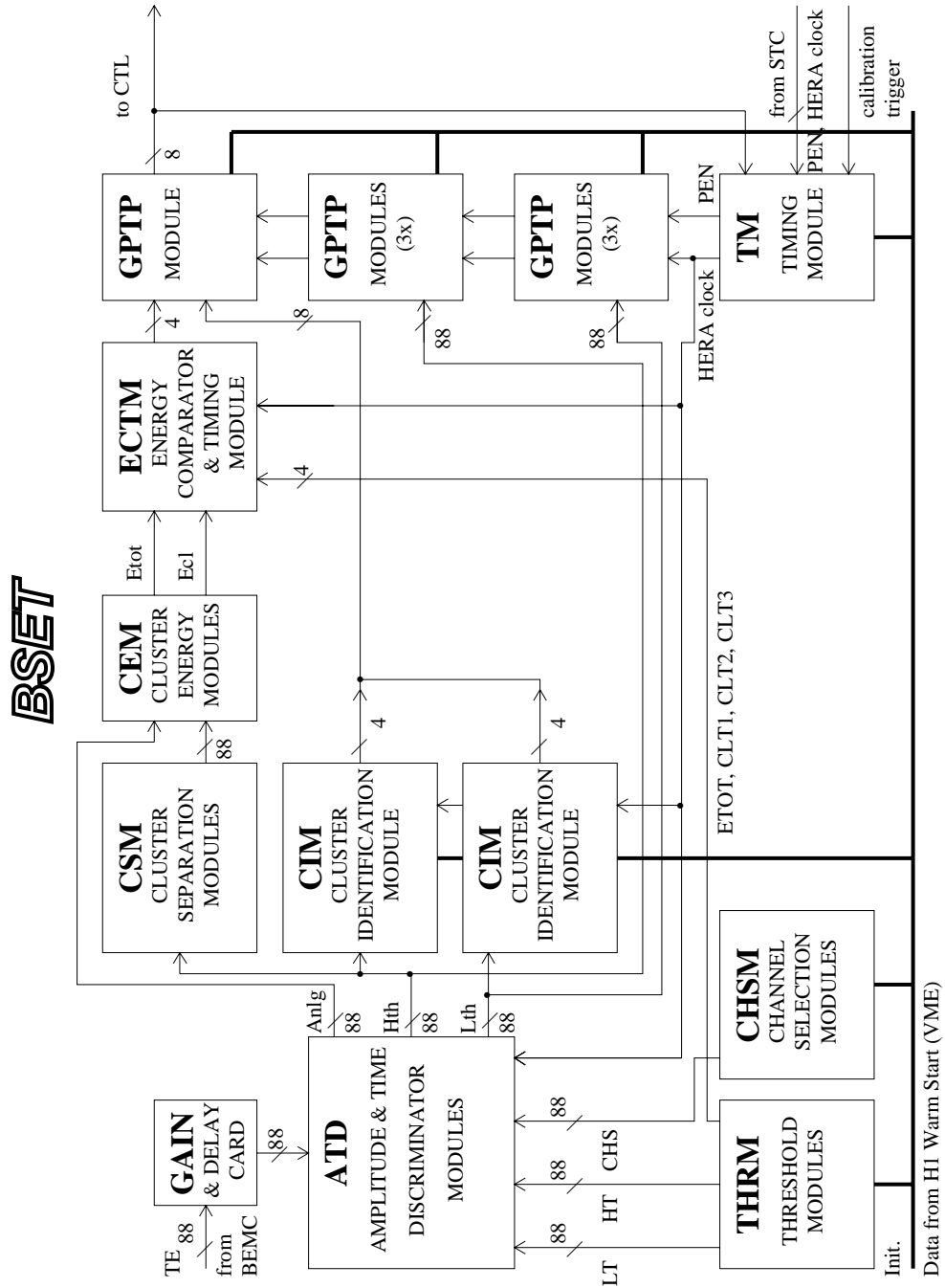


Figure 6.3: BSET trigger block diagram

are sent through mother boards to the analog Amplitude and Time Discriminator (ATD) module. The GAIN card contains also delay lines which allow time response equalization of all stacks.

There are 11 ATD-mother boards each with 8 ATD modules. The block diagram of the ATD module is in Fig. 6.4.

The stack energy signals are further processed in the ATD shaper. The ATD shaper is divided into three parts (Fig. 6.4).

The edge extractor sums the direct analog signal coming from the detector with the same inverted and delayed one. The delay of 120 ns ensures that the leading edge of the input signal is preserved on the output of this edge extractor. The falling edge of the output signal is 300 ns long.

This signal is afterwards differentiated and a bipolar pulse is created. Peak in the output signal from the edge extractor, corresponding to the  $t_0$ , is determined by the zero crossing detector.

The output signal of the differentiator is again integrated to get good energy resolution.

Finally, if a  $t_0$  is detected, the output analog signal is gated with this  $t_0$  for one bunch crossing period. The next HERA clock resets the  $t_0$ .

Each channel amplitude is compared to the 2 thresholds (LT and HT) and can be disabled for the case of hardware failures. Typical thresholds presently foreseen for the trigger operation are  $LT = 0.8 - 1.3 \text{ GeV}$  and  $HT = 3 - 15 \text{ GeV}$ .

Short summary of the ATD module output signals:

1.  $L_{th}$  - digital signal, synchronized with HERA clock, indicating that the shaped analog signal from the stack is above low threshold (noise threshold). This signal is related to the peak position of the shaped signal (stack low threshold  $t_0$ ).
2.  $H_{th}$  - digital signal with the same meaning as  $L_{th}$ , but for high threshold.
3.  $A_{nlg}$  - analog signal gated by  $L_{th}$  - input into the energy summing part.

### 6.2.2 CHSM and THRM Modules

The channel selection module (CHSM) gives a possibility to disable or enable the  $L_{th}$ ,  $H_{th}$  and  $A_{nlg}$  signals simultaneously for each of 88 BEMC's stacks. This is done by setting appropriate bits in the 11 8-bit registers. An additional (12th) register is used to define 8 control signals for the Timing Module (TM) (see section 6.2.5).

The task of the 4 Threshold Modules (THRM) is to set 2 thresholds for each stack, 3 thresholds for cluster energy and 1 threshold for the total BEMC energy. Each THRM contains 48 8-bit DAC's for threshold setting. For threshold verification 48 ADC's are used.

### 6.2.3 CIM Module

The CIM (Cluster Identification Module) identifies energy clusters in the BEMC. The identification is done in both ( $L_{th}$ ,  $H_{th}$ ) BEMC threshold planes, i.e. in 2 CIM modules.

An energy cluster is defined as pattern of one or up to four ( $2 \times 2$ ) adjacent TE elements with signals over threshold (Fig. 6.1a).

The implementation of the cluster identification algorithm in the CIM module is shown on the Fig. 6.2.

The cluster recognition itself is based on the projections onto 2 orthogonal axes [X,Y]. This means that the search for stacks with  $H_{th}(L_{th})$  signals is done in rows and columns. If at least 1 such stack in the row (column) is found the proper projection bit is set. Each of the [X,Y] projection patterns is written into the corresponding 10 bits (Fig. 6.2). The resulting projected pattern is evaluated by the programmable look-up tables. In these tables parameters as e.g.: cluster size, number of clusters and topological criteria are encoded.

The output from these tables is coded into 3 bits for each projection.

The innermost 4 stacks are treated separately (see 3.C1) and the corresponding bits together with  $2 \times 3$  bits from [X,Y] analysis are sent into the next LUT. Here this 10 bit information is summarized and the final result - 4 bits from one CIM module entering the monitor LUT are produced.

#### 6.2.4 CSM, CEM and ECTM Modules

The CSM (Cluster Separation Module) produces digital signals enabling a contribution of analog  $A_{nlg}$  stack signals to the cluster sum. The CEM (Cluster Energy Module) is a summing amplifier, which produces the particular sum for the total BEMC energy  $E_{tot}$  and the particular sum for cluster energy sums  $E_{cl}$ .

The ECTM (Energy Comparator and Timing Module) switches trigger bits on if the energies fulfil the corresponding threshold conditions. On the output the following 4 trigger bits are produced:

- 1 bit for the total energy deposit in BEMC  $E_{tot}$
- 3 bits for the cluster energies  $E_{cl1}$ ,  $E_{cl2}$ ,  $E_{cl3}$

The layouts of modules CSM, CEM and ECTM are shown on (Fig. 6.4).

#### 6.2.5 TM Module

The timing module (TM) is working as an interface for control signals between the BSET trigger electronics and the H1 central trigger logic (CTL). The TM module receives L1/L2 trigger control signals and HERA clock from the BEMC STC (Subsystem Trigger Controller) [54] fanout module and distributes them to the BSET hardware. It sets the appropriate delay for the HERA master clock, sets additional overrun delays and generates the local trigger signal. The following signals are used by the TM module to control different modes of BSET operation:

1. local or central mode
2. pipeline enable
3. trigger enable

4. random trigger
5. calibration trigger
6. - 8. after run (overrun) bits

For more details see section 6.3.

### 6.2.6 Monitor (GTP) Modules

The output patterns of ATD modules ( $2 \times 88$  bits -  $L_{th}$  resp.  $H_{th}$ ), the trigger conditions C1-C4 and the BSET subtrigger elements are stored for every bunch crossing in the General Purpose Trigger Pipe (GTP) cards designed in the H1 collaboration [55]. These cards provide storage for 32 bunch crossings (BC). The BSET history information is very useful for pile-up detection mainly in the BEMC readout chain but also for other subdetectors. It is also used for timing adjustment,  $t_0$  detection study, stability and integrity checking as well as calibration of the trigger electronics in the pipelined environment. This information is read out by H1 calorimeter readout branch and is available in the BSET BOS bank (all 32 BC or only 5 BC are read in the so-called extended resp. compact readout mode).

The resulting 8 BEMC subtrigger bits are provided for every bunch crossing ( $\Delta t = 96$ ns) via a programmable 64 Kbyte monitor look up table.

### 6.2.7 BSET Timing Characteristics

For proper synchronization of the BSET with the HERA clock and with other L1 triggers the knowledge of the BSET internal timing properties is needed.

An internal BSET decision time of 6 bunch crossings originates from the ATD and the CIM modules. The ATD modules need 3 BC to deliver the signals to the following CIM resp. CSM and CEM modules (see Fig. 6.3). The CIM decision is taken in another 3 BC. The parallel energy branch (CSM, CEM and ECTM) is faster and produces output signals after 1 BC already. To synchronize these two branches on the input into the GTP card the selectable delay switch in this card is set to 2 BC to delay the ECTM output bits.

The internal delay of the GTP card adds another 2 BC [55] resulting in the total BSET decision time of 8 BC. To be more precise the analog delays used to adjust the timing of the different stacks in the GAIN card (few tens of ns) should be added to the total decision time.

In the CTL logics the BSET trigger information is delayed by another 9 BC in order to be synchronized with all other triggers. This delay is determined by the slowest H1 trigger element entering the CTL (LAR trigger after  $2.1 \mu s$ ).

## 6.3 BSET Operation Modes

The BEMC electronics (readout and trigger) is an integral part of the H1 calorimeter readout branch. In such a large and complex system as H1 there is a need to have the possibility to test and tune the subsystem electronics independently. The BSET hardware is therefore designed to operate in three different modes :

1. Stand alone test mode

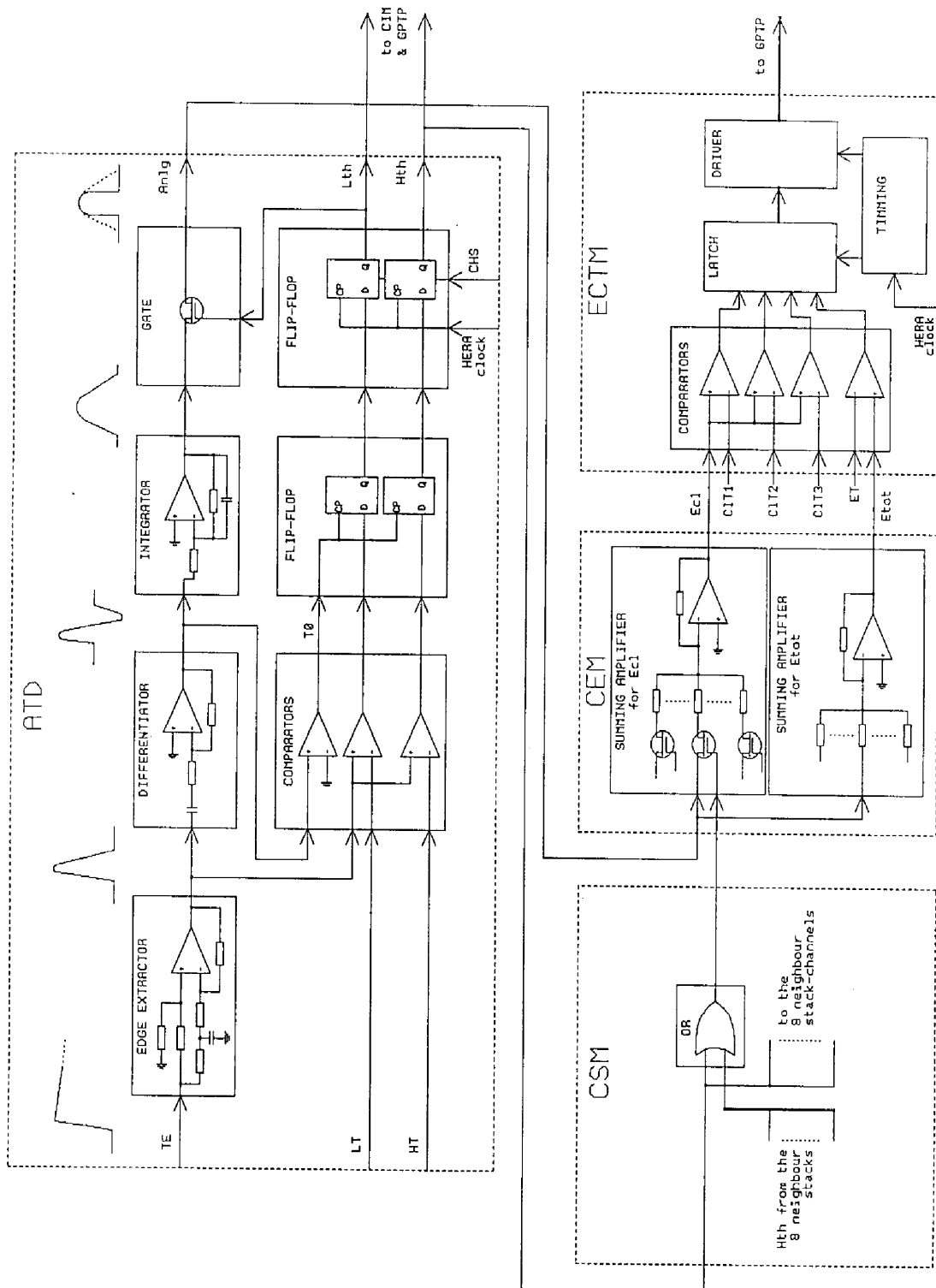


Figure 6.4: Block diagram of the ATD module

2. Stand alone  $e^-p$  mode
3. Standard data taking mode (central mode)

**Stand alone test mode** This mode allows to test, debug, tune and calibrate the BSET hardware completely independently. The BEMC test station sets up this mode (in TM module), chooses local trigger type and pulses the BEMC stacks with the BEMC calibration pulser [42].

The BSET provides three types of local triggers which are used for consistency checks of the whole trigger logic. They are called : *random*, *calibration* and *stand alone trigger*.

A *random trigger* is produced by the software of the control computer which stops the pipeline randomly. This trigger is used for pedestal and noise studies.

A *calibration trigger* is produced by the BEMC calibration pulser when the selected BEMC stacks are pulsed by a given DAC pulse height value. The calibration trigger is used for the gain, timing and threshold calibration of the trigger channels.

A *stand alone trigger* is one of the resulting 8 BSET subtrigger elements monitored locally. This bit is in the stand alone  $e^-p$  mode used as one of the local triggers. As the final subtrigger elements are produced via the fully programmable lookup tables, the stand alone trigger is used to test integrity and functionality of the whole BSET.

An activated local BSET trigger initiates the BEMC test station to read simultaneously data from the BEMC readout chain and from the trigger branch stored in the GPTP cards. Having both, trigger and readout chain data, together with three types of triggers provides powerful tools for testing, debugging and calibration of the trigger electronics.

**Stand alone  $e^-p$  mode** In this mode real data from the BEMC readout and BSET trigger are taken by the local BEMC test station using the stand alone BSET trigger or any trigger coming from the STC (H1 L1 trigger). The stand alone  $e^-p$  mode allows efficient tests of the BSET trigger response on real events.

Combining data from ADC and BSET chains allows optimal timing adjustment and thresholds calibration with real  $e^-p$  events.

**Standard data taking mode** In the standard data taking mode the local BEMC test station is not used and both branches (BSET and BEMC) of the readout electronics are controlled by the main calorimeter processor. In this mode the BSET trigger is regarded by the H1 central trigger logic as a standard triggering device. The BSET sends subtrigger elements to the CTL and through the STC receives H1 control signals.

## 6.4 Calibration and Timing Adjustment

### 6.4.1 Electronic Calibration of the Trigger

The goal of the calibration procedure is to find a function that converts the threshold settings to actual energy values in the corresponding BEMC stack. Energy in the BEMC stack is represented by the DAC pulse value of the calibration generator. To get one point of this function the following procedure is applied. For a given threshold (LT or HT) the stack is pulsed with different DAC levels in the region, where the transition in the

efficiency curve is expected. For each DAC value a given number of pulses is generated and the efficiency is then represented by the fraction of events for which the signal above threshold (in the right time slice) was detected. Differentiation of the efficiency curve gives a peak position at the threshold value.

The points obtained from this procedure are fitted by a linear function and the fit parameters  $p_1(\textit{gain})$  and  $p_2(\textit{pedestal})$  are plotted versus channel number. The same calibration procedure is done for low and high thresholds. The final results are used for thresholds setting of different classes of physics events to be triggered.

### 6.4.2 Timing Adjustment Procedure

In the collider type (pipeline mode) of the trigger electronics there are two basic timing related problems:

- adjusting of all subtrigger elements from the specific detector to the same bunch crossing
- setting the optimal delay for the main accelerator clock and the clock used in the trigger electronics

Thus the timing adjustment procedure has two major steps.

In *the first step* the calibration generator is used to find the BSET channel timing spread and the individual delay for each of BSET channel is determined. From the  $t_0$  distribution for one BSET channel we can see that some of the  $t_0$  values are found in the wrong BC. For each channel the efficiency of signal detection in the right BC for different time delays is computed. Scanning in 5 ns steps in the range of 2-3 BC's around the assumed  $t_0$  position provides the optimal time delay at which the full efficiency is achieved. This procedure can be done individually for each channel or for all channels simultaneously. The distribution width of measured delays must fit into the 1 BC time interval.

The task of *the second step* of the timing adjustment procedure is to find the optimal delay between the HERA clock (from the STC) synchronizing the BSET hardware and the BSET trigger bits position inside the right BC found in the previous step. Here one must take into account the energy dependence of the signal's timing position. This is very important in order to cover the whole dynamic range of the real physics signals.

## Chapter 7

# BSET Trigger Performance

## 7.1 Introduction

The trigger efficiency for a given physics process is the goal of each trigger performance study. But before obtaining the final number a lot of technical checks connected with the whole data acquisition process has to be done. Therefore we divided our analysis into two steps:

- **trigger technical performance**

- Performance of the individual stacks which are the basic trigger elements - most important is timing of each individual channel (see previous Chapter, page 82). We must ensure that for the whole dynamic range the stack response will be always in the same BC. Noise levels should be known and the low thresholds (LT) should be set to  $3 - 4 \sigma$  above the noise (noise thresholds).
- verification of the encoded logic
- verification of the summing part

- **trigger physics efficiency**

- threshold determination in a GeV energy units for all trigger elements
- efficiency calculation for certain class of physics events

Almost all these checks are in principle based on the *comparison* of the *reconstructed energy* from the analog read-out chain with the *trigger response* to these signals.

Another possibility is to find some *independent physics triggers* suitable for *crosschecking* the performance of our triggers. In our case the tracker triggers as e.g. BPC, ZVTX, TOF or DC- $r\phi$ , are used.

In the experiment a set of the so-called *monitor triggers* is defined, used to monitor the performance of the corresponding *physics triggers* and supposed to represent a very small fraction of the all collected data.

### 7.1.1 Trigger - Reconstructed Energy Correlations

Before calculating the BSET efficiency, we want to stress that we distinguish two classes of energies, when talking about the trigger efficiencies:

1. **trigger energy** - energy seen by the BSET trigger;
  - *trigger cluster energy* - i.e. energy sum from the stacks above the low threshold adjacent to the stack above high threshold (trigger cluster initiator)

- *trigger total energy* - energy sum from all BEMC stacks, which are above low thresholds
2. **reconstructed energy** - energy from off-line reconstruction
- *leading cluster* - cluster with maximal energy from all reconstructed clusters
  - *total cluster, total energy* - sum of all reconstructed clusters [56], equivalent to the total reconstructed energy

The fact that the clustering algorithms are slightly different in the trigger and in the reconstruction, that a trigger cluster requires at least one stack above high threshold ( $\sim 3 \text{ GeV}$ ) and to the trigger cluster sum contribute only stacks above low threshold ( $\sim 1.3 \text{ GeV}$ ), the trigger and reconstructed cluster energies could be significantly different (Fig. 7.1). Also total energies from reconstruction and seen by the trigger are different due to the low threshold condition for trigger total energy.

### 7.1.2 Thresholds and Efficiency Functions Evaluation

The calibrated thresholds and the trigger efficiency as a function of the deposited energy are obtained from the following general procedure:

- the reconstructed energy for the given channel (stack) or variable (cluster, total energy) is accumulated with sufficiently high event statistics into two histograms; into the first one enters all events and into the second one only those triggered by the studied trigger
- the trigger efficiency as a function of energy is obtained by dividing these histograms
- the resulting histogram is fitted with the modified 3-parameter Fermi-Dirac distribution function:

$$\epsilon(E_i) = \frac{P_3}{\exp \frac{P_1 - E_i}{P_2} + 1} [\%] \quad (7.1)$$

Parameter  $P_1$  is the threshold value, defined as the energy at which trigger efficiency reaches 50%. Parameter  $P_2$  describes the width of the transition region (threshold width) and at  $\pm 3 \cdot P_2$  the efficiency reaches 95 % resp. 5 %. The third parameter  $P_3$  fits the maximal achieved efficiency.

In the trigger efficiency histogram three regions, with different efficiencies can be distinguished:

1. *inefficient region* - energy is far below the set threshold
2. *threshold region* - energy is around the threshold and efficiency is rising from zero to its maximal value
3. *efficiency plateau* - efficiency is almost constant and for good triggers very close to 100%

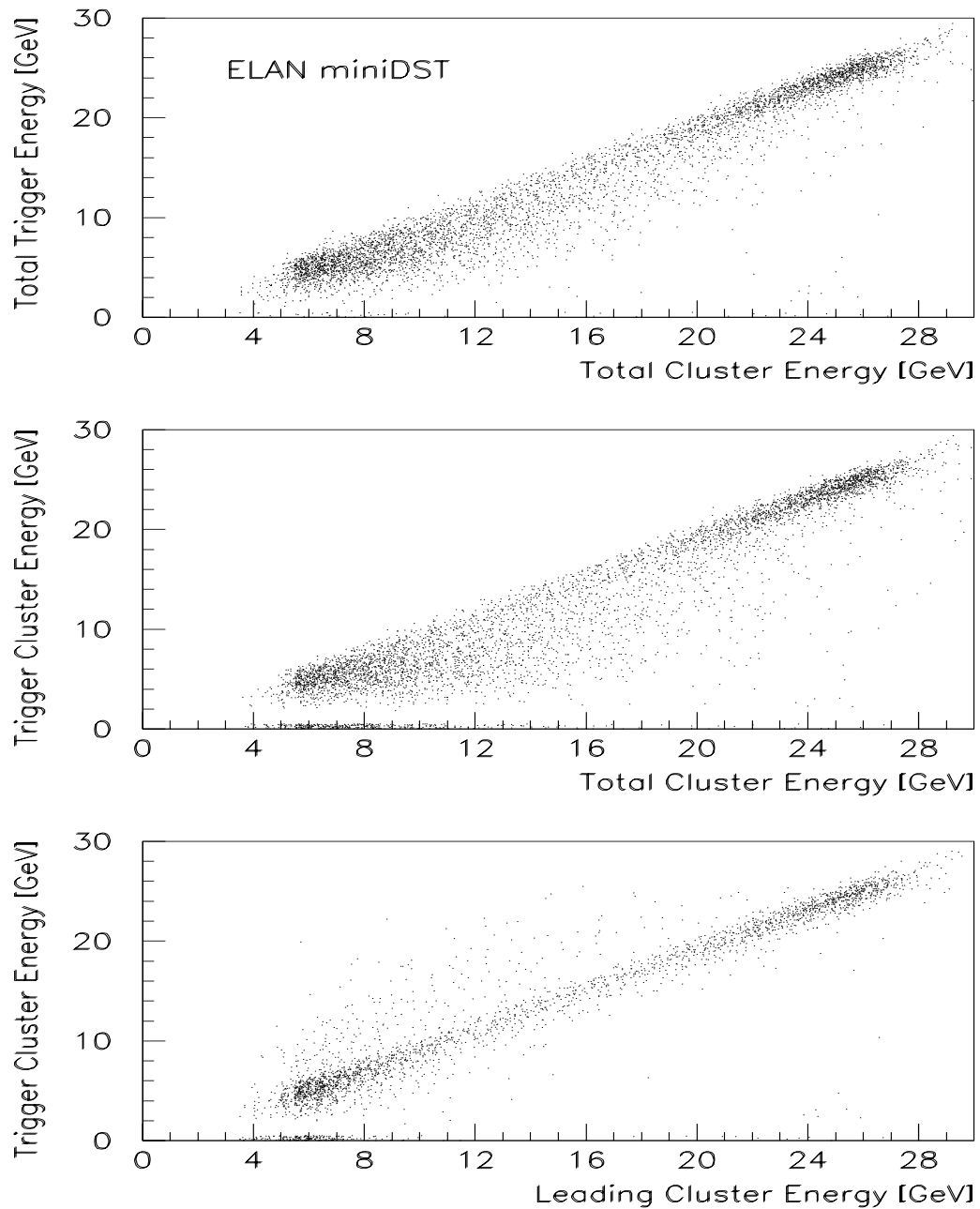


Figure 7.1: *Correlations between energies seen by the trigger and from the reconstruction.*

## 7.2 Technical Performance

### 7.2.1 On-line Monitoring of the BSET Triggers

Each trigger has to be checked already on-line, during the data taking, in order to detect problems as soon as possible. Any inconsistencies in the trigger logic, dead and/or noisy channels could deteriorate the quality of the measured data. Off-line corrections at the physics analysis level are very often painful and difficult. The time and informations available for on-line monitor task are usually rather limited, but nevertheless monitoring significantly improves the measured data quality.

Monitoring can be done on each of the H1 trigger levels L1-L4. As already mentioned, in the first period of the data taking only levels L1 and L4 were used. The most elaborated on-line monitoring of the BSET trigger was done on the  $\mu$ VAX cluster by requesting events from the event builder (AMD29000 RISC processor) [57] via the calorimeter OS9 station. The available information, i.e. the time history of all BSET trigger elements and uncalibrated energies from each BEMC readout channel (diodes), was provided by the calorimetric Digital Signal Processor (DSP). At that time the information from the Central Trigger Logic (CTL) was not available on this stage. The missing L1 trigger results, i.e. the information which subtrigger initiated L1-keep complicates unambiguous identification of the potential problems. E.g. if some other trigger had timing problems and was activated earlier, at first glance this can be identified as some "malfunctioning" of our monitored trigger. But a more detailed analysis could reveal that the expected trigger bit is active 1 bunch crossing later, i.e. monitored trigger works correctly and the shift is due to other trigger which is out of the time. From the many of histograms written to monitor the BSET performance on the  $\mu$ VAX cluster the following ones proved to be the most useful:

- hit maps for each trigger element - this kind of histograms helped to identify 2 sorts of hardware problems: noisy and dead channels.

Noisy stacks were identified in the 2-dimensional scatter plot with stack number on the  $x$ -axis and the bunch crossing (BC) position on the  $y$ -axis. On the Fig. 7.2/53 is an example where the LT trigger bit of the stack 56 is very noisy and is always active. This fact is reflected also in the behaviour of the trigger elements using this information, namely in the number of low energy clusters (Fig. 7.2/55). The quiet behaviour of stack high thresholds is shown on the Fig. 7.2/54. HTs are without the noise signals outside the nominal BC position.

Identification of dead channels was done by selecting stacks with energy deposit (from DAQ branch) safely above the HT and checking if also the corresponding stack threshold trigger bit has fired.

- cluster and total energy thresholds
- stack energy thresholds (LT, HT)
- relative rates of different trigger elements - they served mainly as a logic consistency check, e.g. comparison of rates from three cluster thresholds  $CL1 < CL2 < CL3$  (Fig. 7.2/5), or the occurrence of trigger elements EQ1 (1 high energy cluster) or GE1 (at least 1 high energy cluster found)

- number of hit stacks above LT and/or HT thresholds (Fig. 7.2/6,7)

### 7.2.2 Stack Performance Check

The basic ingredient of each BSET trigger element is the BEMC stack. Therefore we have to know and understand the performance of each stack. When studying the occurrence of low and high threshold (LT, HT) bits of individual stacks two types of inefficiency can be identified:

- LT(HT) bit is not set in the proper bunch crossing (BC) but in another one
  - this can be a sign of pileup, i.e. there can be a real signal at a different time, in another BC
  - this can be also timing problem of the trigger; when individual channels are not precisely adjusted in time, then too small or big signals can cause a shift towards the previous, resp. next BC
  - this can be a general trigger timing problem; if an event is triggered by a trigger which is not stable, then we can derive this "missing" information from our trigger
- the LT(HT) is not set in any of the recorded BC's, although the energy deposit is highly above the threshold
  - this is the case of hardware failure, reflected in the real stack trigger inefficiency and projected of course into the energy sums (total and cluster).

### 7.2.3 Logic Consistency Check

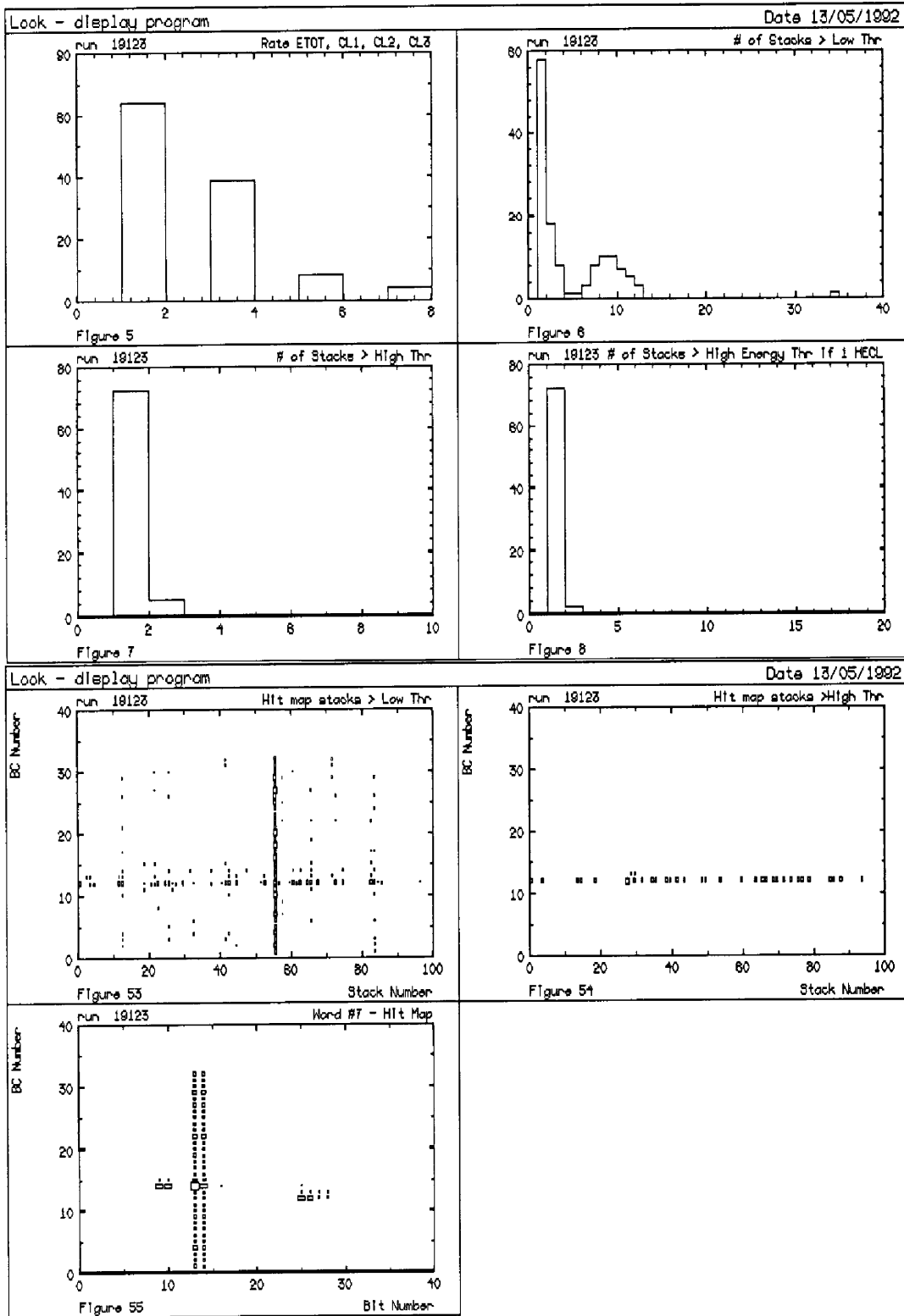
The logic consistency check in our case means testing the correctness of the trigger results and looking for events in which the active bits are in some logical contradiction. E.g. the rate of the trigger element *GE1* cannot be lower than that of *EQ1*.

Checks of the logic consistency are done already during on-line monitoring and in more detailed analysis off-line, where the status of the trigger bits is compared with the off-line reproduced trigger information. This is done by applying the same trigger algorithms, as are supposed to be loaded in the look-up tables, on the reconstructed energy deposits in the individual stacks. Very helpful, at revealing errors in the look-up tables, especially in the first phases of the data taking was the graphical software package H1ED - event display [58]. This tool enables a very detailed event scanning by eye, and confronts the trigger information with the energy deposits in the individual stacks.

### 7.2.4 Verification of the Summing Part

Verification of the performance of the CSM (Cluster Separation Module), CEM (Cluster Energy Module), and of the ECTM (Energy Comparator and Timing Module) is in principle done in the following steps:

- the fired HT and LT bits of the individual stacks in the nominal BC number are found



working ...

Figure 7.2: Examples of some on-line histograms monitoring the BSET trigger performance on the  $\mu$ VAX cluster.

- the energy from the data acquisition part for these stacks is taken and with the same algorithm as in the trigger logic the BEMC trigger total and cluster energy sums are created
- the response of the cluster (CL1, CL2, CL3) and of the total energy (BTOT) bits is checked
- the efficiency for these bits is calculated

Examples of efficiency curves for all our trigger energy sums from one period of the data taking, obtained by this verification procedure, are shown in Fig. 7.3. A characteristic feature of these curves is the narrow transition region, steep efficiency rise and 100% efficiency on the plateau above some threshold. The width of the threshold region depends on the relative precision of the individual stacks calibration, on the precision of each stack thresholds setting and finally on the number of stacks contributing to the trigger energy sum. The main physics trigger CL2 shows the typical behaviour as mentioned above. In the case of CL3 insufficient statistics prevents detailed studies. For CL1 the effect of events selection cut, requiring at least 2 GeV energy cluster in BEMC, is seen.

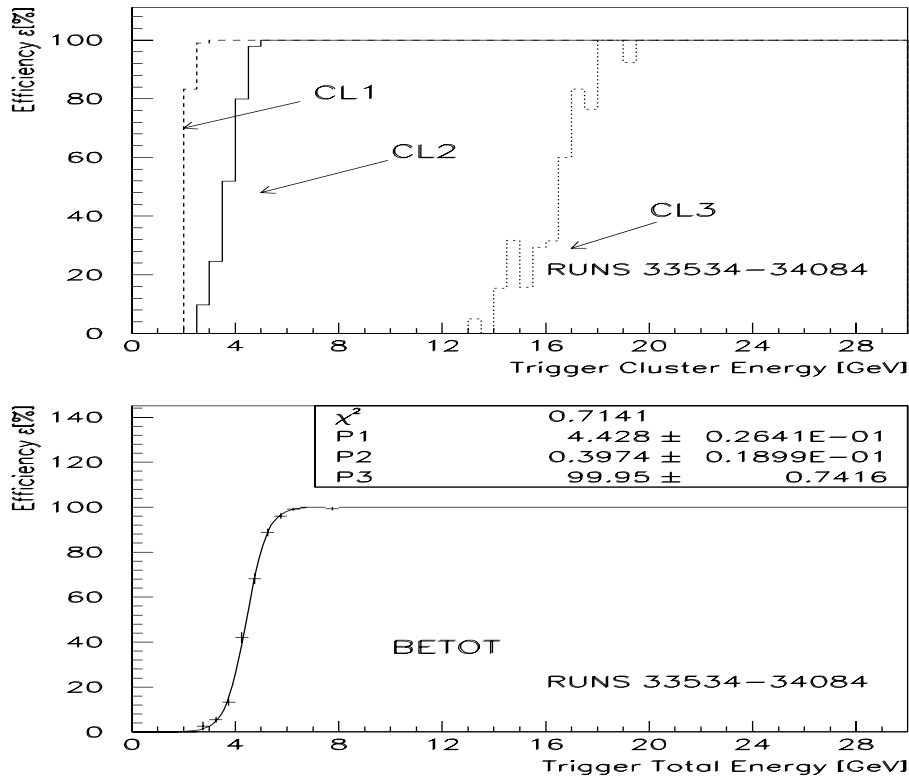


Figure 7.3: Trigger efficiencies for cluster energies seen by the trigger (a) and total BEMC trigger energy fitted with Fermi-Dirac function (b) 7.1.

## 7.3 Physics Trigger Efficiency

### 7.3.1 Stack Thresholds

Each stack is compared with two threshold levels as discussed earlier. The stack thresholds are independent of each other and different thresholds can be set for each stack. So e.g., for the stacks closest to the beam pipe higher thresholds should be set, compared to those located further from the beam line. This is one of the tools for handling high background rates, but of course it complicates final acceptance calculation.

**Low Thresholds (LT)** Low thresholds setting takes into account different noise levels of individual stacks and LTs are intentionally not the same. The differences between different stacks are seen from Fig. 7.5. The mean value over all stacks is  $1.3 \text{ GeV}$  (Fig. 7.6). The entries into this histograms were obtained for each individual stack from the standard efficiency calculation procedure (sec.7.1.2). The same result is obtained by application of the standard procedure on the sum of all stacks.

Extreme values at  $LT < 1.0 \text{ GeV}$  belong to the small triangles. They show better noise behaviour (only 3 diodes), therefore could be set so low. The LT were not changed during the whole autumn 1992 data taking period.

**High Thresholds (HT)** The HTs for all stacks were set to the equal DAC (Digital Analog Converter) values. The only exception were the innermost triangular stacks. Their HT were set to the maximal value of 255 DAC units ( $> 100 \text{ GeV}$ ), and this way they were excluded from the trigger as a potential cluster initiators.

Gradually as the performance of the HERA machine was improved and the background rates decreased, the HTs and energy sum thresholds were lowered. Four different HT settings are available and we can calibrate our stack trigger threshold values, given in DAC units, directly from the data. Thresholds for all stacks together are shown in the Fig. 7.4. Rather broad threshold regions indicate, that there are differences between individual stacks. The same DAC value does not ensure the same energy value. In the measured region we have observed a very good linearity and the calibration curve for the mean thresholds (average over all stacks) is fitted with a linear function:

$$HT(\text{GeV}) = (0.024 \pm 0.129) + (0.456 \pm 0.019) \times DAC \quad (7.2)$$

### 7.3.2 Total Energy Thresholds

To the total energy (*BTOT*) trigger element contribute all stacks with energies above LT. On the off-line reconstruction level a total BEMC energy is obtained from the sum of all reconstructed clusters and for this variable *BTOT* physics thresholds are estimated. During the 1992 period BSET total energy trigger was running at three different DAC values (10,15,24), what in terms of the total reconstructed energy means  $2.4 \pm 0.3$ ,  $3.9 \pm 0.3$ ,  $5.7 \pm 0.4 \text{ GeV}$  respectively.

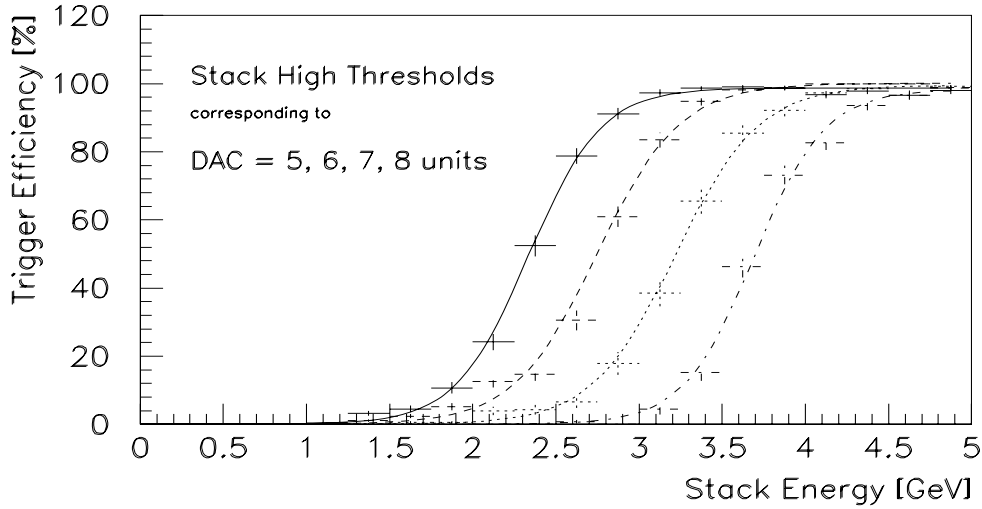


Figure 7.4: *Stack high thresholds corresponding to different DAC values*

### 7.3.3 Cluster Energy Thresholds

Cluster trigger thresholds (CL1, CL2, CL3) were changed more often, but not all values are usable for the calibration. Sometimes insufficient statistics is the reason, but mostly cluster threshold (mainly CL1) was very close to the HT (even below) and de facto determined by the stack high threshold. CL2 was used as a main physics NC DIS trigger, whereas CL3 was set as a kinematical peak trigger and monitor for the TOF performance. In principle seven different points, seven different DAC values are available for the cluster thresholds calibration. The  $GeV - DAC$  dependance was fitted with the function:

$$CLT(GeV) = (-1.68 \pm 0.04) + (0.36 \pm 0.003) \times DAC \quad (7.3)$$

### 7.3.4 Efficiency for the Low $Q^2$ NC DIS

When estimating trigger efficiency for certain class of physics events the first question we ask is:

- Does the trigger quantity correspond unambiguously to the physics variable (object) we rely in the analysis on?

In the case of affirmative answer on the first question, the trigger efficiency calculation can be relatively simple. In principle the trigger efficiency then depends on one variable. In the other case, the task starts to be more complicated and we have to take into account all specifications of the trigger definition and of the physics analysis. The trigger efficiency depends on more variables, which are correlated and its calculation then becomes a multi-dimensional task.

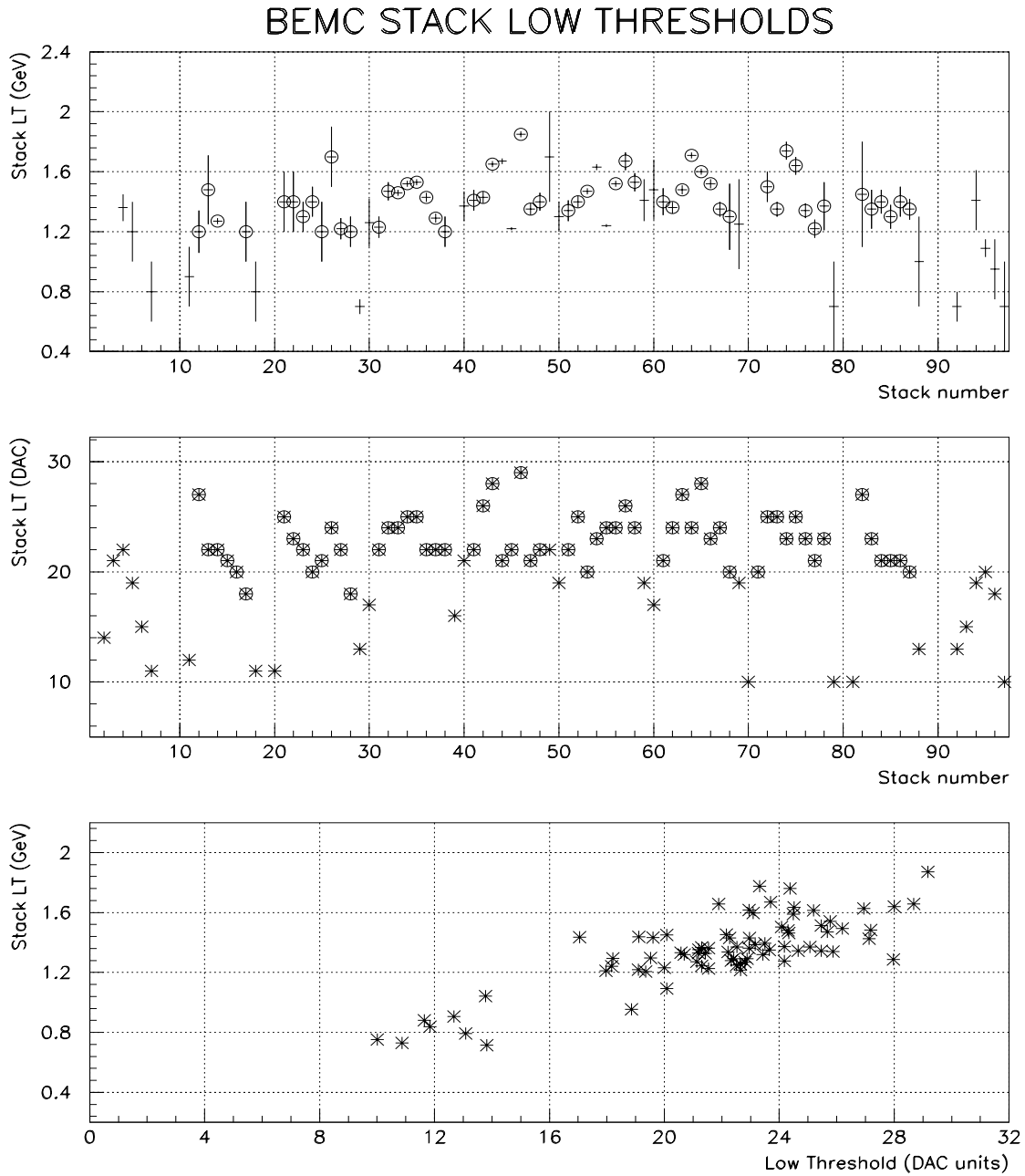


Figure 7.5: Stack low thresholds in GeV (a), in DAC units (b) and correlation between them (c). In (a), (b) the circles stand for the quadratic stacks, the rest are trapezoids and triangles.

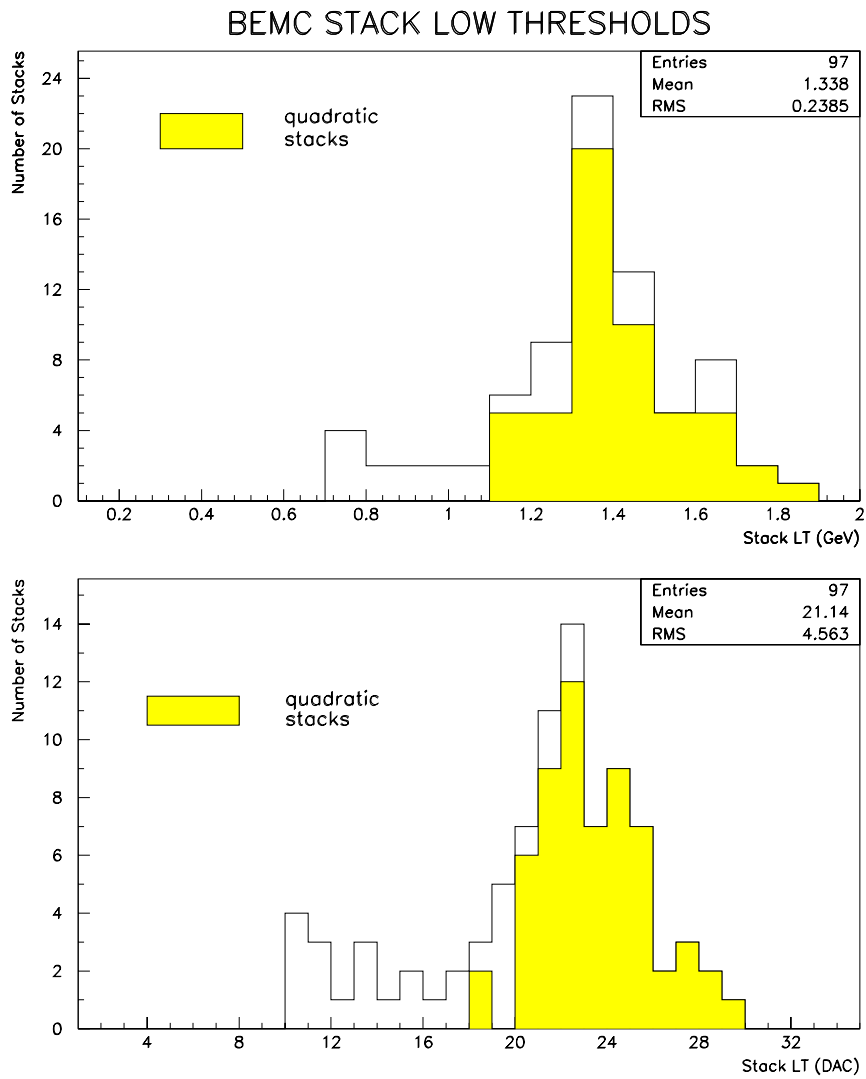


Figure 7.6: *Stack low thresholds distribution for all stacks in GeV (a), and in DAC units (b).*

It is important to note that the BSET trigger is not a truly inclusive electron trigger since in the case when more trigger clusters are found, the resulting trigger cluster energy is the total energy sum of all these clusters.

Therefore the determination of the trigger efficiency must be done on the total energy sum of all reconstructed clusters in the BEMC. But the physics analysis and event selection is done on the leading cluster energy, i.e. on the most energetic reconstructed cluster. The trigger efficiency for the final DIS sample must be estimated from the two dimensional distribution, on the scatter plot for the leading cluster energy and the total cluster energy (Fig. 7.7). This is valid mainly for low cluster energies where the influence of the event topology can be seen. For energies  $E_{CL} > 10 \text{ GeV}$  the 1-dimensional functional dependence on the leading cluster energy turns out to be a good approximation. If the hadrons accompanying the electron are emitted into the BEMC angular acceptance region, there is some chance that these hadrons will contribute to the trigger cluster energy and so enhance the trigger probability. But as already mentioned the BEMC is an electromagnetic calorimeter with a very poor hadronic energy measurement and the energy depositions from hadrons have large fluctuations. When estimating the trigger efficiency for the total reconstructed cluster energies we see a rather broad transition region (Fig. 7.7) and the full efficiency is achieved only for  $E > 15 \text{ GeV}$ . This can be explained when studying correlation between the leading cluster and the total cluster energy sum. Even if the total sum is above  $20 \text{ GeV}$ , there are events where the leading cluster has less than  $8 \text{ GeV}$ . Of course, this kind of events should be very carefully analysed. To have more than  $10 - 12 \text{ GeV}$  from hadrons in the BEMC is very improbable.

**Trigger Efficiency Crosscheck** Events triggered by other subtriggers (BPC, ZVTX, TOF-IA) and simultaneously with some energy deposit in the BEMC were used for the BSET performance crosschecking. The procedure is the same as described in sec.7.1.2 with one additional requirement, e.g. BPC trigger bit was active (Tabl. 7.2). The results are in good agreement with those obtained from the direct efficiency calculations. Only at low cluster energies the efficiency for events triggered simultaneously by tracker triggers is slightly smaller, but this difference is still within the statistical errors.

### 7.3.5 Monitor Triggers

Monitor triggers are usually triggers with very loose trigger conditions (low energy thresholds or any hit in tracker detectors) giving high rates and therefore they are prescaled. Subtriggers prescaling by a given number  $n$  is in hardware achieved by setting a counter to  $n$  and decrementing it with each triggered event. The prescaled trigger fires when the  $n$  counter has reached 0, which also resets the counter to  $n$  for the next cycle. BSET trigger elements EQ1 (1 high energy cluster) or GE1 (1 or more than 1 high energy cluster) monitor the performance of all cluster triggers. The cluster triggers with lower thresholds and without the TOF-VETO ( $\overline{TOF}$ ) requirement monitor the performance of those with higher thresholds. Trigger CL1 monitors the CL2 and CL3, resp. CL2 monitors CL3. Additionally the CL3 serves also as a monitor for very important TOF trigger. The fraction of good events from the CL3 triggers with a  $\overline{TOF}$  signal is used to estimate the number of lost  $e^-p$  collisions due to wrong TOF decisions. This found to be less than a few percent.

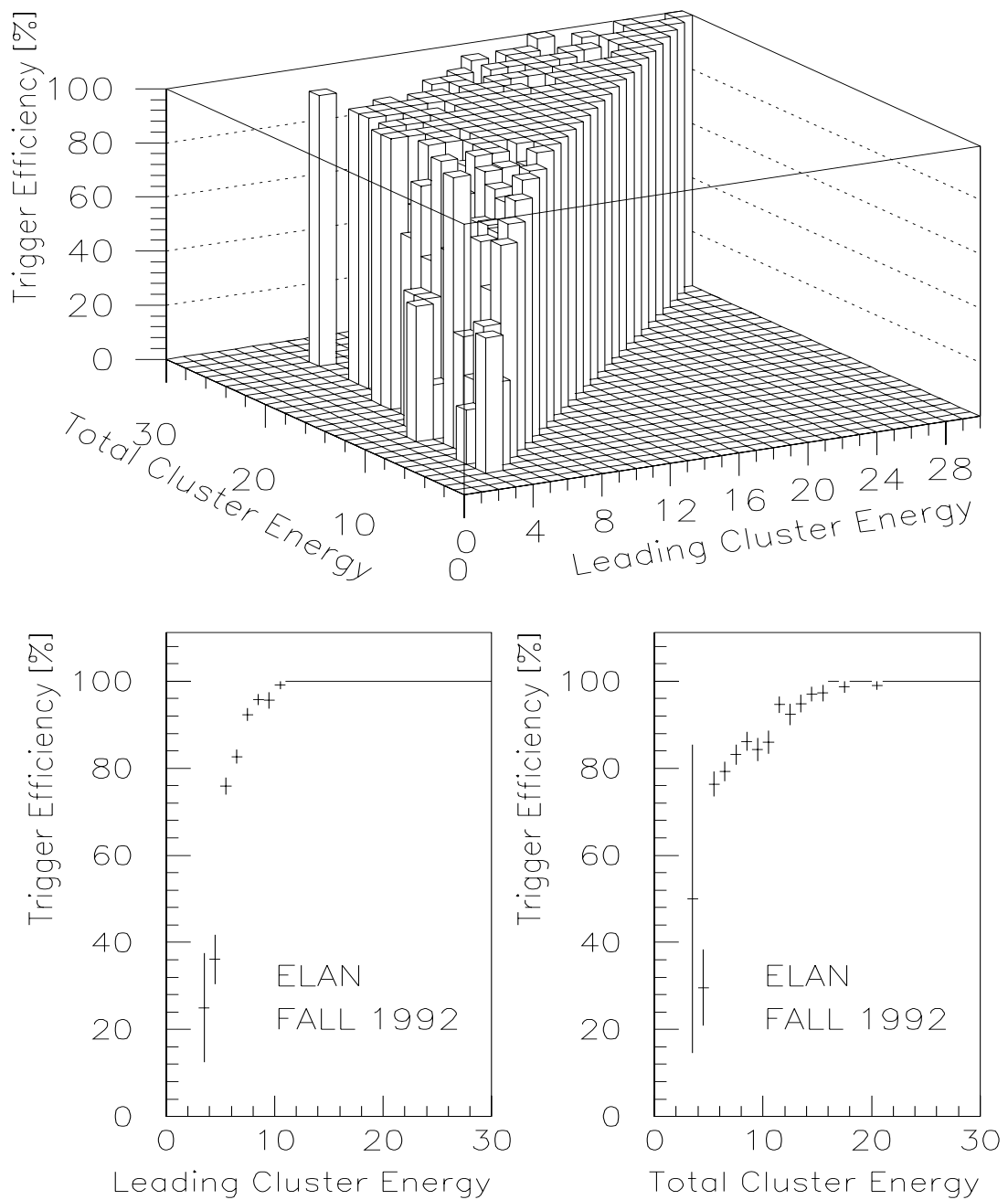


Figure 7.7: Two-dimensional dependance of the trigger efficiency (a) and projections onto both axis (b,c).

E(GeV)	Run #, corresponding HT; TCL2 (GeV)				
	all	< 32097	32097 – 32601	32602 – 34533	> 34533
	mixed	3.6; 3.5	3.2; 3.5	2.8; 3.5	2.3; 2.0
4 - 5	36.1± 5.7	23.1±11.7	25.0±21.7	18.2± 6.7	72.7± 9.5
5 - 6	75.9± 2.0	68.6± 4.3	64.6± 6.9	73.2± 3.1	95.0± 2.2
6 - 7	82.6± 1.6	74.8± 3.9	69.4± 5.9	84.8± 2.4	92.5± 2.3
7 - 8	92.3± 1.5	85.9± 3.9	85.7± 6.6	94.1± 1.9	98.5± 1.5
8 - 9	95.8± 1.3	89.8± 3.9	93.5± 4.4	99.0± 1.0	97.7± 2.3
9 -10	95.6± 1.9	91.2± 4.9	93.3± 6.4	97.8± 2.2	100.0
10 -11	99.1± 0.9	96.7± 3.3	100.0	100.0	100.0
11 -12	100.0	100.0	100.0	100.0	100.0

Table 7.1: CL2 trigger efficiencies for the leading cluster in the BEMC. Different run periods with different stack (HT) and cluster thresholds (TCL2).

E(GeV)	Run #, corresponding HT; TCL2 (GeV)				
	all	< 32097	32097 – 32601	32602 – 34533	> 34533
	mixed	3.6; 3.5	3.2; 3.5	2.8; 3.5	2.3; 2.0
4 - 5	34.8± 5.7	25.0±12.5	25.0±21.7	18.2± 6.7	70.0±10.2
5 - 6	75.8± 2.0	68.4± 4.3	64.6± 6.9	73.1± 3.2	95.0± 2.2
6 - 7	82.7± 1.6	74.6± 3.9	68.9± 5.9	85.4± 2.4	92.5± 2.3
7 - 8	92.3± 1.5	85.9± 3.9	85.7± 6.6	94.1± 1.9	98.5± 1.5
8 - 9	95.8± 1.3	89.8± 3.9	93.5± 4.4	99.0± 1.0	97.7± 2.3
9 -10	95.5± 2.0	90.9± 5.0	93.3± 6.4	97.7± 2.3	100.0
10 -11	99.0± 0.9	96.6± 3.4	100.0	100.0	100.0
11 -12	100.0	100.0	100.0	100.0	100.0

Table 7.2: CL2 trigger efficiencies for the leading cluster in the BEMC crosschecked by the BPC trigger. Different run periods with different stack (HT) and cluster thresholds (TCL2).

### 7.3.6 Pileup

Due to the high rates of background events, *pile-up* effects in the readout electronics chain (preamplifiers, line-drivers, shaper amplifiers) are expected. The pile-up is most critical in the shape amplifier, because this could lead to the wrong energy measurement. Unipolar shape amplifiers ( $FWHM = 500 \text{ ns}$ ) used in the BEMC analog electronics are sensitive to the pile-up effects in a time interval of  $1 \mu\text{s}$ , approximately 7 BC before and 3 BC's after the nominal BC [78].

The extended readout of the BSET trigger enables to write into the BSET bank data on the trigger bits status from 32 HERA bunch crossings. This readout mode was used only in the very beginning of the data taking and later was replaced by the compact readout mode, in which only 5 BC were written into the BSET bank. The compact readout mode is used in order to reduce the data volume and consequently DAQ dead-time in the calorimeter branch. The speed and the timing precision of the BSET allows to identify the pileup in the readout chain. In the trigger chain some of elements are fired not only in the nominal BC but also outside this position.

For the unambiguous identification of a pileup the information from another detector with a good time resolution and space correlation is needed. BPC and TOF detectors are potential candidates, but due to the fact that BPC detector information was spread out over 3 consecutive bunches, the unambiguous pileup detection was not possible with this detector. This is true mainly for LTs, called also noise threshold. If the stack above HT has fired outside the nominal BC, the probability is much higher that the reason was real pileup. The pileup probability is inversely proportional to the distance from the beam axis and the highest rate is expected in the innermost triangular stacks. However these stacks were excluded from the trigger as a potential cluster initiator (i.e. HT set practically to infinity) and therefore the fraction of events with an additional stack above HT outside the nominal BC position is very small. ( $< 1\%$ ).

When running at  $100\times$  higher beam currents pileup problems may become much more serious.

### 7.3.7 One Diode (1-D) Events

An unexpected type of background events triggered by BSET triggers was found in the data. Unphysical energy sharing between diodes of one stack is a typical signature for them. In these events the stack energy is concentrated only in 1 diode, all others together see only few percent of the stack energy! (Fig. 7.8a). To study this phenomenon we have defined a variable  $DR$  as a ratio of the energy seen by the hottest diode in the leading stack to the total stack energy. Cut  $DR > 0.95$ , later  $DR > 0.8$  was used for the rejection of these events on the L4 filter farm.

The radial dependence of the rates (Fig 7.8c) and the correlation with beam currents are a clear indications that source of 1-D events is directly related to the  $e^-p$  beams. Synchrotron radiated  $\gamma$  particles and particles from the proton induced background showers hit the diode directly and create the unphysical energy distribution with unknown energy scale. From all 1-D events more than 97 % have only one stack above  $HT$  (but remember that the innermost triangular stacks are excluded from the trigger!). To identify the source of these events the so-called  $p$ , resp.  $e^-$  pilot bunches, i.e. the bunches without its

corresponding counterparts, were used. For electron pilot bunch events  $\sim 70\%$  of the GE1 triggered events are of the 1-D type ( $DR > 0.8$ ), while from the proton pilot bunch for events not vetoed by the TOF, this number is only 30%. An empty detector with only 1 BEMC stack (1-diode) energy above  $HT$  is a typical signature for  $e^-$ -pilot bunch events, whereas from the proton pilot bunch events more BEMC stacks are hit with a typical signs of the proton induced background. In some cases beam halo  $\mu$  are seen and triggered by the muon and/or VETO WALL system.

About 70 – 90 % of all BSET triggered events rejected on L4 are 1-D events. It is however desirable to get rid of them already on some of the earlier trigger levels, preferably on the L1. The studies on the real data shows that the L1 or L3 trigger rates reduction by a factor  $\sim 5$  is achievable.

Using of single diode signals require major hardware changes (up to now the stack energy = sum of 4 diodes is the smallest available L1 trigger element), but the advantage would be the independence from the other detectors.

Another solution could be a requirement for BSET-BPC spatial correlation. For this purpose we have modified the reconstruction code the same way as in the simulation (see page 59). Matching of the BEMC stacks with the BPC strips and number of required matching BPC planes is defined by the look-up tables. Demanding 3 out of 4 planes (3/4) or 2/4 85 %, resp. 80 % of 1-D events could be recognized and vetoed already on L1 or L3 trigger level. The fact that so many 1-D hit stacks have no corresponding BPC hits indicates that these events are most probably related to the synchrotron radiation.

The solution of this problem becomes more urgent with the higher beam currents. Without significant increase of BSET thresholds the rate of CL2 trigger could be kept at a few Hz level, if 1-D events would be rejected already on L1.

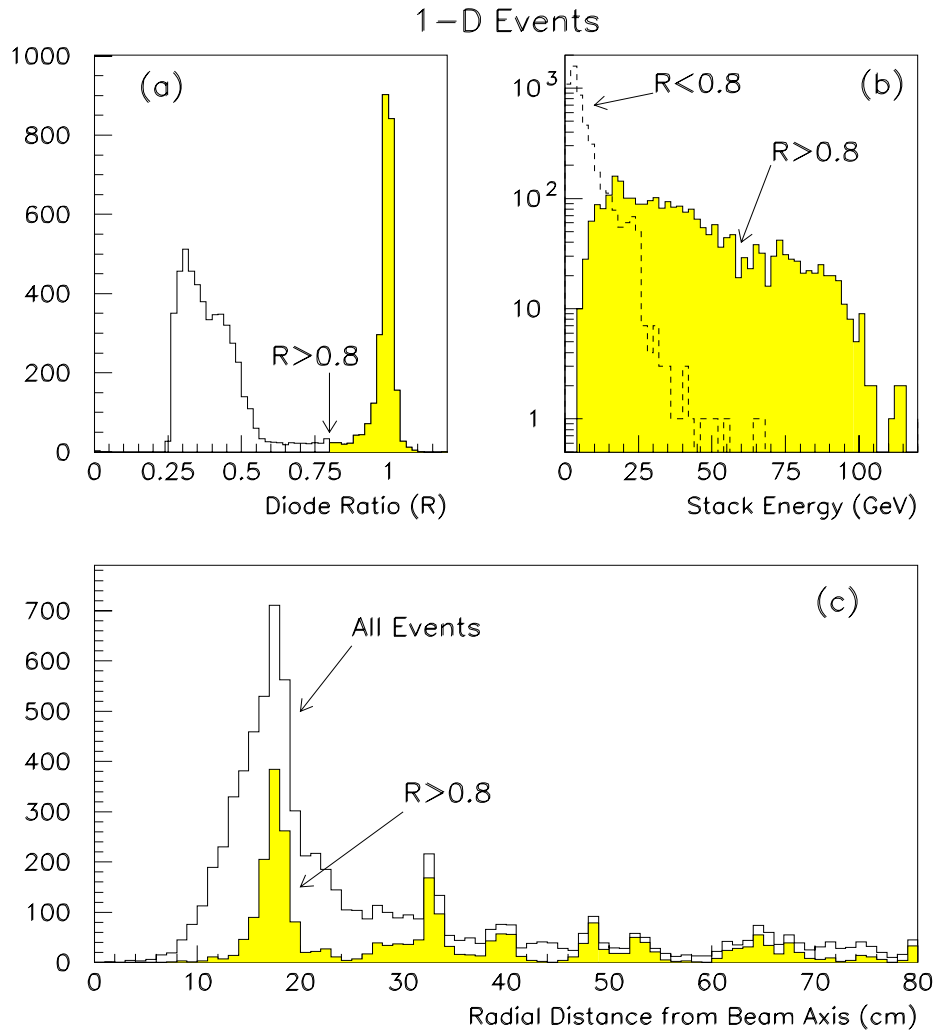


Figure 7.8: (a) Fraction of the energy seen by the hottest diode in the leading stack. (b) Energy spectra of both events classes. (c) Radial distance of the cluster center of gravity for all and for 1-D events.

## Chapter 8

# Measurement of NC DIS at Low $Q^2$

### 8.1 Standard Event Selection

The selection of deep inelastic scattering event candidates starts already on the trigger level. There we relied on the BSET cluster trigger CL2 in coincidence with TOF-veto ( $CL2 * \overline{TOF}$ ). The CL2 selects electron candidates in the BEMC and the TOF-veto, on the basis of time information, rejects dominating beam induced background events.

Most of 1992 the HERA machine operated in the  $10 + 10$  bunch mode at  $\sim 1\%$  of the design luminosity. Nevertheless the trigger rate was strongly dependent on the beam conditions and during the data taking period in the autumn 1992 the  $CL2 * \overline{TOF}$  rate varied between  $1 - 5$  Hz. Raw rates of the CL2 trigger element without TOF-veto were  $\sim 10 - 20\times$  higher.

The second step in the 1992 data events selection is done on the L4 trigger level where the software farm, by applying a set of different cuts using information from all subdetectors, acts as an effective filter. The reduction factor resulting from the two cuts provided by the TOF-veto and the L4 filter varies between  $\sim 40 - 100$  (Fig. 8.1). Most of the  $CL2 * \overline{TOF}$  triggers ( $> 80\%$ ) are on L4 recognized as 1 diode events (see previous chapter). This is the most serious, partially unexpected source of background events.

From all events which passed L1 and L4, i.e. not only those triggered by CL2, a further DIS selection is done off-line. All reconstructed events written on the production output tape (POT) are classified according to different event classes [64]. An event is classified as a NC DIS low  $Q^2$  candidate if at least one reconstructed energy cluster in the BEMC  $E_{BCLR} \geq 4$  GeV was found with a BPC hit in the cone of  $15$  cm around the reconstructed cluster center of gravity. A basic sample (called ELAN miniDST) which is used in the last analysis step contains  $\sim 8200$  NC events candidates and is selected according the following criteria:

- $E_{BCLR} \geq 6$  GeV
- for cluster energies between  $6 - 22$  GeV the existence of the central or forward vertex is required
- TOF cut - if there is at least one hit in the physical time window not more than 2 hits in the background window are allowed
- Beam pipe cut - center of gravity of the leading cluster is outside the innermost triangular stacks:  $|x_{cog}| > 14$  cm or  $|y_{cog}| > 14$  cm

For the final data selection procedure, providing 1019 NC DIS events with  $Q^2 < 100$  GeV<sup>2</sup> (Fig. 8.3a), some of the previous cuts were refined and also additional cuts were made:

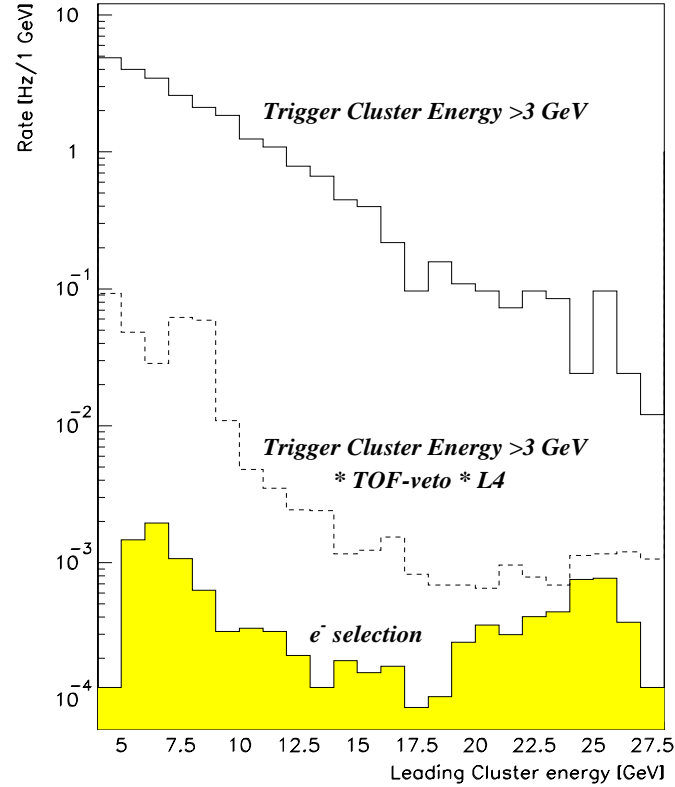


Figure 8.1: Absolute trigger rates in the BEMC as a function of leading cluster energy at different trigger and reconstruction levels.

- the spatial correlation between the BPC hit and the BEMC leading cluster center of gravity was refined from 15 *cm* to 5 *cm*
- the lateral size (radius) of the cluster was required to be < 5 *cm*
- the event had to be triggered by the BSET CL2 trigger
- the fraction of good tracks - events with large fraction (> 0.25) of tracks pointing outside the interaction region were rejected
- the vertex reconstructed from tracks in the central tracker was required to be within  $\pm 50$  *cm* from the nominal interaction point ( $z = 0$  *cm*)
- $0.05 < y_e < 0.6$ , cut for the analysis based on the electron measurement
- $y_h < 0.5$  cut for mixed analysis only (i.e. both electron and hadrons measurements were used)

The energy  $E_e$  and polar angle  $\theta_e$  spectra of the scattered electron used in the analysis are shown in the Fig. 8.2. The energy spectrum is before the cut on the cluster radius, which rejects mainly the  $\gamma p$  background at low energies. For the angular distribution an additional cut on the scattered electron energy  $E_e > 10.4 \text{ GeV}$  is applied. The shape and the position of the characteristic peak in the  $E_e$  distribution near the electron beam energy are only weakly dependent on the MC input structure function. This is used for the electron energy measurement calibration. The achieved precision of the absolute energy scale determination is about 3 %.

The MC events have been generated with the DJANGO 1.0 [65] generator which is an interface between HERACLES [66] and LEPTO [67] generators. HERACLES simulates electroweak interaction with included first order radiative corrections and LEPTO takes into account the QCD processes and parton fragmentation. MC distributions, based on the  $MRS D^-$  parton densities [68], are normalized to the integrated luminosity  $22.5 \text{ nb}^{-1}$  of the measured data sample.

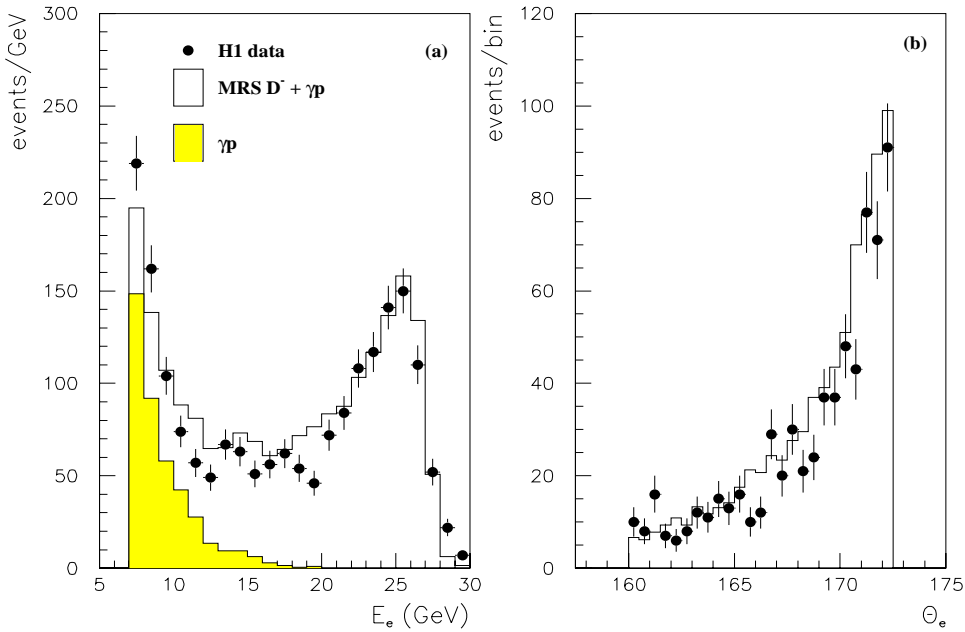


Figure 8.2: (a) Energy spectrum of the scattered electron before cut on the cluster radius. (b) The electron scattering angle spectrum after additional cuts on the lateral cluster size and on the electron energy  $E_e > 10.4 \text{ GeV}$ .

### 8.1.1 Background Subtraction

- **Physics Background** - the most important source of background to the NC DIS events, mainly at high  $y$  ( $y > 0.6$ ) is photoproduction ( $\gamma p$ ). For these events the

electron remains in the beam pipe and hadrons and photons produced can mimic a scattered electron in the BEMC.

The number of  $\gamma p$  events contaminating the NC DIS sample was determined from the combined analysis using the measured data and the Monte Carlo simulation. To generate hard and soft processes at  $Q^2 \sim 0$  the MC event generators PYTHIA [70] resp. RAYVDM [71] were used. The energy spectrum of fake electron candidates falls rapidly with increasing energy (Fig. 8.2). The cut on  $y < 0.6$ , equivalent to the cut on electron energy  $E_e > 10.4 \text{ GeV}$ , strongly reduces the remaining background in the studied sample. Another effective cut is the  $5 \text{ cm}$  cut on the radial size of the BEMC cluster. The photoproduction contamination was estimated to be less than 30 % at  $E_e = 10.4 \text{ GeV}$ . Below  $y \leq 0.4$  the  $\gamma p$  background can be neglected. The residual contamination of the measured  $x, Q^2$  bins was subtracted statistically.

- **Machine Background** - the fraction of events from beam related background surviving the event selection criteria was estimated from the proton and electron pilot bunch events. The upper limit of remaining beam induced background was estimated to be at most 1% in the whole kinematical region [36].

## 8.2 Discussion

The precise structure function measurement is not a simple task. It requires a very detailed understanding of all systematic errors which could have an impact on the final results. Some effects could be neglected in the first round of measurement when the total systematic errors are still at the 10 – 30 % level. The knowledge of the absolute energy scale and the energy resolution are the basic ingredients of this tedious process. The electron energy measurement in the BEMC can be affected by two effects which are not taken into account in the current procedure:

- the pileup events
- the events with 1-diode signature in any of the stacks contributing to the cluster energy sum

In this section we want to discuss these effects which could be important in the future when a better understanding of the whole detector will enable to decrease the overall systematic errors down to a few percent level.

- **Pileup Event Candidates** The HERA beam crossing rate of  $10.4 \text{ MHz}$  means that every  $96 \text{ ns}$  interactions can occur. As the BEMC readout electronics is much slower, the energy measurement can be deteriorated by the superposition of the signals belonging to the previous 7 or to the subsequent 3 bunch crossings [78]. The identification of these events is possible due to the very good time resolution of the BSET trigger and due to the fact that in the trigger readout the status of all trigger bits (including stacks LT, HT) before and after the triggered event is available.

In the leading cluster we were looking for the stacks which have their trigger information (low and/or high threshold bit) active outside the nominal BC position. Here we have found two types of events:

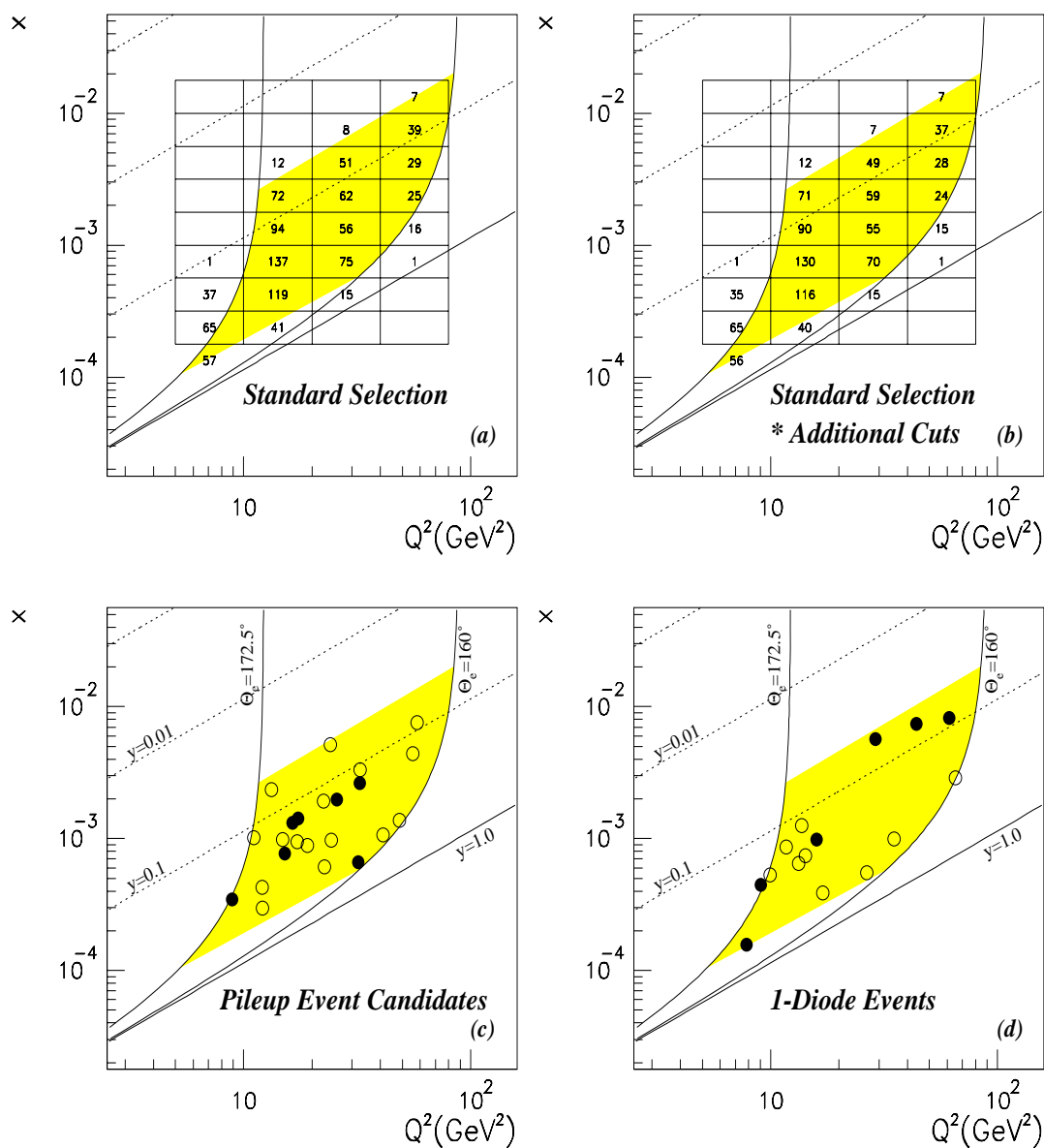


Figure 8.3: (a) Number of events in the defined bins after standard cuts applied on the preselected sample. (b) Number of events in the same bins after additional cuts, using the time history information of the BSET trigger bits (pileup candidates) and rejecting events in which any stack in the leading cluster had the 1-diode signature. The distribution of pileup event candidates (c) and of 1-diode events (d) in the measured region. With black dots are in both cases marked the events in which the affected stack contained more than 2 GeV.

- *primary pileup* - trigger bit is active in the nominal and also in some previous or later BC
- *secondary pileup* - the stack trigger bit is active only outside the nominal BC

The events with *primary pileup* should be removed from the final sample, because a proper correction of the measured energy is not possible in this case. For the *secondary pileup*, in the case that energy in the hit stack is not very big (thus the leakage into the adjacent stacks is small), one could try to leave out this stack from the cluster reconstruction algorithm.

In the ELAN miniDST from summer 1992 and in the final sample after standard selection we have found 3.0 % resp. 2.2 % events which are considered as pileup candidates. In most of these events the energy measured in the hit stack is close to the stack low threshold ( $\sim 1.3 \text{ GeV}$ ) and therefore they could be simply noise triggers, without any measurable effect. But in  $\sim 32 \%$  of these events the energy in the affected stacks is above  $2 \text{ GeV}$ . The residual fraction of the cluster energy  $E_{res} = 1 - (E_{clus} - E_{stack})/E_{clus}$ , which could be wrongly measured varied between  $\sim 5 - 15 \%$ . Unambiguous identification of the real pileup would be possible only with the help of the BPC and/or TOF detectors. Unfortunately the timing adjustment of the BPC, which is intrinsically very fast ( $\sim 50 \text{ ns}$ ), was not perfect and the needed information was spread in up to 3 BC. Almost all pileup event candidates are *secondary pileups* and only in 3 cases we can talk about the *primary pileup*. But in this case the affected stack contains rather big fraction of the cluster energy.

- **1-Diode Events** The so-called 1-D events causing the triggering problems were discussed in the previous Chapter 7 (page 97). Events with 1-D signature are normally rejected already on the L4 filter farm and later also in the standard analysis procedure. But in both these steps only the "hottest" stack in the leading cluster was tested. We have checked all stacks contributing with at least  $500 \text{ MeV}$  to the cluster energy sum and have found that in the ELAN miniDST still  $\sim 6.2 \%$  of 1-D events were present. In the final sample used for the  $F_2$  structure function measurement still  $\sim 1.5 \%$  of all events had the 1-D signature (Fig. 8.3 d). It means that for  $\sim 1.5 \%$  of events the cluster energy measurement could be deteriorated by the contribution from these stacks due to the unphysical energy sharing between the diodes. Although the considered stacks were non-leading ones, the effect on the final energy determination varied between  $\sim 5 - 10 \%$ , with indication of possible tails in the residual energy distribution (two events with 16 % resp. 33 %).
- **Conclusions** Detailed studies of the above mentioned effects have shown, that the fraction of good events affected by the "pileup" or by the existence of 1-D stacks in the leading cluster (Fig. 8.3) is of the order of  $< 4 \%$ . The impact on the 1992 data with rather big systematic errors (10 – 30 %) is negligible. But in the future at  $\sim 100 \times$  higher luminosity the pile-up probability and the fraction of 1-diode stacks in the BEMC electromagnetic cluster could be larger by factor  $\sim 5$ . With better understanding of all systematic effects and reducing them down to a few percent level, the size of the contribution from these two additional sources must be understood and correctly taken into account. Important prerequisite is the precise timing adjustment

of all involved detectors (BPC, TOF, BEMC), which are intrinsically very fast. The unambiguous detection of the proper bunch crossings must be achieved.

## Summary

- **BSET Trigger** A first level single electron trigger, using stack energy as a basic trigger element, has been designed and built for the H1 backward electromagnetic calorimeter. The trigger is capable to recognize cluster topologies and to set thresholds on the cluster and total energies. The trigger decisions can be uniquely assigned to the correct bunch crossing. The history around the nominal trigger position can be recorded via a digital pipeline.

The trigger was operated successfully at the first H1 data taking period at HERA and has been a major contributor for the collection of the NC DIS event sample.

- **NC DIS Triggers** Efficient trigger algorithms and various alternatives for triggering of the NC DIS events at  $Q^2 < 100 \text{ GeV}^2$  based on the H1 trigger simulation results were proposed and used during the data taking at H1. It is shown that in fact with a few subtriggers, as e.g. with the following ones, the whole kinematical region of interest could be effectively covered:

$CL2 * \overline{IST} * \overline{TOF}$	- low $Q^2$ , low $y$ trigger
$CL1 * \overline{IST} * DC - R\phi - thr0 * \overline{TOF}$	- low $Q^2$ , high $y$ trigger
$BTOT * TOF - IA * \overline{TOF}$	- low $Q^2$ , high $y$ trigger
$LAr - Electron * \overline{TOF}$	- high $Q^2$ trigger

- **Beam Wall, Beam Gas Background** The total background rates at H1 are lower by factor 2–5 [79] than the predicted ones. On the other hand in the BSET trigger is this partially compensated by the unexpected high rate of 1-diode events originating mainly from synchrotron radiation.

An algorithm to reject 1-diode events, based on the BPC - BEMC spatial matching, was proposed for the L3 resp. L1 trigger level. The advantage of this solution is that it does not require major hardware changes, but on the other side the rejection efficiency strongly depends on the performance of the BPC. A more reliable solution would be to use the diode signals directly on the L1. In this case major hardware changes are inevitable.

- **Calorimeter Triggers Performance**

**On-Line Monitoring** Software to monitor on-line the performance of the BSET and LAr calorimeter triggers was written and implemented on the calorimeter  $\mu VAX$  cluster.

**Off-Line Analysis** Methods to calculate the trigger efficiency of the BSET trigger for the NC DIS at low  $Q^2$  and techniques to crosscheck the performance of this trigger were elaborated. The cluster trigger worked very reliably and was fully efficient for the energies above 10  $GeV$ .

- **NC DIS Measurement at Low  $Q^2$**  On the top of standard ELAN cuts the additional ones, using more detailed trigger information and careful check of all stack energies contributing to the electron cluster, were applied. It was found that fraction of good events, i.e. those selected by the standard criteria, affected by the pileup or 1-diode stacks is of the order of a few percent ( $< 4\%$ ). These events can be left out from further analysis. When taking into account the achieved precision of the  $F_2$  structure function measurement ( $\sim 10 - 30\%$  systematic errors), this has a negligible impact on the 1992 data. But in the future at  $\sim 100 \times$  higher luminosity the pile-up probability and the fraction of 1-diode stacks in the leading BEMC electromagnetic cluster is expected to be  $\sim 5 \times$  larger. Therefore these effects must be carefully studied. In order to identify the pileup event the information from the BPC and/or TOF detectors has to be used. For this purpose the precise timing adjustment of the involved detectors must be done and the unambiguous detection of the proper bunch crossings must be achieved.
- **Low  $(x, Q^2)$  Physics at H1 in the Future** First measurements of  $F_2$  structure function at very low  $(x, Q^2)$  would not be possible without a dedicated very efficient electron trigger in the backward region of the H1 detector, without the BEMC calorimeter and without the backward proportional chamber (BPC). But in order to use the full potential of the HERA machine at *very low*  $(x, Q^2)$  further improvements in tracking, energy measurement and triggering in this region are needed. They are subject of the H1 upgrade program [83]. From the trigger point of view the improvements are needed in order to:
  - reduce the background rates
  - extend the acceptance in the  $\theta - y$  plane
  - provide a redundancy for the low  $Q^2$  trigger acceptance

## Appendix A

# The H1 Simulation Programs

## A.1 The H1SIM Package

The H1 detector simulation program H1SIM is based on two software packages widely used in the high energy physics community, namely: the GEANT3.13 system of the detector description and simulation of particles tracking through the detection media [80], and the BOS77 system for the dynamic memory management [81].

The whole physics of the particles interactions in the detectors (tracking in the electromagnetic field, cross sections, secondary particles generation, shower development) is in H1SIM simulated by the GEANT3.13, but the ZEBRA based I/O part of GEANT is replaced by BOS77.

The modular form of the H1SIM program [59] enables to process only some specific part of the H1SIM. Thus e.g. trigger studies can be done without redoing the time consuming GEANT or DIGI steps.

The H1SIM modular structure is built up from the following main modules:

- *H1GEA*
- *H1DIGI*
- *H1TRIG*

The *H1GEA* module is the main part of the simulation. H1 detector geometry is built in with many fine details resulting in a very realistic detector response ('close to real life'). The negative effect of this approach is a large CPU-time consumption. The input to the GEANT module are *generated events* (particle 4-vectors) and the output are so called *hit banks*, which contain the xyz-coordinates of entry and exit points of the particle trajectories for the sensitive detector parts in the tracking part and energy depositions for calorimeter type detectors.

For a given detector geometry a decisive factor influencing CPU-time consumption are cuts used for the tracking of all particles through the experimental setup. For each calorimetric medium one has to find the optimal cuts which allow correctly describe the fluctuations in the shower development (energy resolution). For the different tasks were in the H1 defined three sets of cuts. For the simulation of electromagnetic showers in the BEMC the medium set ( $CUTGAM = 0.2$ ,  $CUTELE = 1.0 \text{ MeV}$ ) of the standard H1 tracking cuts was found as a good compromise [77]. Finer cuts on kinetic energy of photons resp. electrons ( $CUTGAM = 0.05$ ,  $CUTELE = 0.1 \text{ MeV}$ ) give the same energy resolution as the medium ones but the time needed to process 1 event is almost 3 times longer (105 ns compared to 38 ns on the DESY IBM 3090-30S). The energy resolution for

the first set of cuts (0.2, 10 MeV) was found almost  $2\times$  worse than the measured one and therefore not suitable for the precise detector response simulations.

The *H1DIGI* module, which is also H1 specific and not the standard GEANT module, transforms the *hit banks* into the *digi banks*, which contain the detector response in a format similar to real events (channel numbers, wire addresses, ADC counts etc.).

Finally the *H1TRIG* module using the *digi banks* as input creates trigger response BOS banks and combines the single trigger elements into the final trigger decision the same way as it is done in the L1 hardware.

All steering options of the H1SIM detector simulation program are entered via the BOS text banks. The banks are read in from standard input at the beginning of the job. All steering banks are collected inside the text bank OSTX, which itself is contained in a normal textfile. Therefore the user can change any of the steering variables by using the local editor.

In addition to the steering banks there are a lot of *parameter banks*. Typical examples of *parameter banks* contain calibration constants, weighting functions, smearing and resolution parameters, trigger thresholds, noise values etc.

All the parameter banks are managed by the H1 database management system *MDB* [82].

### A.1.1 BSET Trigger Code in H1SIM

BSET trigger simulation is part of the *H1TRIG* module and the calling sequence is:

```

BCTRES
BCTRIG
    BTCLUS
        BTIDEN
            BTCLAD

```

**BCTRES** : In this module all thresholds and noise values from the text bank BTTX (BSTH resp. BTNS) are read in. Visible energy from the BRCE digi bank is converted to the real (calibrated) energy. Trigger banks BTTT and BTBT (LAr trigger part trigger towers, resp. big towers) and BTST trigger bank are created. BTST contains BEMC stack numbers and energy depositions in the total and in the backward part of the single stack. Only stacks with energy above Low Threshold (LT) are considered. These stacks are the basic BEMC trigger elements on which the cluster search algorithm works.

**BCTRIG** : BEMC trigger response is analysed and hardware like BSET bank (B32 format) is created.

**BTCLUS** : cluster analysis on the BEMC stacks is done

**BTIDEN** : cluster identification is done

**BTCLAD** : cluster counting is done. A chain of 2 adjacent hits (stacks above LT or HT) is considered as 1 cluster, 3 or 4 adjacent hits in the row or in the column are

considered as 2 clusters and if more than 4 hits are found, simply the number of hits is counted as a number of clusters. It has no sense to calculate exactly the number of clusters, because the  $[X, Y]$  projection method exactly determines only 1 cluster and can say that there were 2 or more clusters.

**BTTX (BTNS)** parameter text bank:  $\sigma$  of the noise in the stacks (total, backward) and in the trigger towers is defined

**BTTX (BSTH)** Following parameters in this text bank has to be defined:

- 3 (resp.2) thresholds for each stack
  - low threshold for the whole stack
  - high threshold for the whole stack
  - low threshold for 'hadronic' part of the stack
- 3 cluster thresholds
- 1 threshold for the total BEMC energy
- number of hit stacks in the innermost "ring" on both, high and low energy levels
- **RATIO** parameter defining acceptable leakage from the  $e^-$  showers into the 'hadronic' part

Stack thresholds can be all the same or one can redefine some or all low (total) and high thresholds. Excluding the stack from the trigger can be done by setting the corresponding threshold to the unrealistically high value.

The number of hit stacks in the innermost ring, mainly on the high energy level, can help to suppress background events rate.

For simulation studies one can use also the **RATIO** parameter, which is fraction of the energy seen by the so called "hadronic" WLS from the total cluster energy. In the hardware is this feature not realized yet. The main problem comes from fluctuations of the leakage into the backward part, even from electrons, and from the relatively large noise in this part of the calorimeter.

## A.2 The H1FAST

This fast, but still accurate shower parametrization is included into the GEANT framework and can be used alternatively to the detailed shower simulation.

The sampling structures of the H1 calorimeters are replaced by homogeneous volumes filled with averaged media. Energy depositions simulated in these media are mapped onto the actual read out geometry. The signal ( $e/mip$ ,  $e/h$  effects) and the desired resolution are generated in a second step by applying external response functions.

In the electromagnetic shower parametrization [74] the longitudinal and lateral shower shapes as well as their fluctuations and correlations are simulated.

In the hadronic showers only electromagnetic subshowers in the cascade are being parametrized. Parametrization over cracks is not allowed because it cannot be easily parametrized and this leads to an incorrect description of the energy losses in the dead material [73].

The fast MC is implemented in the general framework of GEANT for geometry description and particle tracking, while GHEISHA or FLUKA produce hadronic interactions.

All energy depositions (e.m., hadronic, energy lost in a nuclear reactions) in all parts of the detector are stored in BOS banks. This allows to reconstruct the response after simulation with simple response functions, which are basically sums over the smeared true energy depositions [75],[76]. This scheme provides the possibility of quick retuning with different response functions, and in addition the absolute energy scale of the MC is intrinsically correct.

### A.3 The H1PSI (Parametrised Simulation)

#### A.3.1 BEMC Geometry in H1PSI

The whole geometry description of the H1 detector is simplified in the H1PSI program. Many details are left out and material properties are averaged. Main differences in the BEMC description between H1PSI and H1SIM are the following:

- projective geometry in H1PSI with 5  $\Theta$  and 16  $\phi$  bins
- different granularity, in addition H1PSI BEMC stacks' size is radius dependent, most striking is the difference in the innermost ring where 4 H1PSI stacks correspond to 1 H1SIM stack
- different number of basic trigger elements (H1PSI 80 and H1SIM 88 stacks)
- angular acceptance - H1PSI ( $154^\circ - 176^\circ$ ), H1SIM ( $150.6^\circ - 175.6^\circ$ )
- in H1PSI is the 'hadronic part' of the stacks missing

#### A.3.2 BSET Trigger Code in H1PSI

Calling sequence:

```

BTGINI
CATRES
    BTRING
BSTRIG
    BTCLUS
        BTIDEN
            BTCLAD

```

**BTGINI** : In this module all thresholds and noise values from the text bank BTTX (BSTH resp. BTNS) are read in.

**CATRES** : The calibrated energy from the CACE digi bank is read out and BEMC channels are renumbered to 1 - 80. Numbering is spiraling from outermost ring and stops in the innermost ring. Depositions in the innermost ring are reorded due to the already mentioned difference in the granularity. Energies in the four adjacent stacks are summed up and put into the stack with maximal original deposit. If the corresponding steering parameter is chosen, noise is added to each stack.

Trigger banks UATB, UBTT and UBTB (LAr trigger part trigger towers, resp. big towers) and UBTS trigger banks are created. UBTS contains BEMC stack numbers and energy depositions in the whole stack. The so called hadronic part does not exist in H1PSI. In a similar way as in H1SIM only stacks with energy above LT are considered. These stacks, as in H1SIM, are the basic BEMC trigger elements on which the cluster search algorithm works.

**BSTRIG** : the BEMC trigger response is analysed and BSET trigger bits are stored in the TRBEMC common.

**BTCLUS** : the cluster analysis on the BEMC stacks is done, but now unlike in H1SIM the  $[R, \phi]$  projections are used for cluster search

**BTIDEN** : cluster identification

**BTCLAD** : cluster counting is done. For the cluster definition and number of found clusters the same considerations as in H1SIM are valid.

**BTTX (BTNS)** is the parameter text bank:  $\sigma$  of the noise in the stacks (total, backward) and in the trigger towers is defined

**BTTX (BSTH)** parameter text bank for which the following thresholds has to be defined:

- 2 thresholds for each stack
  - low threshold
  - high threshold
- 3 cluster thresholds
- 1 threshold for the total BEMC energy

The same way as in H1SIM different thresholds for each stack can be defined. The  $(R, \phi)$  symmetry is also used and the stack thresholds for the whole rings can be changed in one step.

## Appendix B

# The BEMC parameters

### B.1 Material Constants

The basic material constants important for the development of electromagnetic and hadronic showers are summarized in Table 4.1. Mean values for the whole BEMC (last row) of the nuclear interaction length  $\lambda_0$ , radiation length  $X_0$ , critical energy  $E_k$  and Molière radius  $R_M$  are calculated according the approximate analytical formulae of U. Amaldi [72]:

$$\lambda_0 \simeq 35A^{1/3} [gcm^{-2}] \quad (\text{B.1})$$

$$X_0 \simeq 180 \frac{A^2}{Z} [gcm^{-2}] \quad \left( \frac{\Delta X_0}{X_0} < \pm 20\% \quad \text{for} \quad 13 \leq Z \leq 92 \right) \quad (\text{B.2})$$

$$E_k \simeq \frac{550}{Z} [MeV] \quad \left( \frac{\Delta E_k}{E_k} < \pm 10\% \quad \text{for} \quad 13 \leq Z \leq 92 \right) \quad (\text{B.3})$$

$$R_M \simeq 7 \frac{A}{Z} [gcm^{-2}] \quad \left( \frac{\Delta R_M}{R_M} < \pm 10\% \quad \text{for} \quad 13 \leq Z \leq 92 \right) \quad (\text{B.4})$$

Table 4.1 Material constants

Material	Z	A	$\rho$ [ $gcm^{-3}$ ]	$\lambda_0$ [cm]	$X_0$ [cm]	$E_k$ [MeV]	$R_M$ [cm]
Al	13	26.98	2.70	39.4	8.9	39.3	3.69
Pb	82	207.19	11.35	17.09	0.56	7.2	1.56
Polystyrol	6	12	1.03	79.50	42.40	87.0	14.0
38.5% Pb,61.5% scin.	72.4?	182.6?	4.98	39.8	1.44	8.9	3.55

Table 4.2 BEMC module construction in  $X_0, \lambda_0$ , units

#oflayers	Material	Total Thickness in $X_0$	Total Thickness in $\lambda_0$
1	18 mm Al	0.20	0.05
49	2.5 mm Pb	21.88	0.72
50	4 mm SCSN 38	0.47	0.25
		$\Sigma = 22.55$	$\Sigma = 1.02$

## B.2 The BEMC Geometry (Granularity)

Most of the BEMC stacks are of the size  $15.9 \times 15.9 \text{ cm}^2$ . This size includes the complete steel box housing. The active size of the sampling structure is approximately  $15 \times 15 \text{ cm}^2$ . All other exotic types of stacks are not much smaller. This means that granularity is too big if compared to the Molière radius  $3.55 \text{ cm}$  characterizing the lateral size of the electromagnetic shower in this medium.

Nonprojective geometry and gaps (cracks) between the stacks are the sources of energy losses in the BEMC fiducial volume and make the task of the electron measurement and triggering more complicated.

Longitudinally the BEMC stacks are readout from two samples:

- from the whole length of the stack -  $E_{tot}$
- from the last third of the stack -  $E_{had}$

### B.2.1 Transversal Size of EM Showers

The lateral size of e.m. shower scales with the Molière radius  $R_M$ , which describes the average lateral deflection of electrons with energy  $\epsilon_c$  after traversing  $1 X_0$  and is essentially caused by two effects:

1. due to multiple Coulomb scattering electrons move away from the shower axis
2. bremsstrahlung photons may deflect quite far from the axis, particularly if they are emitted by electrons that themselves travel under a relatively big angle

The first process dominates in the early stages of the cascade development, while the second process is dominant beyond the shower maximum, particularly in high-Z media [84].

$$R_M = X_0 \frac{E_s}{\epsilon_c} \approx \frac{(21.2 \text{ MeV})}{\epsilon_c} \quad (\text{B.5})$$

Near  $t_{max}$  almost all the shower is contained in a core of radius  $\sim 1 X_0$ , but deeper in the shower, the core is surrounded by an extensive halo of multiply scattered low energy electrons, such that 95% of the shower energy is contained in a cylinder of  $\sim 2 R_M$ . Transversal size or in the terms BEMC trigger elements, number of hit stacks and amount of energy deposited in them tell us what is the cluster size we should use in the trigger (see chapter 5.1.1).

### B.2.2 Energy Containment (Energy Leakage)

**Electrons** The calorimeter length  $L$  needed to contain a fixed fraction 98% of the incident particle energy can be computed from the approximate analytical relations [72]:

$$L(98\%) = 3t_{med} \quad (\text{B.6})$$

$$t_{med} = \left( \ln \frac{E}{E_k} + 0.4 \right) \quad (\text{B.7})$$

where  $t_{med}$  is the median depth of the shower, i.e. depth at which half of the initial energy is deposited. In our case it turns out that  $L(98\%) = 25.5 X_0$ . If the 10 – 20% error of this calculation is taken into account, this roughly corresponds to the total BEMC length. Test measurements confirmed that EM showers are well contained even for maximal 30 GeV electrons with negligible leakage behind the BEMC ( $\sim 600$  MeV) [56].

Leakage problems arise at angles above  $173^\circ$  (close to the beam pipe) where the electron hits the BEMC near to the edge and part of the energy is lost due to the transversal size of the shower. Due to the triangular form of the innermost BEMC stacks the energy losses are also dependent on the azimuthal angle  $\phi$ .

The second "leaky" area arises at angles smaller than  $156^\circ$  (Fig 2.3). In this case BEMC depth seen by the traversing particle is not sufficient for full containment and due to the not projective geometry the side leakage also plays its role of course. Overlap with the liquid argon calorimeter is not very good and big energy corrections have to be applied in this region.

Other areas where some portion of the energy is lost, even in the good angular region, are those in between the BEMC stacks, in the gaps between the basic building blocks.

Quantitative estimates of all these effects and energy sharing between adjacent stacks define the cluster energy thresholds which should be used for well controlled triggering on the defined electron energies.

**Hadrons** From the similar equations for *hadronic showers* [72]:

$$x_{med} = (0.54 \ln E + 0.4)\lambda_0 \quad (\text{B.8})$$

$$L(95\%) \simeq 2.5x_{med} \quad (\text{B.9})$$

we realize that the calorimeter length needed to absorb 95% energy of incident 5 and 10 GeV pions is 3.2 resp. 4.2  $\lambda_0$ .

From these BEMC parameters is clear that BEMC is really only electromagnetic calorimeter, with good containment of electromagnetic showers but too "short" ( $\lambda_0 = 1.02$ ) for hadronic particles.

$e^-/\pi$  separation achievable with the BEMC alone is insufficient and good  $e^-$  identification below 10 GeV is rather difficult. This is very severe for the L1 trigger level, where additional means of the off-line analysis are not available.

---

## Bibliography

- [1] ECFA 80/42, March 1980, DESY HERA 80/01,  
Study on the Proton-Electron Storage Ring Project HERA
- [2] H1 Collaboration, DESY June 28, 1985,  
Letter of Intent for an Experiment at HERA
- [3] H1 Collaboration, March 1986,  
Technical Proposal for the H1 Detector
- [4] H1 Collaboration, October 1987,  
Technical Progress Report
- [5] G. Ingelman, R. Rückl, in Proc. of the HERA Workshop,  
Hamburg 1987, Ed. R.D. Peccei, Vol.1, p.107
- [6] B. Campbell, V. Elias, W.R. Frisken, Can. J. Phys. 59 (1981) 1742  
E. Lohrmann, K.-H. Mess, DESY HERA 83/03 (1983)
- [7] M. Klein, PHE 90-25, Zeuthen Preprint, November 1990,  
Deep Inelastic Scattering at HERA
- [8] J. Blümlein et al., in Proc. of the HERA Workshop,  
Hamburg 1987, Ed. R.D. Peccei, Vol.1, p.67
- [9] Ed. U. Amaldi, DESY 79/48 (1979), p. 391-394,  
Proc. of the study of an ep facility for Europe
- [10] J. Feltesse, DAPNIA/SPP 92-01, January 1992, Revised version  
HERA the New Frontier, Lectures pres. at the SLAC Summer Institute,  
Stanford, California, 5-16 August 1991
- [11] G. Bernardi, W. Hildesheim, in Proc. of the Physics at HERA Workshop,  
Hamburg 1991, Eds. W.Buchmuller, G. Ingelman, Vol. 1, p.79
- [12] S. Bentvelsen et al., in Proc. of the Physics at HERA Workshop,  
Hamburg 1991, Eds. W.Buchmuller, G. Ingelman, Vol. 1, p.23
- [13] J.D. Björken, Phys.Rev **179**(1969) 1547  
J.D. Björken, E.A. Paschos, Phys.Rev **185**(1969) 1975
- [14] E.D. Bloom et al., Phys.Rev.Lett. **23**(1969) 930
- [15] R.P. Feynman, Phys.Rev.Lett. **23**(1969) 1415  
R.P. Feynman, W. A. Benjamin Inc., 1972,  
Photon-Hadron Interactions

- [16] G. Miller et al., Phys.Rev. **D5**(1972) 528  
A. Bodek et al., Phys.Rev.Lett. **30**(1973) 1087
- [17] C. Chang et al., Phys.Rev.Lett. **35**(1975) 901  
H.L. Anderson et al., Phys.Rev.Lett. **37**(1976) 1034  
S. Stein et al., Phys.Rev. **D12**(1975) 1884
- [18] A.D.Martin et al., Nucl.Phys.B (Proc.Suppl.) **29A**(1992) 14
- [19] P. Amaudruz et al., Phys.Rev.Lett. **66**(1991) 2712
- [20] H. Plathow-Besch, CERN-PPE,1992.07.22, W5051 PDFLIB,  
PDFLIB: Structure Functions and  $\alpha_s$  Calculations, (User's Manual)
- [21] L.V. Gribov, L.N. Lipatov, Sov.Journ.Nucl.Phys. **15**(1972) 438 and 675  
G. Altarelli, G. Parisi, Nucl.Phys. **126**(1977) 297  
Yu. L. Dokshitzer, Sov.Phys.JETP **46**(1977) 641 G. Marchesini, B. Webber,  
Nucl.Phys. **B349**(1991) 617
- [22] E.A. Kuraev, L.N. Lipatov, V.S. Fadin, Sov.Phys.JETP **45** (1977) 199  
Ya. Ya. Balitzky, L. N. Lipatov, Sov.Jour.Nucl.Phys. **28**(1978) 822
- [23] B. Webber, Proc. of the Physics at HERA Workshop,  
Hamburg 1991, Eds. W.Buchmuller, G. Ingelman, Vol. 1, p.285  
G. Marchesini, B. Webber, Nucl.Phys. **B349**(1991) 617
- [24] L.V. Gribov, E.M. Levin and M.G. Ryskin, Nucl.Phys. **B188**(1981) 555; Phys. Rep.  
**100**(1983)
- [25] A. Donnachie, P.V. Landshoff, Phys.Lett. **185B**(1987) 403
- [26] A.H. Mueller and J. Qiu, Nucl.Phys. **B268**(1986) 427
- [27] J. Bartels, J. Feltesse, Proc. of the Physics at HERA Workshop,  
Hamburg 1991, Eds. W.Buchmuller, G. Ingelman, Vol. 1, p.131
- [28] A.H. Mueller, Nucl.Phys.B (Proc.Suppl.) **18C**(1991) 125  
A.H. Mueller, Navelet, Nucl.Phys. **B282**(1987) 727  
J. Bartels et al., Proc. of the Physics at HERA Workshop,  
Hamburg 1991, Eds. W.Buchmuller, G. Ingelman, Vol. 1, p.203
- [29] M.G. Ryskin, M. Besancon, Proc. of the Physics at HERA Workshop,  
Hamburg 1991, Eds. W.Buchmuller, G. Ingelman, Vol. 1, p.215
- [30] K. Charchula, E.M. Levin, Proc. of the Physics at HERA Workshop,  
Hamburg 1991, Eds. W.Buchmuller, G. Ingelman, Vol. 1, p.223
- [31] G. Ingelman, K. Janson-Prytz, Proc. of the Physics at HERA Workshop,  
Hamburg 1991, Eds. W.Buchmuller, G. Ingelman, Vol. 1, p.233

- [32] G. A. Schuler, in Proc. of the Physics at HERA Workshop, Hamburg 1991, Eds. W.Buchmuller, G. Ingelman, Vol. 1, p.461  
A. Levy, *ibid.* p.481  
S. Levonian, *ibid.* 499  
G.Schuler, J. Terron, CERN-TH 6415/92 (1992)
- [33] B. Schrepf, in Proc. of the Physics at HERA Workshop, Hamburg 1991, Eds. W.Buchmuller, G. Ingelman, Vol. 2, p.1034
- [34] H1 Collaboration (T. Ahmed, ...T.Kurča...,et al.), DESY-92-160, Nov 1992  
Phys.Lett. **B299**(1993) 374-384  
Total photoproduction cross-section measurement at HERA energies
- [35] H1 Collaboration (T. Ahmed, ...T.Kurča...,et al.), DESY-92-164, Nov 1992,  
Phys.Lett. **B299**(1993) 385-393,  
Observation of deep inelastic scattering at low x
- [36] H1 Collaboration (I. Abt, ...T.Kurča...,et al.), DESY-93-117, Aug 1993,  
Nucl.Phys. **B407**(1993) 515-535,  
Measurement of the proton structure function  $F_2(x, Q^2)$  in the low x region at HERA
- [37] H1 Collaboration (T. Ahmed, ...T.Kurča...,et al.), DESY-92-162, Nov 1992  
Phys.Lett.**B298**(1993) 469-478,  
Measurement of the hadronic final state in deep inelastic scattering at HERA
- [38] H1 Collaboration (T. Ahmed, ...T.Kurča...,et al.), DESY-93-029, March 1993,  
Nucl.Phys. **B396**(1993)3-23,  
A Search for Leptoquarks, Leptogluons and Excited Leptons in H1 at HERA
- [39] Ch. Berger et al., in Proc. of the Physics at HERA Workshop, Hamburg 1991, Eds. W.Buchmuller, G. Ingelman, Vol. 2, p.1029
- [40] B. Andrieu et al., DESY-93-078, June 1993,  
to be published in Nucl.Instr.& Methods,  
The H1 Liquid Argon Calorimeter System
- [41] F.W. Brasse, DESY 92-140, Hamburg October 1992,  
The H1 Detector at HERA
- [42] D. Breton et al., H1 Int. Report H1-04/92-219,  
H1 calorimeter calibration electronics
- [43] E. Elsen, in Procc. of the International Symposium Electronic Instrumentation in Physics, Dubna, May 14-17, 1991,  
H1 note, H1-01/93-262, Hamburg Januar 1993,  
The H1 Trigger and Data Acquisition System
- [44] P. Loch, PhD Thesis, FH1K-92-02, DESY intern., October 1992,  
Kalibration des H1 Flüssig-Argon Kalorimeters unter Berücksichtigung der Gewichtungsmethode für Teilchenjets

- J. Gayler, H1 note, H1-10/92-250, DESY, Hamburg, October 1992,  
Contr. to the 3rd Intern. Conf. on Calorimetry in High Energy Physics, Sept. 29 -  
Oct. 2, 1992, Corpus Christi, Texas  
Performance of the H1 Liquid Argon Calorimeter
- [45] J. Tutas, H1 note, H1-10/92-246, DESY, Hamburg 1992,  
The limited streamer tube system of H1
- [46] J. Tutas, H1 note, H1-07/91-185, DESY, Hamburg, July 1991,  
A Level 1 Trigger from the Limited Streamer Tube system
- [47] BEMC Group, H1 note, H1-07/92-233, DESY, Hamburg 1992,  
The H1 Backward Electromagnetic Calorimeter
- [48] J. Coughlan et al., H1-04/90-135, DESY, Hamburg April 1990,  
Proposal to build muon triggers and time-of-flight hodoscope for the H1 experiment  
at HERA
- [49] D. P. Johnson, H1 note, H1-07/87-65, April 1987,  
Beam-Gas Background at HERA
- [50] G. Grindhammer et al., H1-TR-300, September 1987,  
The First Level Liquid Argon Calorimeter Trigger Physics Requirement
- [51] R.J. Ellison, U. Straumann, H1 note, H1-05/90-137, May 1990
- [52] H. Brettel et al., H1-MPI-140, Munich, October 1990,  
Calorimeter Event  $t_0$  and trigger elements for CTL and DSP
- [53] J. Bán, T. Kurča, M. Seman, IEP Košice, September 1990,  
Proposal for separated electron and independent  $t_0$  trigger for BEMC
- [54] H. Krehbiel, DESY, July 1991,  
The extended fan out card of the H1 STC
- [55] H.T. Duhme et al., H1 note, September 1991,  
VME board GPTP - General Purpose Trigger Pipe (User Manual)
- [56] BEMC Group, H1 note, H1-08/92-234,  
Calibration and Reconstruction of the BEMC
- [57] F. Descamps, C. Vallee, H1 note H1-10/92-256,  
Data Acquisition for the H1 Calorimeters
- [58] S. Levonian, H1 software note 03/91-20,  
EVLOOK - An Interactive Program for the H1 Event Display
- [59] S. Egli, H1 software note 10/90-12,  
BOS modules in H1 software - A set of rules and recommendations

- [60] R. Eichler et al., H1 note, H1-4/87-61, H1-TR 302, DESY, April 1987,  
The First Level MWPC Trigger for the H1-Detector  
S. Eichenberger et al., H1-note, H1-02/92-214, DESY, Februar 1992,  
A Fast Pipelined Trigger for the H1 Experiment based on Multiwire Proportional  
Chamber Signals
- [61] Th. Wolff et al., H1-note, H1-02/92-213, DESY, Februar 1992,  
A Driftchamber Track Finder for the First Level Trigger of the H1-Experiment
- [62] S. Levonian, in Proc. of the Physics at HERA Workshop,  
Hamburg 1991, Eds. W.Buchmuller, G. Ingelman, Vol. 1, p.499,  
Total Photoproduction Cross Section Measurement at HERA
- [63] J. Heatherington et al., H1 note, H1-08/93-307, DESY, Hamburg 1993,  
Studies on TOF FTDC data
- [64] H. Hufnagel et al., unpublished, H1 internal software information,  
L5-Event Classification
- [65] G.A. Schuler, H. Spiesberger, Proceedings, Physics at HERA,  
Hamburg 1991, Eds. W.Buchmuller, G. Ingelman, Vol. 3, p.1419,  
DJANGO: the interface for the event generators HERACLES and LEPTO
- [66] A. Kwiatkowski et al., Comp.Phys.Comm. 69 (1992) 155
- [67] G. Ingelmann, "LEPTO 5.2", unpublished program manual;  
H. Bengtsson et al. Nucl.Phys. **B301**(1988) 554
- [68] A. D. Martin et al., Phys.Rev. **D47**(1993) 867
- [69] G.A. Schuler, T. Sjöstrand, Phys.Lett. **B300**(1993) 169
- [70] T. Sjöstrand in Proc. of the Physics at HERA Workshop,  
Hamburg 1991, Eds. W.Buchmuller, G. Ingelman, Vol. 3, p.1405  
PYTHIA at HERA
- [71] H1 interface program to LUCVDM of the LUCIFER package of  
G. Ingelman and A. Weigend, Computer Phys. Comm. **46**(1987)241
- [72] U. Amaldi, Phys.Scripta **V23**(1981) 409-424,  
Fluctuations in Calorimetry Measurements
- [73] M. Kuhlen, H1 internal note H1-10/92-254,  
presented at XXVI Int. Conf. on High Energy Physics, Dallas 1992,  
The Fast H1 Detector Monte Carlo
- [74] S. Peters, PhD Thesis, Universität Hamburg, 1992  
Die parametrische Simulation elektromagnetischer Schauer.
- [75] M. Rudowicz, PhD Thesis, Universität Hamburg, 1992  
Hadronische Schauersimulation für H1-Detector.

- [76] G. Bernardi et al., H1 Software Note 26, (1991),  
Calibrated Energies in H1 Detector Simulation
- [77] P. Reimer, H1/BEMC group internal note No. 10-90,  
MC study of BEMC energy resolution and software calibration constant dependence  
on impact point position, electron energy and ep vertex smearing
- [78] BEMC group, H1 internal note H1-08/92-233,  
The H1 Backward Electromagnetic Calorimeter (BEMC)
- [79] D. Handschuh, PhD Thesis, Universität Hamburg, 1993  
Studien zum Protoninduzierten Untergrund am H1 Detektor und Entwicklung von  
Filteralgorithmen zu dessen Unterdrückung
- [80] R. Brun et al., DD/EE/84-1, CERN, September 1987,  
GEANT 3
- [81] V. Blobel, DESY R1-88-01 Internal Report, Januar 1988,  
The BOS System Dynamic Memory Management,  
Second updated printing Fortran77 Version
- [82] L. Criegee, privat communication
- [83] H1 Collaboration, PRC 92/03, H1 09/92-243, DESY, September 1992,  
Letter of Intent to Upgrade the Backward Region of the H1 Detector  
H1 Collaboration, PRC 92/01, H1 06/92-226, DESY, June 1992,  
Technical Proposal to build Silicon Tracking Detectors for H1
- [84] R. Wigmans, in Techniques and Concepts of High-Energy Physics VI,  
ed. Th. Ferbel, Series B: Physics Vol. 275, p. 325, 1990, St. Croix,  
Calorimetry in High Energy Physics

## Acknowledgments

First of all I would like to thank the H1 Collaboration and its spokesmen Prof.Dr. F. Eisele and Prof.Dr. J. Feltse for their encouragement and the possibility to work with H1 at DESY.

I would like also to express my gratitude to DESY and the DFG for their financial support, which enabled my stay at Hamburg.

I greatly appreciate the support from the Directorate and from the High Energy Physics Department of my home Institute of Experimental Physics in Košice.

I would like to thank all my colleagues in Košice whose contribution enabled me to join the H1 experiment, especially Dr. M. Seman for his suggestion and first ideas on the single electron trigger for the BEMC, the engineers J. Bán, J. Špalek, F. Kriváň who practically realized the BSET trigger ideas and Dr. J. Ferencei for his enthusiastic effort and coordination of the work connected with running of the BEMC and the BSET.

I would like to thank Prof.Dr. K. Meier for his support and his coordination of the BEMC group.

I am very grateful to Dr. A. DeRoeck for his support and many illuminating discussions about the triggering of NC DIS. It was a great pleasure to work in the H1 trigger group and in the electron physics analysis group ELAN. Discussions with Dr. M. Klein, Dr. Th. Naumann and E. Peppel were very helpful for me. I would like to thank Dr. G. Cozzika, Dr. A. DeRoeck and Dr. E. Elsen for careful reading of the manuscript and for many useful suggestions and comments.

I would like to thank all members of the BEMC group from the I. Institute of Physics at University Hamburg, lead by Prof.Dr. H.-H. Duhm, for their friendship, kind hospitality and help not only at physics related problems. Special thanks to H.-P. Kassermann for his friendly help during the completion of this thesis and for stimulating discussions.

I am very grateful to Prof.Dr. H.-H. Duhm for motivating discussions, for his kind support and his readiness to take over the supervisor's duties. Many thanks also to Prof.Dr. W. Bartel for his interest and willingness to write the referees report.

Last but not least I would like to thank my wife Viera for her patience and understanding of my almost permanent absence from home.